Carbon Nanotube Based Dosimetry of Neutron and Gamma Radiation

Anthony J. Nelson

Dissertation submitted to the faculty of the Virginia Polytechnic Institute and State University in partial fulfillment of the requirements for the degree of

Doctor of Philosophy

In

Engineering Mechanics

Committee:

Mark A. Pierson, Chair

Marwan S. Al-Haik, Co-chair

Scott W. Case, Co-chair

Ilia N. Ivanov

Muhammad R. Hajj

Mayuresh J. Patil

March 10, 2016

Blacksburg, VA

Keywords: carbon nanotubes, neutron radiation, radiation dosimetry, reactor pressure vessel lifetime assessment, gamma rays

Carbon Nanotube Based Dosimetry of Neutron and Gamma Radiation

Anthony J. Nelson

Abstract

As the world's nuclear reactors approach the end of their originally planned lifetimes and seek license extensions, which would allow them to operate for another 20 years, accurate information regarding neutron radiation exposure is more important than ever. Structural components such as the reactor pressure vessel (RPV) become embrittled by neutron irradiation, reducing their capability to resist crack growth and increasing the risk of catastrophic failure. The current dosimetry approaches used in these high flux environments do not provide real-time information. Instead, radiation dose is calculated using computer simulations, which are checked against dose readings that are only available during refueling once every 1.5-2 years. These dose readings are also very expensive, requiring highly trained technicians to handle radioactive material and operate specialized characterization equipment. This dissertation describes the development of a novel neutron radiation dosimeter based on carbon nanotubes (CNTs) that not only provides accurate real-time dosimetry, but also does so at very low cost, without the need for complex instrumentation, highly trained operators, or handling of radioactive material. Furthermore, since this device is based on radiation damage rather than radioactivation, its readings are time-independent, which is beneficial for nuclear forensics. In addition to development of a novel dosimeter, this work also provides insight into the particularly under-investigated topic of the effects of neutron irradiation of carbon nanotubes.

This work details the fabrication and characterization of carbon nanotube based neutron and gamma radiation dosimeters. They consist of a random network of CNTs, sealed under a layer of silicon dioxide, spanning the gap between two electrodes to form a conductive path. They were fabricated using

conventional wafer processing techniques, making them intrinsically scalable and ready for mass production. Electrical properties were measured before and after irradiation at several doses, demonstrating a consistent repeatable trend that can be effectively used to measure dose. Changes to the microstructure were investigated using Raman spectroscopy, which confirmed that the changes to electrical properties are due to increasing defect concentration.

The results outlined in this dissertation will have significant impacts on both the commercial nuclear industry and on the nanomaterials scientific community. The dosimeter design has been refined to the point where it is nearly ready to be deployed commercially. This device will significantly improve accuracy of RPV lifetime assessment while at the same time reducing costs. The insights into the behavior of CNTs in neutron and gamma radiation environments are of great interest to scientists and engineers studying these nanomaterials.

Acknowledgements

I would like to thank my advisors, Dr. Marwan Al-Haik and Dr. Mark Pierson, for their guidance and support. I am very fortunate and grateful to have had the opportunity to work under their supervision. I would also like to thank my committee, especially Dr. Ilia Ivanov, who served as my technical contact at Oak Ridge National Lab and provided invaluable assistance and advice, and Dr. Scott Case, who served as co-chair of my committee.

I am very grateful to all of my research group members, including Ayoub Boroujeni, Dr. Mehran Tehrani, Dr. Amir Skandani, Anahita Emami, Dr. Nejib Masghouni, Dr. Masoud Safdari, and Dr. Radim Ctvrtlik. I would also like to thank my other colleagues at Virginia Tech including Zhipeng Tian, Sadia Afroz, Don Leber, Dr. Chris Winkler, Steve McCartney, Dr. Masoud Agah, Jonathan Metzman, Dr. Vaishnavi Srinivasaraghavan, Dr. Muhammad Akbar, Dr. Randy Heflin, and Dr. Carlos Suchicital. I would like to thank the wonderful administrative staff of my department, in particular Lisa Smith, Melissa Nipper, and Mark Warbec.

I would like to thank my collaborators at Oak Ridge National Lab, including Eric Muckley, Dr. Chris Jacobs, David Glasgow, Riley Hunley, and Geoffrey Deichert.

I would like to thank the organizations that provided funding or other assistance, including Virginia Tech, the Department of Biomedical Engineering and Mechanics, the Nuclear Regulatory Commission, Oak Ridge National Lab, and the Center for Nanophase Materials Science.

Finally, I would like to thank my family and friends, particularly my mother, Patti Tyree, for her support and my girlfriend, Jenna Whisler, for her patience.

Table of Contents

List of Figures

List of Tables

1. Introduction

1.1 Objectives

The objectives of this dissertation are to develop a carbon nanotube based real-time neutron dosimeter for reactor pressure vessel (RPV) lifetime assessment and to gain insights into the effects of high flux neutron and gamma irradiation on single wall carbon nanotubes (SWNTs) and multiwall carbon nanotubes (MWNTs). This dissertation lays out the theory and design of a novel neutron radiation dosimeter that represents an improvement to existing technology. The process by which this design was developed, including the results of four generations of device configurations, is described in detail. This dosimeter will improve the ability of the nuclear industry to evaluate the extent of neutron radiation exposure to critical reactor components, improving safety and allowing for more accurate lifetime predictions.

In addition to the development of a novel neutron dosimeter, this work makes significant contributions to the field of nanotechnology. The effects of high flux neutron and gamma irradiation on carbon nanotubes (CNTs) is a particularly under-investigated topic and this dissertation will contribute to establishing an understanding of how high flux neutron and gamma irradiation impacts these unique nanomaterials on a structural level and, consequently, how these changes to microstructure impact the macroscopic properties. A thorough review of the published literature shows that there has never been an experimental investigation into the effects of neutron bombardment on the electrical properties of 2D carbon nanotube networks.

This dissertation is organized as follows: Chapter 1 discusses the background and theory behind the operation of the devices and summarizes the current state of the art. Chapter 2 describes the

experimental procedure used to fabricate, irradiate, and characterize the devices. Chapter 3 summarizes the evolution of the design of the devices, laying out the design, fabrication techniques, and results of the first three generations of devices that led to the final design. Chapter 4 is dedicated to the results of the final device. Chapter 5 summarizes the conclusions that can be drawn from these results and discusses avenues for future research that build upon the results of this project.

1.2 Motivation

The United States currently has 99 operating commercial nuclear power plants with an average age of over 30 years. Originally granted licenses to operate for 40 years, most of these facilities have applied for 20-year extensions. In addition, research is already being conducted into extending nuclear power plant lifetime to 80 years. With an aging fleet of nuclear reactors, accurate lifetime assessment is more important than ever, and radiation dosimetry plays a critical role.

The steel pressure vessel that contains the reactor core, core shroud, and reactor coolant is one of the most critical components for lifetime assessment. Because they cannot practically be replaced, most reactor pressure vessels (RPVs) are over 30 years old and are expected to last for at least another twenty years. The stainless steel out of which these pressure vessels are made is embrittled by neutron irradiation, reducing its capability to resist crack growth and increasing the probability of catastrophic failure.

To avoid such failure it is important to closely monitor the neutron dose of the RPV. The approach currently used in commercial reactors utilizes a combination of computer simulations and dosimetric readings. One of the primary methods currently used for evaluating the exposure dose of the pressure vessel is to scrape off some material from the inner surface of the RPV and measure the ^{54}Mn activity of

the sample. Since the extent of activation is proportional to neutron dose, it is possible to determine the amount of radiation that the pressure vessel was exposed to. This method has several serious drawbacks, most notably that it only gives reliable information for the previous 3 years of reactor operation and that it can only be carried out during the times when the reactor is not operating [1]. Another technique involves placing a niobium capsule in the pressure vessel, then removing it and recording the extent to which it has been activated [2]. This method also suffers from the fact that it is impossible to gain real-time information on the exposure dose of the RPV. Furthermore, calibrated Nb detectors are no longer available from NIST [3]. Another approach to estimate the radiation dose is to place a niobium, nickel, iron, titanium, or copper foil between the outer wall of the pressure vessel and biological shielding [4, 5]. This method is relatively easier than removing samples from inside the pressure vessel, but the fluence is decreased by shielding from the pressure vessel and it also does not provide real time dosimetry. Another method involves fabricating test specimens from the same batch of steel as the pressure vessel and placing them on the outside of the core basket. These specimens are removed at ten year intervals to measure changes to their mechanical properties.

The dosimeters developed in the course of this project have some advantages over the techniques currently being used. These carbon nanotube based dosimeters could offer real time results so simulations can be verified and modified throughout a cycle instead of waiting until refueling to find out if there are any errors, which will significantly improve accuracy of dose information. Also, these tiny devices are cheap to fabricate and, unlike activation-based dosimetry methods, they do not require highly trained technicians to evaluate. This means that they can be installed at a number of locations in the pressure vessel in order to map the radiation dose with higher resolution, increasing the likelihood that any unexpected local variations are spotted. Furthermore, since the readings are based on damage to the microstructure of the CNTs, such as formation of vacancies in the lattice, which are the same

types of interactions that cause embrittlement to the RPV, the dose information is sensitive to radiation of the type that is most concerning for structural components. This is in contrast to activation based dosimetry, which uses a fundamentally different type of interaction to measure radiation dose.

Another important application for these carbon nanotube based dosimeters is nuclear forensics. Activation based dosimetry methods suffer from the drawback of being time dependent. Over time, the activity of the sample will decay, and eventually the dose information will be lost. If, for instance, in the case of a nuclear accident investigators cannot gain access to the dosimeter for several months, activation based dosimeters will have significantly decayed and the accuracy of the dose readings will be compromised. Since the carbon nanotube dosimeters rely on irreversible structural changes to the molecules, the dose record remains intact indefinitely, allowing accurate dosimetry even after significant delays.

1.3 Neutron and Gamma Radiation

Neutron and gamma radiation are the two types of ionizing radiation that carry no charge. Neutron radiation consists of lone neutrons while gamma rays are made up of high energy photons. Energetic neutrons can be generated by nuclear fission and fusion, radioactive decay, and particle interactions such as nuclear spallation [6]. Gamma rays and other high energy photons are produced by a large number of processes including nuclear fission and fusion, radioactive decay, neutron capture, bremsstrahlung, synchrotron radiation, annihilation radiation, and characteristic X-rays emitted by relaxation of an excited atom [6]. Neutron and gamma radiation are concerns for both human safety and protection of equipment in medical, military, energy, and aerospace applications.

Since gamma and neutron radiation carry no charge, they can only interact with matter through collisions with particles. Gamma rays can interact with either the nucleus or with the electrons in an atom, while neutrons only interact with nuclei. The most common means by which photons lose energy are through photoelectric absorption, Compton scattering, and pair production. Photoelectric absorption occurs when a photon is absorbed by the atom, which then ejects an energetic photoelectron. This process leaves a vacancy in one of the bound shells of the atom, which can result in the emission of a characteristic X-ray or an Auger electron [6]. Compton scattering results when a photon collides with an electron, changing direction and transferring some of its energy to the recoil electron. Pair production is only possible with gamma rays having energy greater than 1.02 MeV in the vicinity of an atomic nucleus and is characterized by the transformation of the photon into an electron-positron pair. When the positron annihilates, two additional annihilation photons are produced [6].

In contrast to gamma rays, which generally result in emission of photons, electrons, or positrons, the secondary radiations created by neutrons usually comprise heavy charged particles. Neutrons can interact with matter through elastic scattering, inelastic scattering, and absorption. In elastic scattering, the neutron collides with a nucleus, transferring some of its energy, and the total kinetic energy of the two bodies is conserved. When inelastic scattering occurs, the resulting kinetic energy of the two bodies is less than the original kinetic energy of the incoming neutron, some of the energy having been used to place the nucleus into an excited state, from which it will later emit radiation. Absorption results when a nucleus absorbs an incident neutron causing fission or the emission of a recoil nucleus, a proton, neutrons, gamma rays, or an alpha particle [7].

Neutron collisions with nuclei can result in displacement of the atom from its position in the lattice, whereas gamma ray collisions will primarily ionize an atom but not displace it. Gamma rays can also break molecular bonds such as in radiolysis of water molecules.

1.4 Carbon Nanotubes

1.4.1 Carbon Nanotube Structure

Since their discovery in 1991 [8], carbon nanotubes (CNTs) have been the subject of numerous studies due to their remarkable electrical, thermal, and physical properties. Carbon nanotubes are a cylindrical allotrope of carbon with side walls one atom thick, diameters as small as 0.5 nm, and aspect ratios as high as 132,000,000:1 [9]. They can be divided into two broad classifications: single wall nanotubes (SWNTs) consist, as their name suggests, of a single carbon cylinder, while multi-wall nanotubes (MWNTs) are composed of concentrically stacked SWNTs as shown in Figure 1.

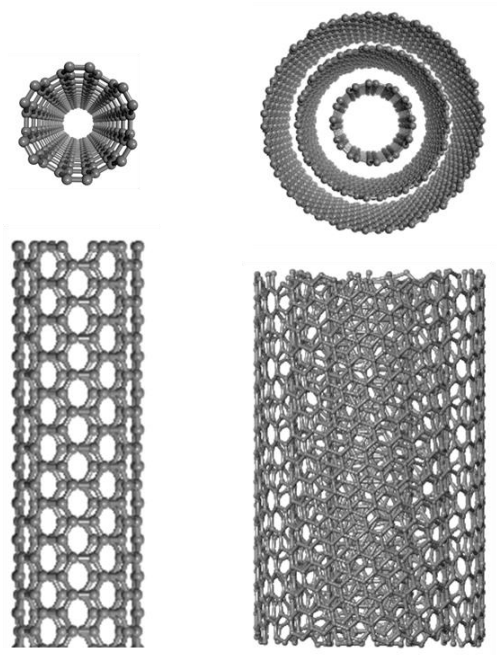

Figure 1: SWNT (left) and MWNT (right)

Though the method of fabrication is quite different, CNTs can be thought of as cut from a sheet of graphene and rolled into a cylinder. The angle of this rolling is referred to as the chiral angle, and it determines the pattern of the nanotube side walls, as shown in Figure 2.

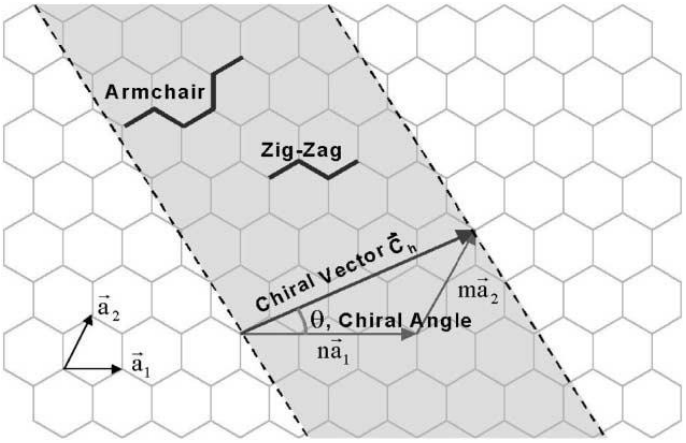

Figure 2: Chiral angles and chiral vector [10]. (Image used under Fair Use)

The chirality of carbon nanotubes can also be described by the chiral vector, $\vec{\boldsymbol{C}}_h$, given by

$$\vec{\boldsymbol{C}}_h = n\vec{\boldsymbol{a}}_1 + m\vec{\boldsymbol{a}}_2 \qquad 1$$

where (n, m) are the chiral indices, which represent the number of steps along the carbon bonds of the hexagonal lattice in their respective directions.

There are three general categories of chirality: armchair, zigzag, and chiral, as shown in Figure 3. A chiral angle of 0°, $(n, 0)$, corresponds to the zigzag pattern, a 30° chiral angle, (n, n), gives an armchair pattern, and patterns formed by other chiral angles are broadly referred to as chiral [10].

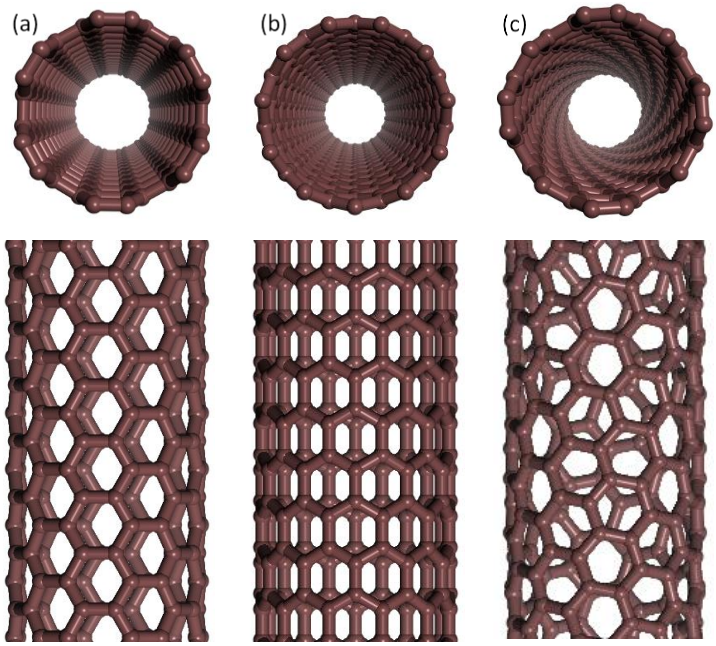

Figure 3: Carbon nanotube chirality: (a) armchair, (b) zigzag, and (c) chiral.

1.4.2 Carbon Nanotube Properties

Carbon nanotubes have unique mechanical and electrical properties that vary depending on a number of factors including dimensions, defects, chirality, and whether they are SWNTs or MWNTs. There have been a number of attempts to characterize the properties of individual CNTs but, due to challenges associated with their small size and the difficulty in manufacturing nanotubes of identical configurations, there is some debate as to the actual values. Most studies have concluded that the elastic modulus of SWNTs is around 1.0 TPa, that the strength is between 13 and 150 GPa [10-21], and that the Poisson's ratio is 0.16 [22]. CNTs have also demonstrated excellent resistance to permanent damage from significant deformations and shape changes [17].

Unlike their mechanical properties, the electrical properties of carbon nanotubes are strongly affected by chirality. There are three general classes of SWNTs based on their electrical properties: metallic with

zero bandgap, semiconducting with a small bandgap, or semiconducting with a large bandgap. All armchair (n, n) SWNTs are metallic, while zigzag $(n, 0)$ and chiral (n, m) SWNTs are semiconductors with a very small bandgap if $n - m$ is a nonzero multiple of 3 [23]. All other SWNTs are semiconductors with a large bandgap. Furthermore, in semiconducting SWNTs, the gap size depends on the nanotube diameter. For large gap SWNTs, the gap is inversely proportional to the diameter while for small gap SWNTs it is inversely proportional to the square of the diameter. Since the bandgap decreases with increasing nanotube diameter and MWNTs tend to have an outer diameter an order of magnitude larger than SWNTs, the outer layer typically has a nearly zero gap even if it does not have armchair chirality. For this reason, MWNTs are generally considered to behave as highly conductive metals [17]. Table 1 shows the electrical properties of the four types of carbon nanotubes.

Table 1: Carbon nanotube electrical properties.

Carbon Nanotube Electrical Properties		
Structure	**Category**	**Bandgap Dependence**
Armchair SWNT n=m	Metallic (zero gap)	None
SWNT, n-m=3k	Small bandgap	$1/r^2$
SWNT, n-m≠3k	Large bandgap	1/r
MWNT	Metallic (zero gap)	None

The theoretical intrinsic two-terminal resistance of metallic SWNTs has been calculated to be 6.5 kΩ [17] and the actual resistance has been measured as low as 10 kΩ [24]. While metallic SWNTs have zero bandgap, that of semiconducting SWNTs can be anywhere from just above zero up to as high as silicon [25]. This extraordinary tunability is one of the reasons why carbon nanotubes show so much promise for sensing applications.

When mechanically deformed via bending, twisting, or stretching or arranged in networks or bundles, the electrical properties of carbon nanotubes become somewhat more complex. Experimental

measurements of metallic SWNTs with a kink caused by bending of the nanotube have shown that flattening of the tube results in a tunnel junction, which behaves in much the same way as two intersecting SWNTs [26]. Twisting of a metallic SWNT has also been predicted to change the electrical properties, inducing a band gap that is proportional to the twist angle [27]. Axial stretching has been shown to induce a bandgap in metallic SWNTs and to modify the bandgap in semiconducting SWNTs [28]. Due to their high aspect ratio, SWNTs tend to agglomerate in bundles or ropes containing tens to hundreds of individual nanotubes in a close-packed lattice, which can cause changes to their electrical behavior. One first-principles study predicts that a bundle of metallic armchair SWNTs will behave as a semiconductor due to interactions between tubes [29].

Defects and doping also have a significant effect on the electrical properties of carbon nanotubes. The effects of defects are dependent both on the type of defect and the type of nanotube. Semiconducting SWNTs containing defects tend to have lower conductance than pristine nanotubes, but stacking of defects can have counterintuitive effects. Theoretical modelling of semimetallic $(12,0)$ nanotubes showed that large defects consisting of 4 and 6 vacancies can have higher conductance than smaller defects made up of 2 vacancies [30]. In metallic $(10,10)$ SWNTs, simulations have shown that substitutional boron and nitrogen impurities have little effect on the overall conductance at the Fermi level while single and double vacancies significantly reduce conductance at the Fermi level [31]. The effects of long and short range disorder are also substantially different for semiconducting and metallic SWNTs. Short range disorder, such as that caused by a vacancy in the lattice of the nanotube sidewall, has a strong effect on both metallic and semiconducting SWNTs but long range disorder, such as that caused by a localized charge near the nanotube, only significantly affects semiconducting nanotubes [32]. Long range disorder from localized charges essentially breaks the semiconducting SWNT up into a set of quantum dots arranged in series and separated by tunnel barriers.

In the case of a MWNT resting on the surface of an electrode or of multiple MWNTs laying across each other in a network, typically only the outer wall of the nanotube is in contact and the inner layers play little role in conduction. In fact, it has been predicted that a MWNT will exhibit almost identical electrical conduction if the inner tubes are removed [33]. Intershell transport is not, however, forbidden and it has been shown that conduction through a MWNT with electrodes connected to different shells is only about half as high as when the electrodes are both connected to the outer shell [33]. It is also possible for all layers of a MWNT to carry electrical current, which greatly increases the conductivity. This has been demonstrated by growing a MWNT directly onto the electrode and welding the free end of the nanotube to an AFM tip [34].

1.4.3 Irradiation of Carbon Nanotubes

The effects of radiation exposure on the structure and properties of CNTs have been explored in great detail for some types of irradiation but they have been largely neglected for other types. The effects of irradiation by electron beams have been characterized in great detail, partly because many microscopy techniques utilize these beams and partly because it has been shown that beneficial modifications to the molecular structure are possible by this method [35-40]. The effects of ion bombardment of CNTs have also been studied, largely due to the nanoscale structural modifications that result [41, 42].

It has been shown that irradiation of carbon nanotubes results in many different types of changes to their microstructure, depending on the type, energy, dose, and dose rate of radiation and on the type and morphology of the carbon nanotubes being irradiated. The most common defects induced by irradiation are vacancies and interstitials [43]. The threshold energy required to break the carbon-

carbon bonds to knock an atom out of its position in the lattice of a carbon nanotube side wall is estimated to be around 13-20 eV [44-46].

Carbon nanotubes have a unique ability to heal radiation damage by rearrangement of the local microstructure to saturate energetically unfavorable dangling bonds [47]. This results in complex rearrangements of the lattice, local decreases in nanotube diameter, and bends or kinks. Pentagon/heptagon Stone-Wales defects can be caused by incomplete annealing after annihilation of a Frenkel pair [48]. These defects manifest themselves as a rotation of a bond in the lattice. When SWNT bundles or MWNTs are irradiated, a number of more complex defects can be generated. SWNTs in a bundle can be cross-linked when vacancies are formed in adjacent nanotubes. Similarly, covalent bonds can be formed between the layers of a MWNT.

This work focuses on neutron and gamma irradiation, which differ from electron and ion beams in that they have no charge, and are therefore unable to interact with matter by means of the Coulomb force [6]. As with electron and ion irradiation, some of the research into the effects of gamma irradiation on carbon nanotubes was motivated by the structural improvements that can be made by specific exposure. Another context under which these effects have been studied is that of aerospace applications, where components are exposed to cosmic rays. Generally, the effect of gamma irradiation on the microstructure of carbon nanotubes is manifested by the generation of defects in the lattice [49, 50]. These defects in the side walls of CNTs are known to aid in the formation of functional groups [49, 51]. It has also been found that exposure to gamma rays can reduce the interlayer spacing of MWNTs and improve their graphitization [52]. MWNTs have been shown to be more robust to gamma rays than SWNTs [49, 53].

Due to the changes in molecular structure resulting from gamma irradiation, there are significant changes in the electrical and mechanical properties of the carbon nanotubes. It was found that the elastic modulus and electrical conductivity of SWNTs both increase with increasing gamma dose until the SWNTs become saturated with defects at 170 kGy, after which point increasing exposure to radiation reduces both properties [54]. The initial increases in the electrical conductivity and elastic modulus are attributed to the formation of cross-links between the nanotubes, which are formed when the broken carbon bonds on the nanotube surface are closed. Similar experiments showed increasing strength and elastic modulus as well as decreasing strain at break for SWNT yarns after irradiation [55]. The saturation dose was confirmed to be in the general vicinity of 100kGy. Gamma irradiation of SWNTs has been shown to result in n-type doping via radiolysis of adsorbed water [56].

The effects of neutron irradiation on carbon nanotubes is a particularly under-investigated field. Compared to other types of radiation, relatively little is known about how neutron bombardment affects carbon nanotubes. Some insights can be gained by irradiation experiments undertaken on other carbon allotropes. It was found that, following neutron bombardment, fullerenes C_{60} and C_{70} had a tendency to coalesce into dumbbell-shaped carbon nanostructures C_{121}, C_{131}, and C_{141} [57]. Neutron irradiation damage in graphite has been studied extensively due to its usefulness as a moderator in nuclear reactors. A reduction in thermal conductivity of graphite caused by phonon scattering at vacancies and interstitial defects generated by neutron bombardment has been well documented [58-60]. Irradiated graphite also exhibits an increase in electrical resistivity, dynamic shear and Young's modulus, and critical stress intensity factor [61]. The strength of carbon fibers have been shown to increase with exposure to neutron bombardment [62].

1.4.4 Carbon Nanotube Based Sensors

The first field effect transistor (FET) using a carbon nanotube as the semiconducting path between electrodes was fabricated in 1998 [63]. Since then the sensitive electrical properties of CNTs have prompted the adaptation of CNT-based electrical devices for sensing applications of many types. They have been used for ultra-sensitive gas sensors [64-68], biomolecule and DNA sensors [69, 70], light sensors [71], gamma ray sensing and dosimetry [72-75], and proton radiation sensing [76]. Graphene has also been investigated for radiation sensing applications [77-80].

Tang et al. fabricated FETs by growing an individual SWNT across the source and drain for gamma ray sensing [72]. The substrate consisted of a p-doped silicon wafer coated with a 500 nm layer of SiO_2. The electrodes were patterned with W/Pt and the SWNTs were grown across the 3 μm gap by chemical vapor deposition on 1 μm x 1 μm catalyst islands. Two types of devices were made: tube-on-substrate and suspended tube. The gate voltage was applied through the p-doped silicon substrate and the source-drain bias was 10 mV. The CNTFETs were exposed to 6 MV photons with doses of up to 6.44 cGy and the sensitivity was found to be orders of magnitude higher than for conventional MOSFET dosimeters, especially for the suspended tube type [72].

Kang et al. [74] irradiated semiconducting SWNT films with 6 and 15 MV X-rays, measuring changes in electrical resistivity to determine exposure dose. Gold electrodes were deposited onto a glass substrate with a gap length of 1 cm. The SWNTs were suspended in an aqueous surfactant solution and deposited onto the patterned substrate using the vacuum filtration method. Real time resistivity measurements revealed that the resistance dropped rapidly when exposed to X-rays and rose rapidly when the X-ray was turned off. The change in resistivity was shown to be quasi-linearly proportional to the dose rate, indicating promise for dosimetry applications.

Lobez et al [75] fabricated a gamma ray dosimeter based on changes in the electrical properties of a MWNT/functionalized poly(olefin sulfone) composite. MWNTs were dispersed near the percolation threshold in the polymer so that they formed a nearly conductive network partially broken up by small regions of separation by the insulating polymer. The mechanism of detection was that gamma rays cause depolymerization of the matrix, resulting in lower resistance between the MWNTs. The composite was cast as a thin film on a glass substrate and gold electrodes were sputtered on the film with a spacing of 1.5 mm. The non-reversible increase in conductivity exhibited by these devices after irradiation doses of $5x10^3$ rad and $5x10^6$ rad can be utilized for gamma ray dosimetry.

Foxe et al [78, 79] designed and simulated a graphene FET capable of detecting neutron radiation via a boron conversion layer. The boron conversion layer absorbs neutrons and emits alpha and gamma irradiation. They also created a prototype device and showed that irradiation with alpha particles has an effect on the Dirac curve of their FET.

A thorough review of the published literature revealed that there has never been a neutron dosimeter using carbon nanotubes as the sensing elements.

2. Experimental Procedure

2.1 Sample Fabrication

The dosimeters consist of a randomly dispersed two dimensional network of carbon nanotubes spanning the gap between two metal electrodes as shown in Figure 4.

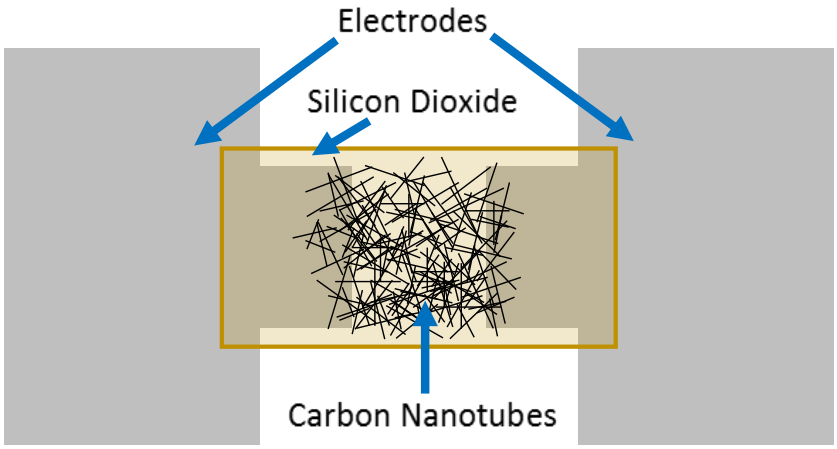

Figure 4: Device Layout.

The carbon nanotubes are sealed from air by a thin layer of silicon dioxide while the electrodes are exposed so that electrical contacts can be made. By applying a voltage across the electrodes, the electrical resistance of the CNT network can be measured. The changes to this electrical resistance due to exposure to radiation allow for the measurement of dose.

The sample fabrication process begins with purification of the carbon nanotubes, followed by patterning of electrodes then deposition of the carbon nanotubes. Once the device is coated with CNTs, they are sealed in place with a layer of silicon dioxide. Two types of samples were fabricated, one with SWNTs and the other with MWNTs.

2.1.1 Materials

The substrate is a four inch diameter ultra-high purity UV grade fused silica glass (Corning 0F 7980 HPFS). This material was chosen for its very high elemental purity and electrical resistivity. Because the devices are being exposed to extremely high doses of neutron radiation, it is essential that all materials used contain very few metallic impurities. Otherwise, the devices may become highly radioactive, which would delay or prevent post-irradiation analysis.

Table 2 lists the dimensions and purities of the carbon nanotubes, which were purchased from Cheap Tubes, Inc.

Table 2: Carbon nanotube specifications.

Tube Type	Item #	Outer Diameter	Length	Purity
SWNT	0101	1-2 nm	5-30 µm	>90%
MWNT	030111	12-18 nm	3-30 µm	>99%

2.1.2 Carbon Nanotube Purification

Because the devices are subject to extremely high neutron radiation fluences, it is essential that all materials are extremely pure. In previous experiments that exposed CNTs to similar neutron fluences, activation of impurities was reported to cause delays of over three months before samples could be free-released [56]. Although the purchased CNTs were purified by the vendor, examination with transmission electron microscopy (TEM) and energy-dispersive X-ray spectroscopy (EDX) revealed that even the nominally 99% pure nanotubes contained a significant amount of cobalt impurities. Cobalt is used as a catalyst to grow the carbon nanotubes, and it is very difficult to remove because it is often encapsulated within the nanotube or in layers of graphite or amorphous carbon [81, 82].

Figure 5 shows one such encapsulated cobalt impurity. The parallel lines wrapping around the impurity are the multiple walls of a MWNT.

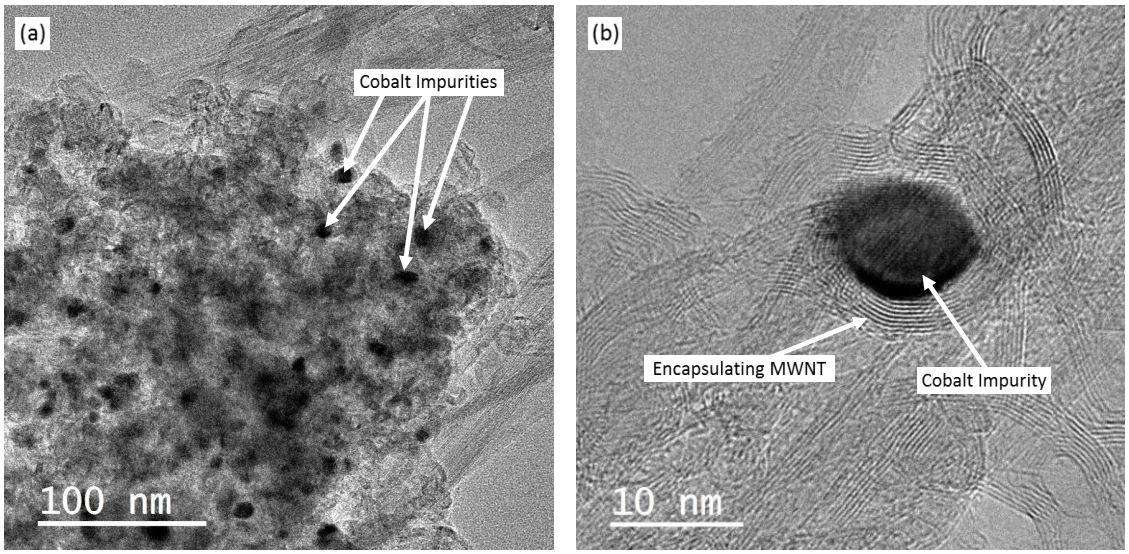

Figure 5: TEM micrographs of as-received 99% pure MWNTs. (a) MWNT agglomerate containing cobalt impurities and (b) close up of cobalt impurity encapsulated in a MWNT.

Figure 6 shows an energy-dispersive X-ray spectroscopy (EDX) map of a bundle of as-received 99% pure MWNTs. Areas where carbon atoms are present are colored red and areas where cobalt atoms are present are colored green.

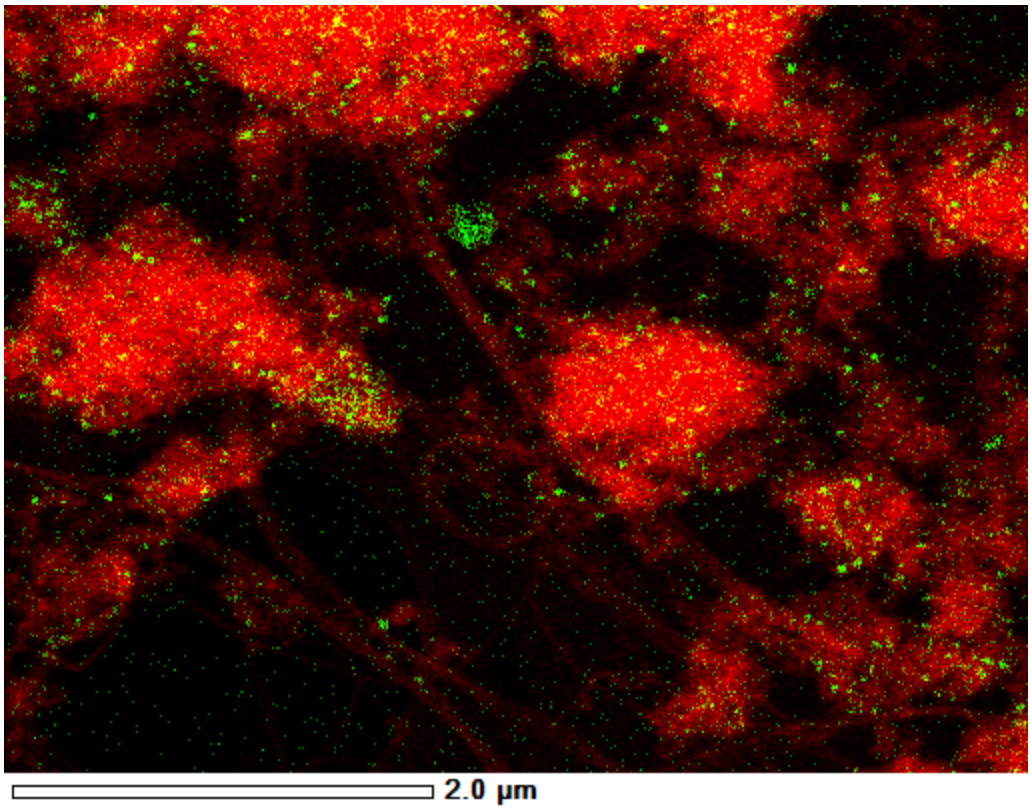

Figure 6: EDX map of as-received 99% pure MWNTs. Red indicates carbon and green indicates cobalt.

To prevent activation of the devices, a rigorous purification technique was developed to ensure that practically all metallic impurities were removed. In order to remove these impurities it is necessary to first release them from the encapsulating graphite or nanotubes. To this end, the CNTs were first baked in a tube furnace in air for 2 hours at 500 °C to selectively burn off amorphous carbon and in some cases to burst the carbon encapsulate by thermally expanding the metallic impurities.

After baking, the nanotubes were dispersed in a small amount of deionized water via tip sonication at 40% power for 5 minutes in order to debundle the large agglomerates. They were then refluxed in high concentration (69.3%) nitric acid in a laboratory microwave (CEM Discover) at 150 W at atmospheric pressure. Because the microwave energy is preferentially absorbed by the metallic impurities, local

temperatures around them can grow to many times the boiling point of the acid, selectively accelerating the reaction in those regions. As such, microwave assisted acid reflux can target impurities specifically without causing additional damage to the nanotubes themselves. After refluxing, the solution was diluted with DI water and vacuum filtered through 0.65 µm pore size cellulose nitrate membrane filters, rinsed with a liter of DI water, and dried in an oven at 70°C for 2 hours. Figure 7 shows EDX maps of the nanotubes before and after purification. It can be seen that there is no cobalt (represented in green) present after purification.

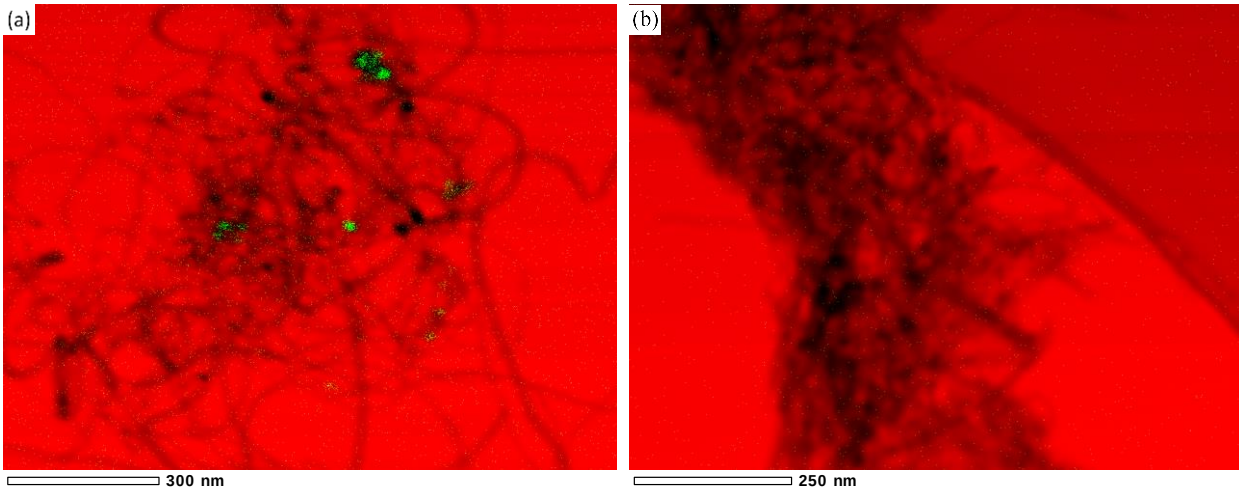

Figure 7: EDX map of (a) CNTs before purification and (b) after purification. Black indicates carbon and green indicates presence of cobalt.

After searching rigorously under TEM for hours, no trace of cobalt could be found in the purified carbon nanotubes. The extremely high purity was further confirmed by the lack of measurable radioactive cobalt isotopes after neutron irradiation.

Unlike the MWNTs, the SWNTs contained substantial amorphous carbon impurities that required an additional purification step to remove. Figure 8 shows Scanning Electron Microscope (SEM) micrographs

of a SWNT and MWNT network. It can be seen that the SWNT network has substantial amorphous carbon contamination while the MWNT network contains only nanotubes.

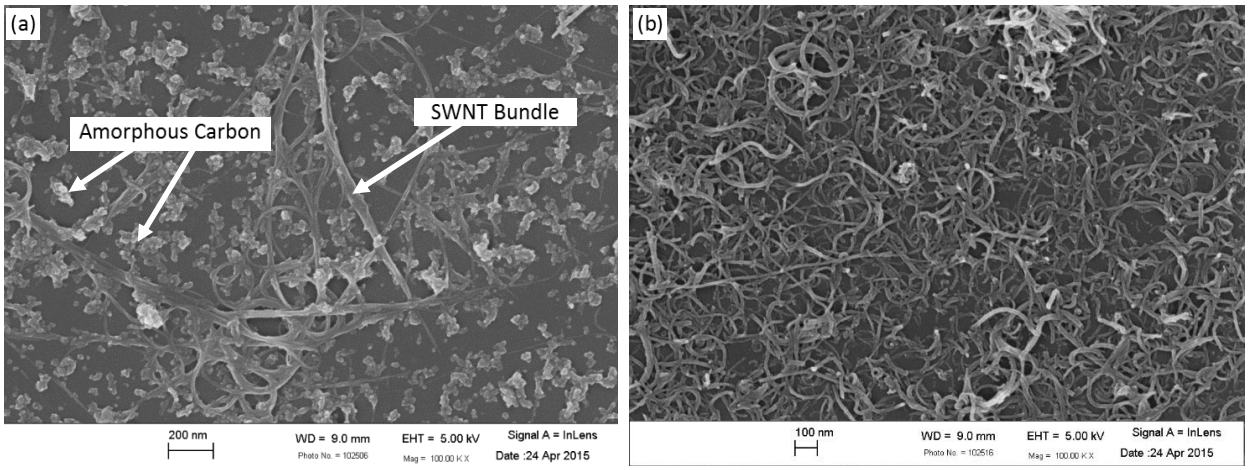

Figure 8: SEM micrograph of (a) SWNT network containing amorphous carbon and (b) MWNT network free from amorphous carbon.

To remove the amorphous carbon from the SWNTs, they were first dispersed in a solution of 1 wt% sodium dodecyl sulfate (SDS), an anionic surfactant, in deionized water to form a 5 µg/g mixture. The mixture was tip sonicated for 2 minutes at 20% power then bath sonicated in an ice bath for 2 hours. The mixture was then centrifuged at 8800 g for 2 hours. The amorphous carbon does not dissolve as well in the solution and aggregates at the bottom of the centrifuge tube while the pure SWNTs remain dispersed. The top 50% of the solution in the centrifuge tubes was decanted, vacuum filtered through 0.65 µm pore size cellulose nitrate membrane filters, rinsed with a liter of DI water, and dried in an oven at 70°C for 2 hours. Figure 9 shows SEM micrographs of SWNTs before and after centrifugation. While there is still some amorphous carbon present, it is greatly reduced.

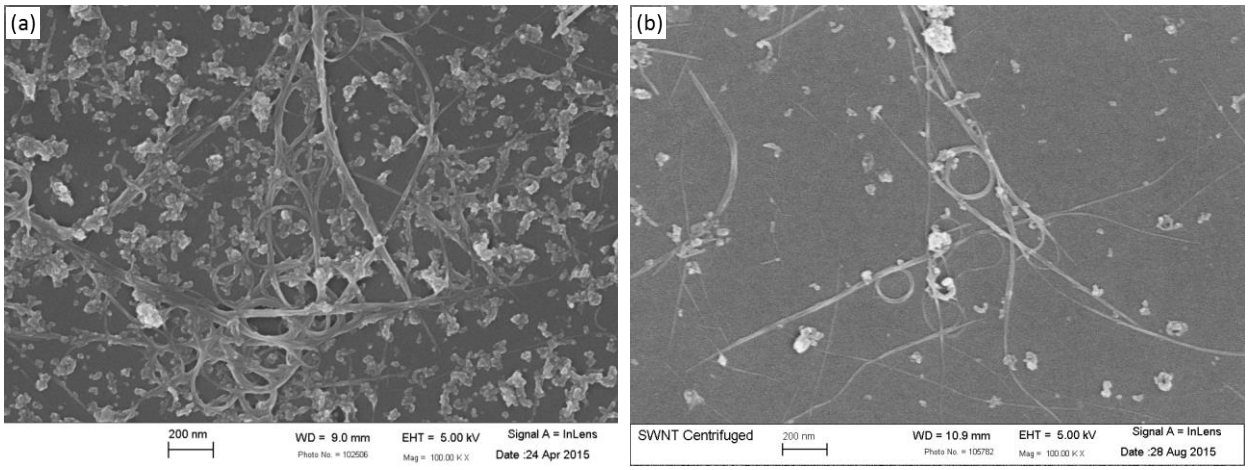

Figure 9: SEM micrograph of SWNTs (a) before centrifugation and (b) after centrifugation.

2.1.3 Electrode Patterning

The dosimeters were fabricated in the Virginia Tech Electrical and Computer Engineering (ECE) Micro and Nano Fabrication Laboratory (MicrON) clean room using wafer processing techniques such as those utilized by the semiconductor industry to make integrated circuits. The advantages to this approach are that it is extremely precise, allowing feature sizes as small as 7 µm, and that it is a batch processing technique that is very scalable, meaning that this design is immediately ready for low-cost mass production. Also, since over 800 devices can be simultaneously fabricated on a single wafer, the risk of inconsistencies due to variations in processing conditions is greatly reduced.

Electrodes were patterned onto the 4" diameter fused silica wafer via lift-off, an additive microstructuring technique that uses a sacrificial layer of photoresist. Photoresist is a light-sensitive material that is used in photolithography. Exposure to UV light causes photoresist to undergo chemical changes that make it soluble in a developing solution.

To pattern the electrodes, the wafer was first washed in acetone, alcohol, and water to remove any particles from the surface. Then photoresist was spin-coated onto the wafer. The photoresist used in all photolithography steps for this device was Microposit SC 1827. Once the wafer was coated in a uniform layer of photoresist, it was exposed to UV light, which was partially blocked in the desired pattern by a photomask in a MA6 mask aligner system. Figure 10 shows the photomask that was used to pattern the electrodes.

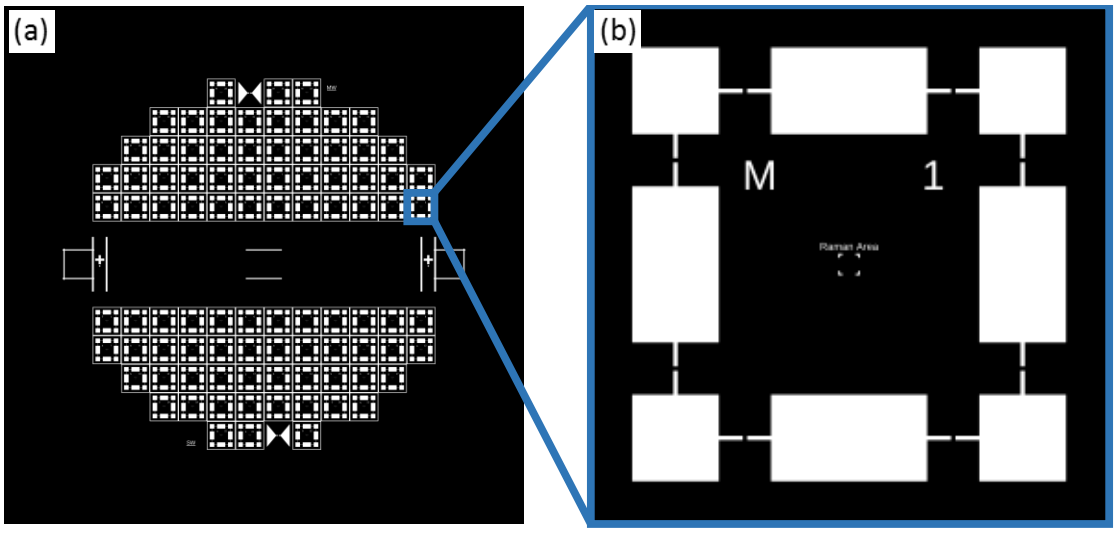

Figure 10: (a) Photomask for electrodes and (b) close up of one sample containing eight devices.

A photomask is a printed pattern on transparent film or glass. Light is blocked by the black portions and passes through the transparent portions (white portions in Figure 10), causing the photoresist to become soluble in developing solution in those areas. Washing the wafer in developer removes photoresist only from the spaces that were exposed to light, thereby transferring the photomask pattern to the wafer, as shown schematically in Figure 11.

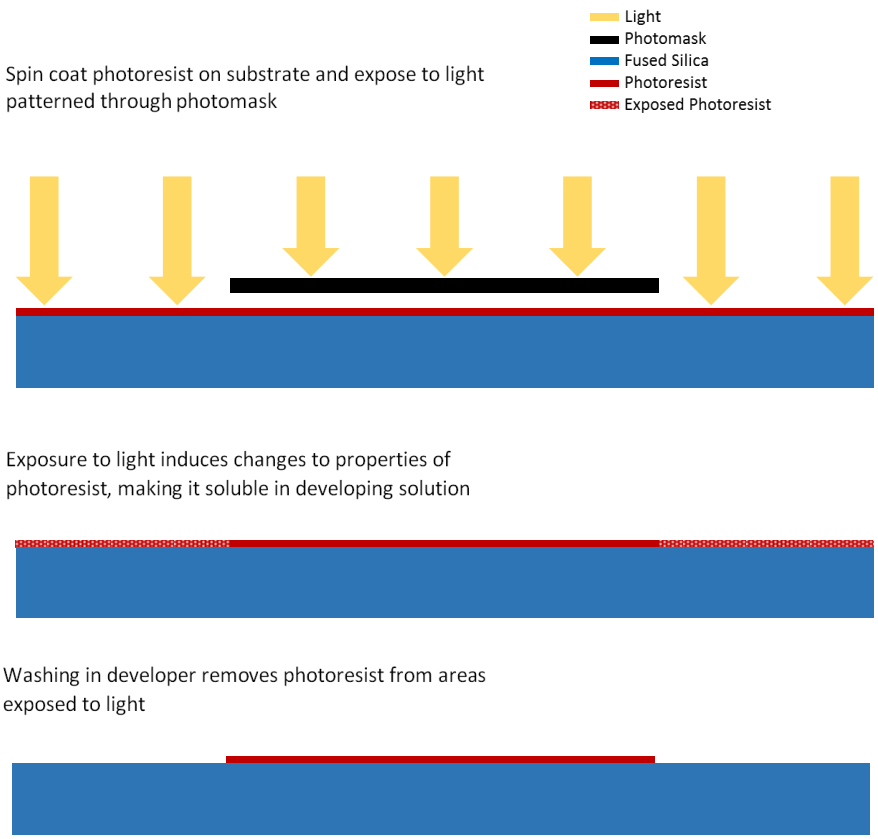

Figure 11: Schematic of photolithography process

Once the photoresist was patterned, the electrodes were deposited via e-beam. Nickel was chosen for the electrode surface because of its resistance to oxidation and the fact that it does not activate into any particularly long-lived isotopes upon neutron irradiation. Nickel, however, does not adhere well to fused silica, so an adhesion layer of titanium was deposited first. A 20 nm thick layer of titanium was deposited over the patterned photoresist, followed by a 130 nm layer of nickel. The electrodes were patterned by the lift-off method as shown in Figure 12.

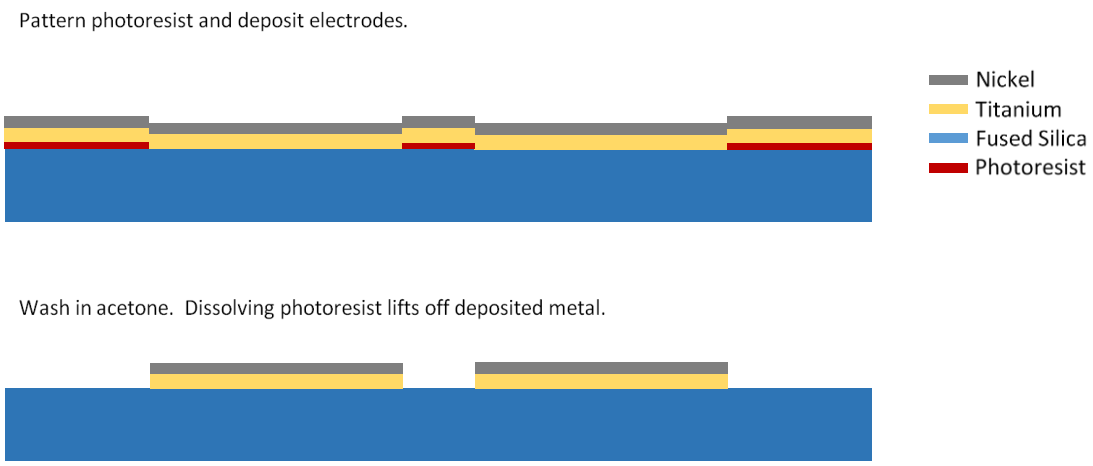

Figure 12: Schematic of liftoff process.

Figure 13 shows the wafer after deposition of electrodes. The two dark quadrants are regions where a layer of boron was first deposited, and will be discussed in more detail later.

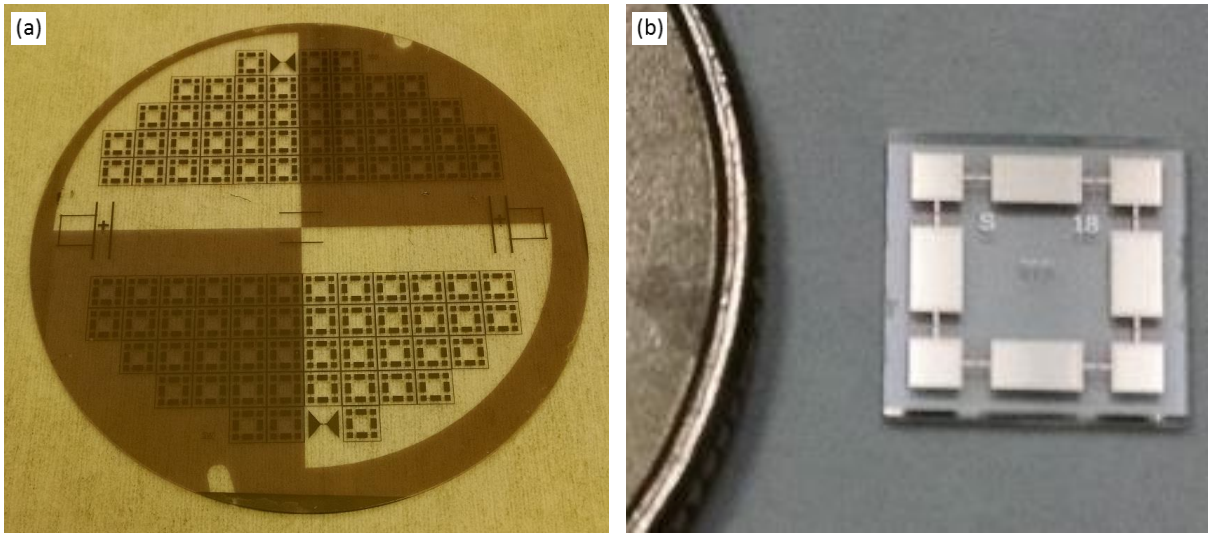

Figure 13: (a) Wafer after electrode patterning and (b) close up of individual sample.

2.1.4 Carbon Nanotube Deposition

Once the electrodes were patterned onto the substrate, the purified CNTs were deposited using an airbrush technique. Like photolithography, this approach is well suited for batch processing, and it

results in a uniform random network of carbon nanotubes. First the nanotubes were mechanically mixed into dimethylformamide (DMF) at a concentration of 0.1 mg/ml. They were then tip-sonicated at 40% power for half an hour using a pulsed pattern of 10 s on followed by 10 s off. After tip sonicating they were continuously sonicated in a bath sonicator throughout the deposition process. The substrates were fixed to a sheet of aluminum foil placed over the surface of a hot plate set to 150°C and the CNT/DMF solution was sprayed onto the surface using a Master Performance (model G22) multi-purpose dual-action gravity feed airbrush with a 0.3 mm tip. This handheld air brush sprays a fine mist of solution onto the substrate, at which point the solvent is quickly evaporated, leaving behind a layer of CNTs on the surface of the substrate. The nanotubes were deposited layer by layer, allowing the solvent to fully evaporate after each spray, until a randomly distributed network of nanotubes was deposited. After every 10 layers, the electrical resistance between electrodes was measured with a multimeter. The process was repeated until the multimeter was able to detect current flow, indicating that the percolation limit had been reached and a conductive path had been established by the network of nanotubes between the electrodes. Figure 14 shows SEM micrographs of the resulting MWNT and SWNT networks.

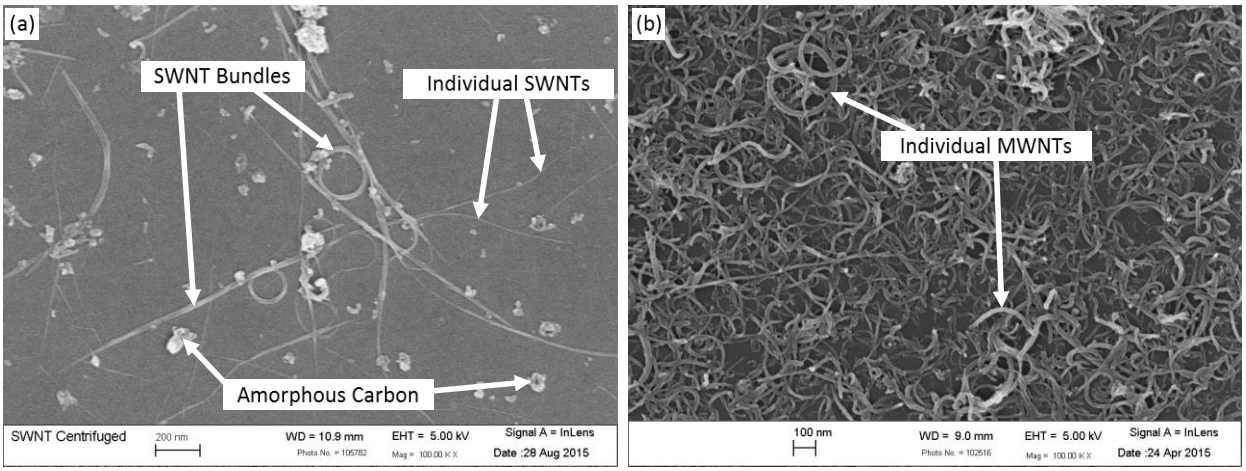

Figure 14: SEM micrographs of dispersed networks of (a) SWNTs and (b) MWNTs.

These micrographs show that the MWNT network is well dispersed with virtually no bundling or amorphous carbon content while the SWNT network is highly aggregated, forming entangled ropes, and there is some amorphous carbon present.

2.1.5 Sealing with Silicon Dioxide

After spray coating, the nanotubes are exposed to air and are loosely attached to the substrate by van der Waals forces. They must be handled carefully because brushing the surface can disturb their position or wipe them completely off. Additionally, they adsorb chemicals from the air, including water vapor and oxygen, which can affect the electrical properties of the device and influence the effects of irradiation. For these reasons, it is essential to seal the nanotubes onto the substrate and away from the air. This was accomplished by coating them with a 2 µm layer of silicon dioxide. The process is shown schematically in Figure 15.

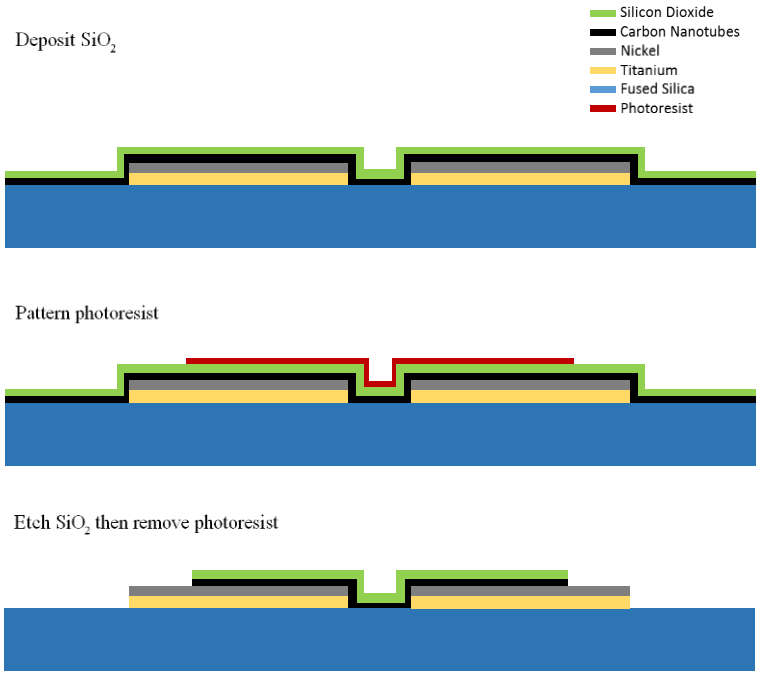

Figure 15: Schematic of silicon dioxide patterning.

First, the wafer was held under vacuum for 1 hour while the temperature was ramped up to 300 °C in order to desorb as much water as possible from the nanotubes. Then the silicon dioxide layer was grown via Plasma Enhanced Chemical Vapor Deposition (PECVD). Next, the silicon dioxide had to be selectively removed from the electrodes in order to measure the resistance. To accomplish this, photoresist was patterned over the areas where nanotubes needed to remain sealed, as shown in Figure 16.

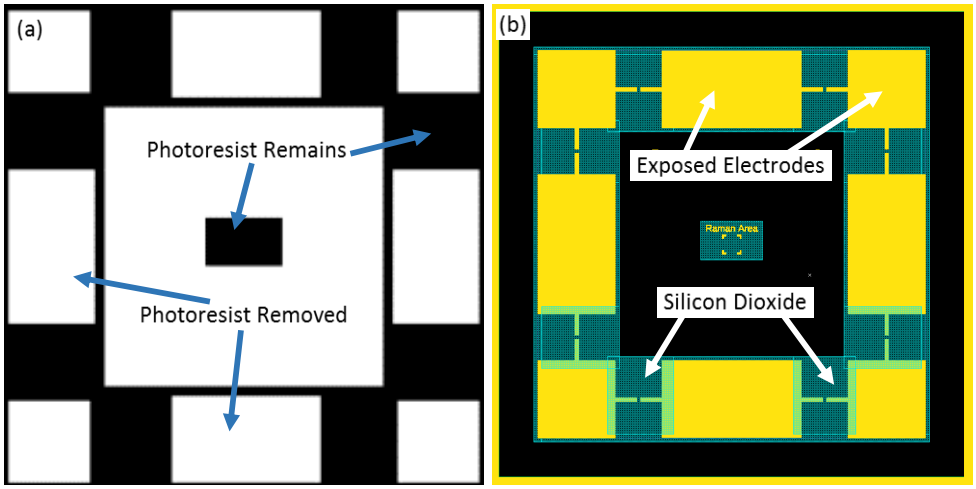

Figure 16: (a) Photomask for silicon dioxide patterning and (b) resulting device diagram.

After patterning the photoresist, the silicon dioxide was etched in a buffered hydrofluoric acid solution. The areas protected by photoresist were not etched while the exposed silicon dioxide was removed. The photoresist was then removed, finalizing the fabrication of the devices. Figure 17 shows an optical microscope image of a finalized device.

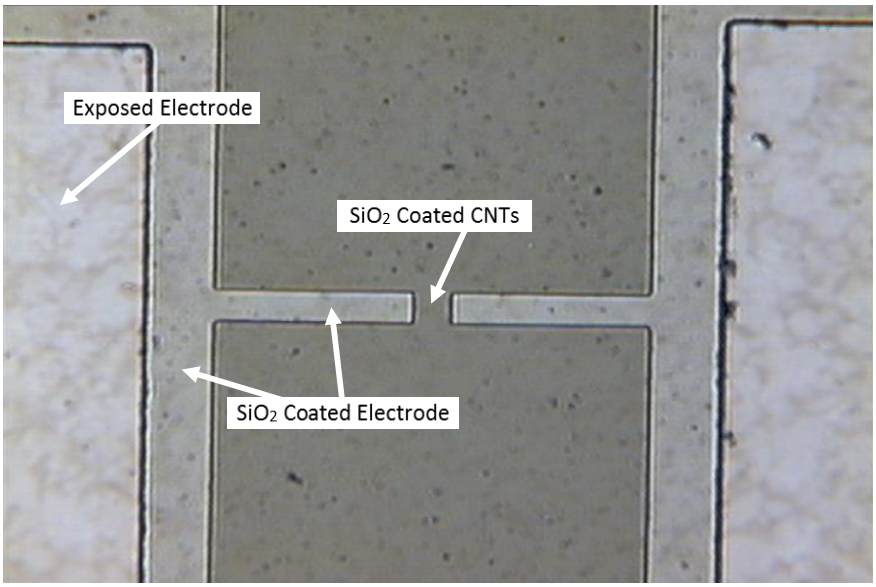

Figure 17: Optical microscope image of device.

The final step before irradiation was to dice the individual samples apart from each other using an automated dicing saw. Final sample dimensions were 6.3 mm x 6.3 mm with 8 devices per sample.

2.2 Irradiation

The samples were irradiated in the PT-1 pneumatic tube system at the High Flux Isotope Reactor (HFIR) at Oak Ridge National Lab (ORNL) in Tennessee. Located in the permanent beryllium reflector about seven inches from the fuel element, as show in Figure 18, PT-1 exposes samples to both neutron and gamma radiation.

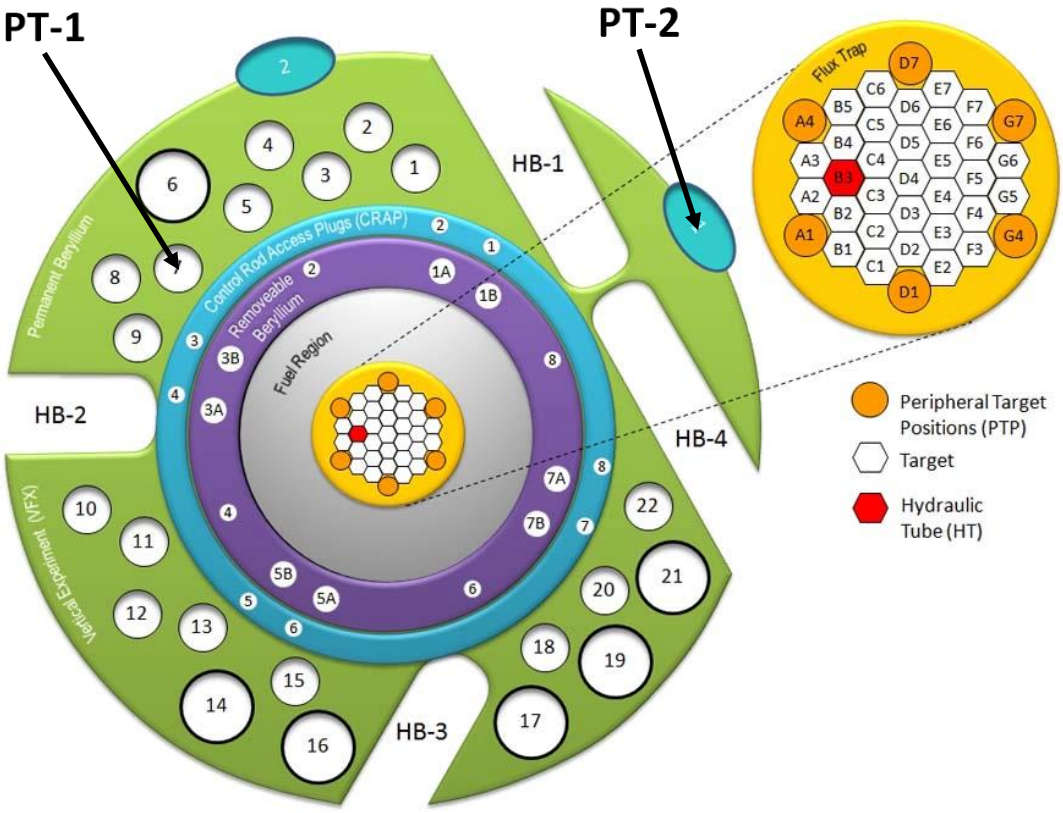

Figure 18: Schematic of HFIR core assembly [83]. (Image used under Fair Use)

PT-1 has a thermal neutron flux of 4.43×10^{14} n/cm^2-s and a thermal/epithermal ratio of 47.7. The gamma ray exposure rate is 4.5×10^5 rad/s with an average gamma ray energy of 1.3 MeV. Samples were placed into small high-density polyethylene cylindrical containers called "rabbits" that fit in the pneumatic tube assembly. The rabbits were packed with helium prior to irradiation to prevent oxidation of electrodes. Samples were irradiated for 30, 60, and 120 seconds for total thermal neutron fluences of 1.329×10^{16}, 2.658×10^{16}, and 5.316×10^{16} n/cm^2 and total gamma doses of 1.35×10^7, 2.7×10^7, and 5.4×10^7 rad. The neutron and gamma radiation energy spectra are shown in Figure 19 and Figure 20, respectively.

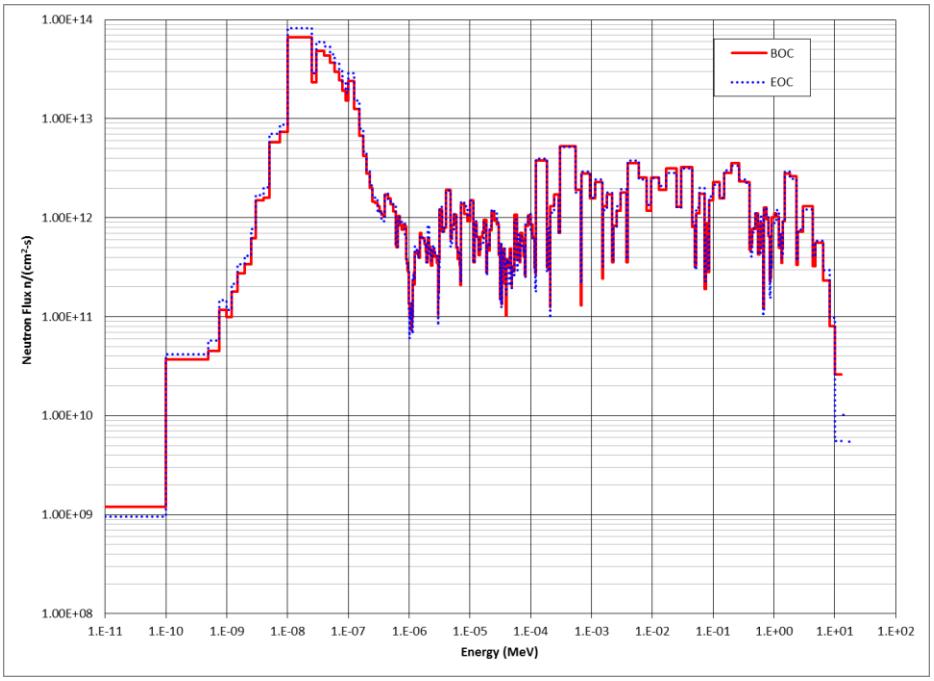

Figure 19: Neutron energy spectrum for HFIR PT-1.

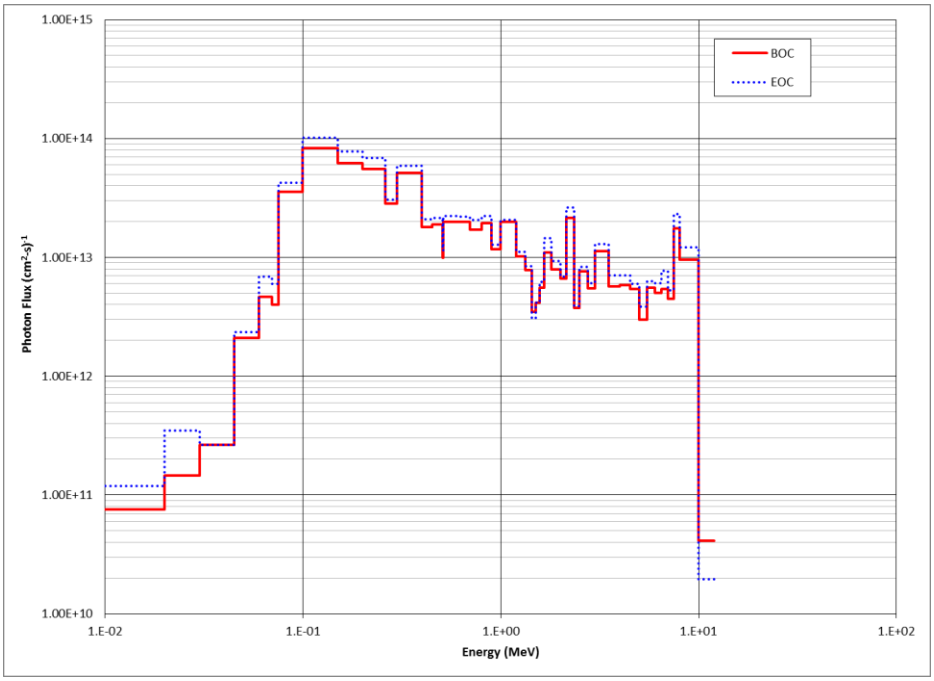

Figure 20: Gamma energy spectrum for HFIR PT-1.

After irradiation in HFIR, the samples had become radioactive and were stored in a designated area until they had decayed to releasable activity levels. This decay period was about 2 weeks and during this time they were kept sealed in their rabbits in a helium environment.

Since HFIR PT-1 exposes samples to both neutrons and photons, it is necessary to differentiate between the effects of the two types of radiation. To this end, another set of samples were irradiated at equivalent pure gamma doses in the HFIR Gamma Irradiation Facility (GIF). The GIF is located in the spent fuel pool of HFIR, where samples are placed in the center of a spent fuel assembly. Because the gamma rays are generated by radioactive decay, the dose rate changes over time, but for these experiments it was around 6700 rad/sec. An argon sweep gas was used to prevent oxidation of the samples during irradiation.

2.3 Characterization

To determine the effects of irradiation, the devices were characterized before and after exposure to radiation. In addition to the irradiated samples, the properties of a control sample were measured at the same time to account for any changes unrelated to irradiation that occurred over the 2 week decay period. For each of the two radiation environments, HFIR and GIF, there was one sample for each radiation dose. Each sample contained 8 dosimeters so that statistical data could be collected at each radiation dose point. Characterization included measuring changes to electrical properties by recording the DC resistance and measuring changes to the microstructure of the nanotubes via Raman spectroscopy. Also, separate devices were exposed to various humidity environments in order to characterize the effects of adsorbed water vapor on the electrical properties. The effects of thermal annealing on the electrical properties of the devices were investigated as well.

2.3.1 DC Electrical Resistance

Changes in the DC electrical resistance of the CNT network are the primary method by which the dosimeter operates. It is an attractive sensing method because it is simple and cheap to detect and can provide real time information. The electrical properties of randomly oriented CNT networks are the result of the interaction of nanotubes with a range of electrical properties, chiralities, lengths, and diameters, all with different levels of radiation damage.

A SemiProbe Lab Assistant manual probe system was used to make electrical contact with the devices, as shown in Figure 21. It allows precise manipulation of the probes viewed under a microscope in order to verify contact with the 1 mm^2 electrode pads.

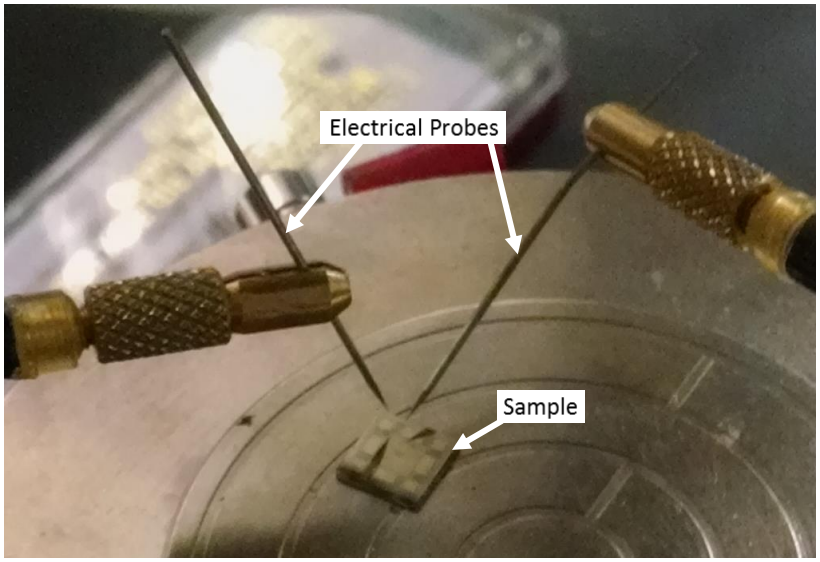

Figure 21: Electrical properties characterization configuration.

The DC electrical resistance was measured for eight dosimeters for each dose before and after irradiation. The resistance of 8 control devices were also measured at the same time as the irradiated

devices, both before and after, in order to account for unrelated effects such as differences in temperature, humidity, and system calibration.

2.3.2 Raman Spectroscopy

Raman spectroscopy is a spectroscopic technique that relies on inelastic scattering of monochromatic light to investigate material systems at a molecular level [84]. When light is scattered by an atom or molecule, most photons are scattered elastically through a process called Rayleigh scattering. In elastic scattering, the frequency of the reflected light is the same as that of the incident light. About one in every 10^6-10^8 photons, however, is scattered inelastically via an excitation in which the frequency of the scattered photon is different from that of the incident photon [84]. This frequency shift can reveal important details about the molecular structure of the material under investigation.

Scattering of light occurs when a photon interacts with a molecule, distorting the electron cloud to form a short lived (virtual) state that emits a photon when it relaxes to a vibrational state. After being excited to a virtual state by interaction with a photon, the molecule will usually return to its original vibrational state, emitting a photon with the same energy as the incident photon. This is what occurs during Rayleigh scattering. At room temperature, the majority of molecules are in the lowest energy vibrational state. Sometimes these molecules do not relax back to the ground state after interaction with a photon, but instead absorb some of its energy and relax to a higher energy vibrational state. In this case, the photon emitted has lower energy (and lower frequency) than the incident photon. This phenomenon is called Stokes scattering [84]. It is also possible for a molecule which is already in an excited vibrational state to return to the ground state after interaction with a photon, emitting a photon of higher energy than the incident photon. This is called anti-Stokes scattering [84]. The change in

frequency resulting from Raman scattering, referred to as the Raman shift, reveals the characteristics of the vibrational modes of a molecule, which are strongly linked to molecular structure.

In Raman spectroscopy, the sample is exposed to monochromatic light in the UV, visible, or near infrared (NIR) region and the intensity of the scattered light is collected as a function of the Raman shift. Most Raman spectroscopes use a visible or NIR laser for excitation and in this work an excitation frequency of 532 nm was used. The absolute values of intensity are generally unimportant in the study of Raman spectra. The useful quantities are the relative intensities, width, and location of the peaks. Figure 22 shows a typical Raman spectrum for single wall carbon nanotubes with some of the most significant peaks labeled.

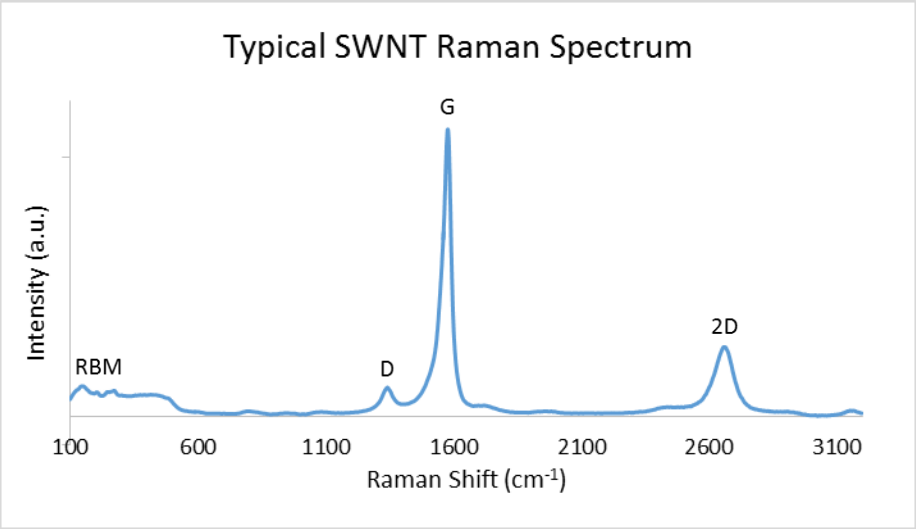

Figure 22: Typical SWNT Raman spectrum.

Raman spectroscopy has been used extensively in the study of carbon nanotubes due to its ability to quickly and accurately reveal a number of important nanotube characteristics. Table 3 lists the most common features in Raman spectra of SWNT and the frequency range at which they usually occur.

Table 3: Notable features of SWNT Raman spectra [85, 86]

Name	Location, cm^{-1}	Relevant Nanotube Characteristics
RBM	100-350	Nanotube diameter
D	1250-1400	Defect concentration
G^-	1500-1600	Longitudinal strain
G	1500-1600	Long range ordering
G^+	1500-1600	In-plane transverse strain
2D	2600-2700	Lattice disorder due to doping

The first mode, occurring with frequencies between 100 and 350 cm^{-1}, is called the radial breathing mode (RBM) due to the fact that it corresponds with the coherent vibration of carbon atoms in the radial direction, expanding and contracting the tube as if it were breathing [85]. For SWNTs with diameter below 2 nm, the location of the RBM is inversely related to the nanotube diameter. For SWNTs with larger diameters, the radial breathing mode is so weak that it is practically unobservable [85]. In Figure 22, several distinct RBM peaks can be seen because the SWNT network is made up of nanotubes with various chiralities and diameters.

The D band is a disorder-induced double resonance feature usually occurring between 1250 and 1400 cm^{-1} in SWNTs [85, 86]. It arises from defects in the periodic carbon lattice of graphene, and both the peak height and linewidth have been shown to increase as more defects are introduced [86]. Since the end of a nanotube is by definition a defect in the graphene lattice, shorter nanotubes possess more pronounced D bands. For individual SWNTs the D band is a sharp peak while for SWNT bundles it takes on a multi-peak dispersed shape. The D band in metallic SWNTs is usually stronger in than in semiconducting nanotubes, but the exact cause of this phenomenon is not well understood [86]. Examination of the D band peak height and linewidth can provide an excellent qualitative understanding of structural damage to SWNTs. The position of the D peak is affected by chemical doping of the CNTs. Downshifts to the D peak position indicate n-type doping while upshifts indicate p-type doping.

The G band in SWNTs is caused by stretching of carbon-carbon bonds and it consists of several different peaks [86]. This feature is sensitive to strains in the graphene sheet, including the inherent strain generated by the curvature of the nanotube. The G^- peak occurs at a slightly lower frequency and is attributed to vibrations in the circumferential direction. Its line shape is sensitive to whether the nanotube is semiconducting or metallic. The G^+ peak, occurring at a slightly higher frequency, is associated with vibrations along the central axis of the SWNT and is sensitive to charge transfer from addition of dopants [85, 86]. Defects to the lattice structure cause increased splitting of the G band, reducing the main G band intensity. Since defects cause the intensity of the G band to drop at the same time that they cause an increase in the intensity of the D band, the ratio of these two peaks is a useful measure of overall damage to SWNTs.

The 2D band, sometimes referred to as the G' band, arises from a second order Raman scattering process involving two phonons [85]. It is the highest frequency Raman feature of much significance seen in SWNT. It typically occurs at a frequency between 2600 and 2700 cm^{-1} and contains useful information about nanotube chirality and doping [85].

Raman spectroscopy of MWNTs differs from that of SWNTs in a number of significant ways. Due to their large diameter and the fact that they consist of an ensemble of SWNTs with different sizes, the RBM is both very weak and very broad, making it usually unobservable in the spectra of MWNTs [85]. The splitting of the G band is also less obvious in MWNTs than it is in SWNTs, often characterized by a weakly asymmetric line shape with a peak near that of graphite around 1582 cm^{-1}. For both types of nanotubes, however, the ratio of the D and G bands provides a general qualitative description of defect concentration.

To characterize the Raman properties of the samples, a Renishaw micro Raman machine with automatic mapping capability powered by WiRE software was used. A 532 nm edge laser was used with an 1800 l/mm grating. Spectral data was collected in air from 1090 to 1888 cm^{-1} using a 20x objective lens. The equipment was calibrated each day with a silicon wafer. In an attempt to measure the Raman spectra in the exact same location pre- and post-irradiation, titanium/nickel alignment marks were patterned onto the substrate. Having measured 49 locations on each sample, statistical analysis on the data provided by the spectra was performed to examine the effects of irradiation on the structure of the nanotubes.

Curve fitting of the Raman spectra was performed automatically using the WiRE software after manually inputting approximate peak positions.

2.3.5 Humidity Analysis

It has been well established that ambient humidity affects the electrical properties of carbon nanotubes via adsorption of water molecules [87, 88]. Individual semiconducting SWNTs [63, 89] and networks of combined metallic and semiconducting SWNTs [90] have been shown through experiment and simulation to behave as p-type semiconductors. Individual MWNTs generally behave as conducting metals, but when flattened can act as p-type semiconductors [91]. It has also been shown that randomly oriented networks of MWNTs can act as p-type semiconductors [87]. The electrical resistivity of MWNT and SWNT networks tends to increase when exposed to water vapor [87, 88, 92]. This increase in resistivity has been attributed to water molecules adsorbing onto the surface of the nanotubes and donating electrons to the valence band, decreasing the number of holes.

The presence of water molecules can also have a significant effect on the reaction of the nanotubes to radiation. When exposed to gamma rays, water undergoes radiolysis, producing a number of byproducts such as H^+ and OH^- radicals that readily interact with and dope CNTs. It has been shown that trapped water molecules undergoing radiolysis can be a significant cause of damage to SWNTs irradiated by neutron and gamma irradiation [56].

Because of the effects of water molecules on the electrical and radiological properties of CNTs, it was necessary to measure the adsorption of water onto the nanotubes and characterize the effects on their properties. A vacuum chamber with internal electrical leads and a quartz crystal microbalance (QCM) was used for this analysis. Figure 23 shows a photograph and schematic of this environmental control chamber.

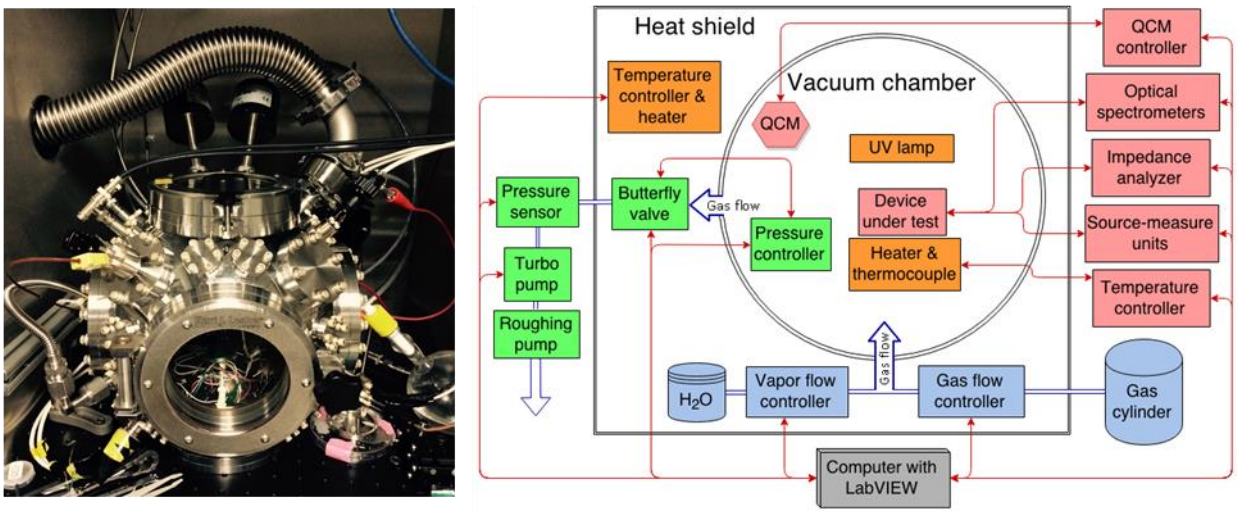

Figure 23: Photograph (left) and schematic (right) of the environmental control chamber.

This environmental control chamber was set up, instrumented, and run by Eric Muckley of the University of Tennessee. The spray coating technique was used to deposit a network of CNTs onto the surface of a gold coated quartz crystal (Inficon 5MHz gold coated crystal, item number 750-1005-G10) in order to

measure the amount of water adsorbed by the nanotube networks at various humidity levels. In the same batch, CNTs were deposited onto fused silica substrates and they were patterned with electrodes so that the effect of humidity on the electrical properties could be examined.

The crystals and fused silica samples were both placed into the vacuum chamber to degas over night at a pressure of 3.64×10^{-6} Torr. The humidity was controlled by allowing water vapor to enter the chamber in steps equivalent to 20% humidity. After each step, the humidity was maintained constant for 30 minutes in order to allow the CNT networks to equilibrate. The mass adsorbed was recorded continuously by the QCM and the DC electrical resistance was measured continuously by a 2 point probe.

2.3.6 Thermal Annealing

It has been demonstrated that CNTs possess the ability to self-heal structural defects by rearrangement of the local microstructure to saturate energetically unfavorable dangling bonds. Many defects are capable of self-healing at room temperature, but others are initialized only when a threshold energy is exceeded. Irradiation contributes to annealing in two ways. First, the radiation environment itself has an elevated temperature and second, interaction with radiation causes local energy transfer, which propagates easily along pristine sections of the CNTs but builds up at defect sites where thermal conductivity is lower. To investigate the effects of the addition of energy to the nanotube networks, non-irradiated devices were annealed in nitrogen for one hour at temperatures of 100, 200, 300, 400, and 500 °C. The electrical resistance was measured before and after baking. Exposure to temperatures above 550 °C begins to cause damage to the carbon nanotubes, which would overshadow any changes caused by thermal annealing.

3. Evolution of Design

The final devices described in Chapter 2 were the result of a lengthy and in-depth design process. They are the fourth generation of devices designed, fabricated, irradiated, and characterized during this study. Each design iteration served an important role in the design process and motivated specific changes to the features of the final device.

The first generation of devices were intended as a proof-of-concept, and as a way to evaluate the irradiation and characterization procedures. After a successful proof of concept, the fabrication process was greatly refined to make the second generation devices, which aimed to evaluate the effects of electrode dimensions and to test improved fabrication techniques. The third generation devices incorporated the lessons learned from the second generation and increased the number of devices per sample to allow for statistical analysis. The fourth and final iteration made changes to the electrode materials and irradiation conditions to prevent oxidation.

3.1 First Generation

The first generation devices were intended as a proof-of-concept and as a way to discover any unexpected obstacles in the irradiation and characterization process. They were fabricated using a relatively inexpensive approach that didn't require lengthy and expensive training on new equipment. The primary objective was to demonstrate that the idea was feasible before spending substantial time and resources training on advanced microfabrication techniques.

3.1.1 Design and Fabrication

The first device consisted of copper electrodes sputtered onto an ultra-high purity fused silica substrate that was then spray coated with a random network of CNTs. The fused silica was received as 1.0”x3.0”x0.5 mm slides which were then cut using a low-speed diamond saw into 0.7”x0.3” substrates. These dimensions were chosen to fit into the polyethylene rabbits used to pneumatically transport samples into the radiation environment.

Some substrates were then patterned with copper electrodes to allow repeatable measurement of electrical properties. The pattern was sputtered onto the substrates using a magnetron high vacuum sputtering system (AJA International ATC Orion). A polycarbonate stencil was used to block copper deposition in order to form the pattern. The stencil was laser cut from a polycarbonate sheet and the pattern was made by taping the stencil over the substrate and sputtering a 200 nm layer of copper through the holes in the stencil. Unlike the final design where the electrodes for around 100 samples were patterned in the same step, this first generation device required each sample to be patterned one at a time, which was much more time consuming, not as scalable for commercial production, and did not result in the same high consistency between samples. Figure 24 shows the design of the stencil, a photograph of the stencil, and a picture of a substrate that has been patterned with copper using this method. Each sample has 3 sets of electrodes referred to as small, medium, and big (top to bottom in Figure 24). The width of the electrodes and the gap between them was 100 µm for the small electrode, 200 µm for the medium electrode, and 300 µm for the big electrode.

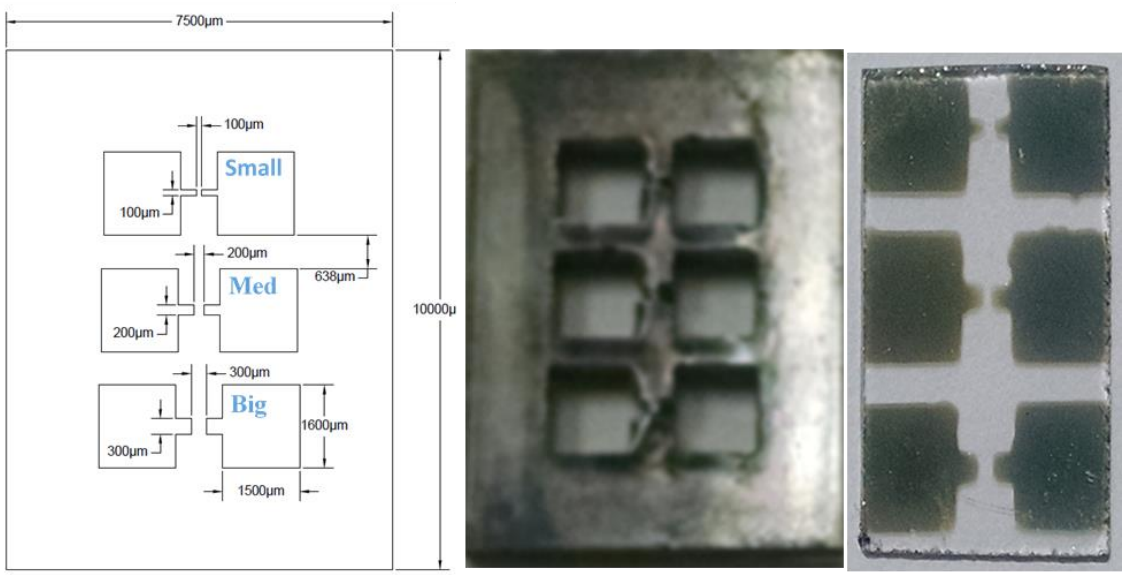

Figure 24: Stencil design (left), photograph of stencil (center), and photograph of resulting copper pattern (right).

The carbon nanotubes were deposited using the same spray coating method for all 4 generations of devices and the metallic impurities were removed using the same purification method throughout. In these first generation devices, however, the amorphous carbon was not removed from the SWNTs by centrifugation as they were in the final device.

To keep track of the samples, sample names were scratched into the back side of the substrate using a diamond tipped glass cutting hand tool.

3.1.2 Irradiation

The first generation devices were irradiated in the PT-2 pneumatic tube system at the High Flux Isotope Reactor (HFIR) at Oak Ridge National Lab (ORNL) in Tennessee. The thermal flux on the date of irradiation was recorded to be 4.58×10^{13} n/cm^2-s with a thermal/epithermal ratio of 4127.9. Figure 25 shows the neutron energy spectrum to which the first generation samples were exposed.

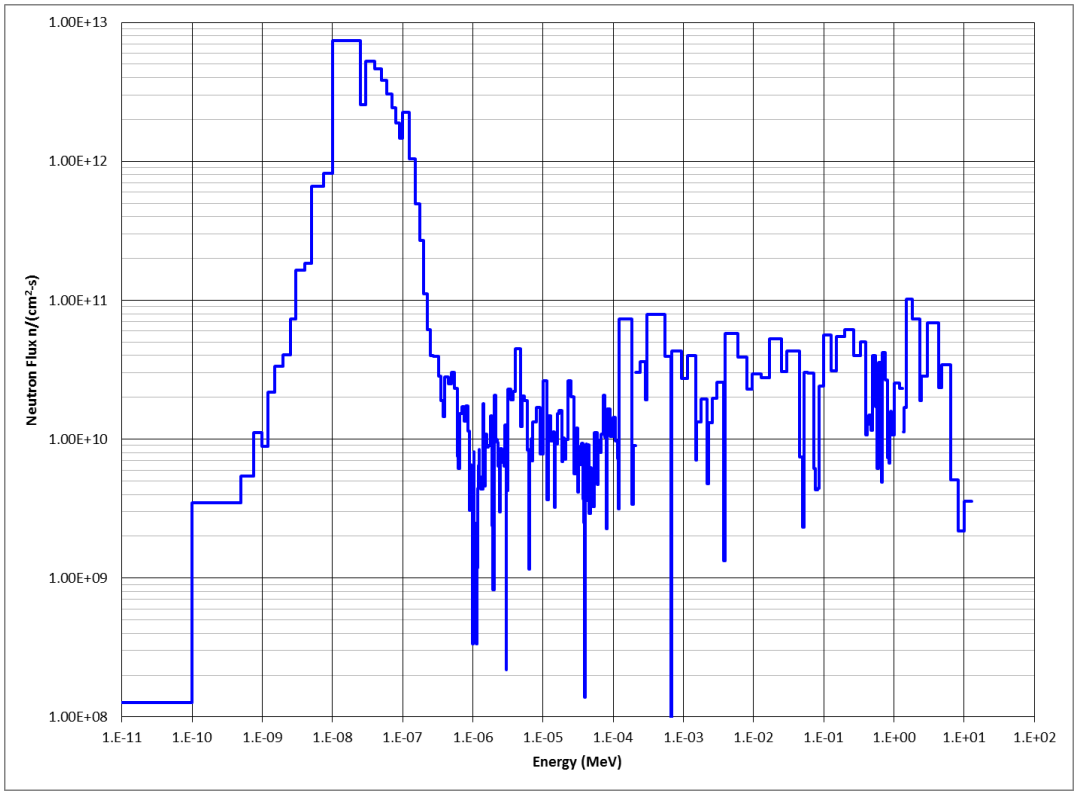

Figure 25: 238-group neutron flux spectrum for PT-2.

The samples were to be subjected to 3 irradiation times: 10 s, 60 s, and 300 s, but the pneumatic tube that transports the rabbits to the reactor burst before any samples could be irradiated for 300 s. Fortunately no one was harmed since all of the potentially radioactive gasses were contained by the fume hood. All of the 10 s and 60 s irradiations had already been done, but some of the samples shattered from the rough handling of the pneumatic system. All of the samples had large enough pieces to perform Raman analysis, albeit not in the exact locations as the pre-irradiation characterizations, but some of the samples were fractured across the electrodes preventing post irradiation electrical resistance measurements. Furthermore, it appears that the fractured pieces may have rubbed up against each other inside the rabbit, removing some nanotubes from the surface. Figure 26 shows the scratched surface of one of the post irradiation samples that fractured.

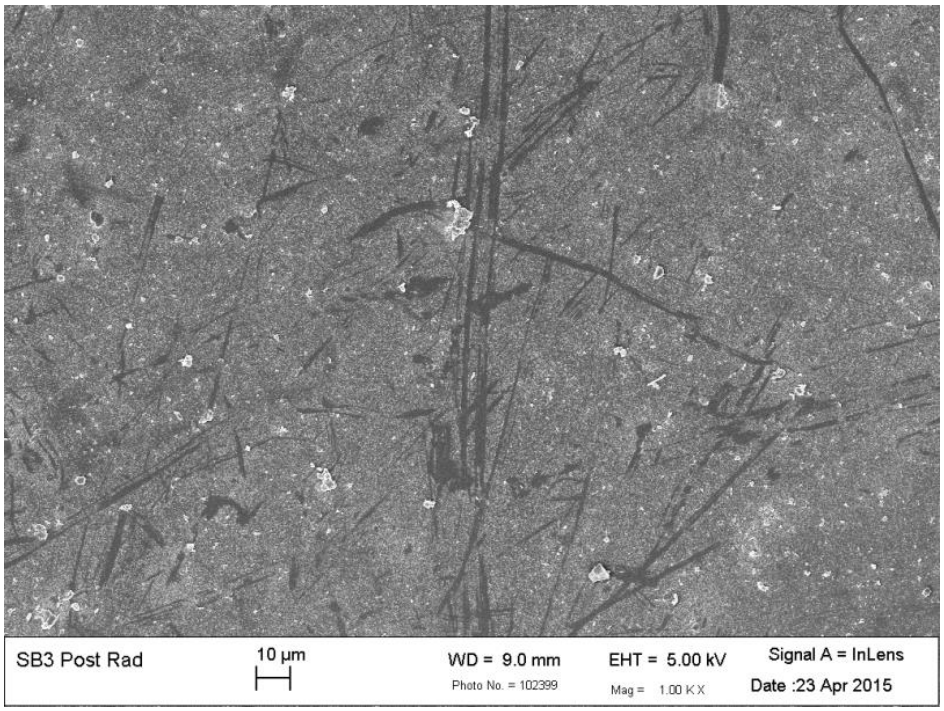

Figure 26: SEM micrograph of the scratched surface of sample that fractured in PT-2.

3.1.3 Electrical Properties

The DC electrical resistance was measured for three devices of different electrode dimensions at each radiation dose. Figure 27 shows how the DC resistance of the MWNT samples were affected by neutron and gamma irradiation in HFIR PT-2. The y-axis represents the percent change in electrical resistance due to irradiation. Each line corresponds to a different set of electrodes (big, medium, and small) on the MWNT sample. The small electrode location on the non-radiated sample was damaged so no electrical data could be collected. A clear trend of increasing resistance with increasing radiation dose is apparent. It is almost exactly linear for the medium electrode and nearly linear for the big electrode. The sensitivity of the device, given by the slope of the line, increases as the size of the electrode decreases. This may be due to the fact that there are fewer alternate conductive paths across the small electrode, so electrons are forced to travel across the less conductive damaged nanotubes rather than detouring around them via undamaged CNTs.

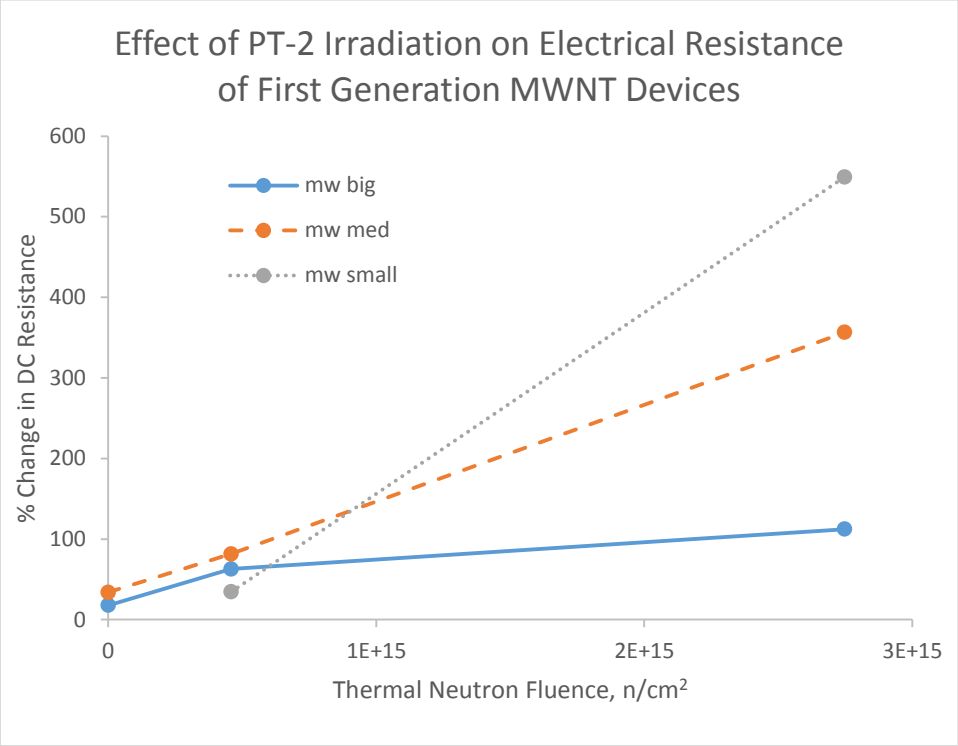

Figure 27: Effect of PT-2 irradiation on the electrical resistance of first generation MWNT samples with big (blue), medium (orange), and small (grey) electrodes.

Figure 28 shows how the electrical resistance of the SWNT samples were affected by neutron and gamma irradiation in HFIR PT-2. The small electrode device on both irradiated SWNT samples was damaged so only the medium and big electrode configurations are shown. It can be seen that the electrical resistance increases significantly then seems to level off at the higher dose.

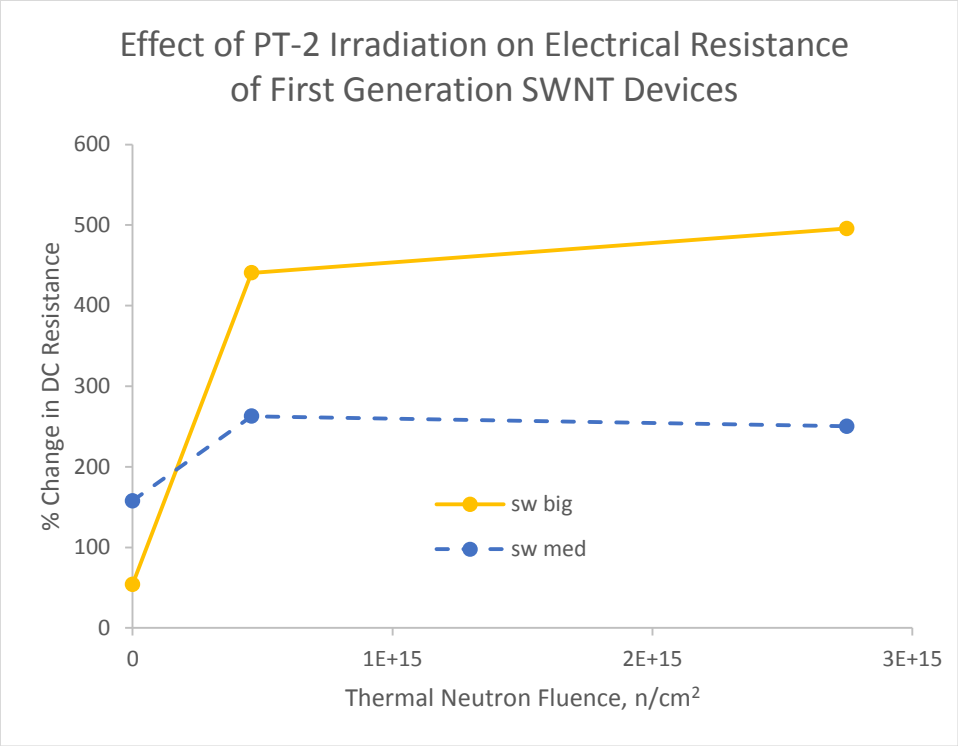

Figure 28: Effect of PT-2 irradiation on the electrical resistance of first generation SWNT samples with big (yellow) and medium (blue) electrodes.

Because these samples are exposed to air, their electrical properties can be influenced by adsorption of molecules such as water and oxygen. Adsorbed molecules would also have an impact on their reaction to irradiation, for example due to radical formation during radiolysis of adsorbed water. They can also be easily damaged if their surface is touched, as the CNTs can be wiped away, as was seen when the samples broke during irradiation and rubbed against each other.

3.1.4 Raman Spectroscopy

Raman spectroscopy has the potential to reveal details about the structural damage incurred by the nanotubes due to exposure to radiation. The primary measure of damage is the ratio of the D peak to the G peak. Since increasing damage to the nanotubes tends to increase the D peak and decrease the G peak, the ratio can give a qualitative measure of the overall concentration of defects in the nanotubes. .

The damage in MWNTs due to irradiation times of 10 and 60 seconds, expressed as a percent change in the D/G ratio from values obtained prior to irradiation, are shown in Figure 29. For these first generation devices, Raman spectra were collected at 784 points for each sample and the 20% highest and lowest values were discarded as a crude method for removing outliers. Data points on the graph represent the mean change in D/G ratio and the vertical bars represent one standard deviation in the positive direction and one in the negative direction.

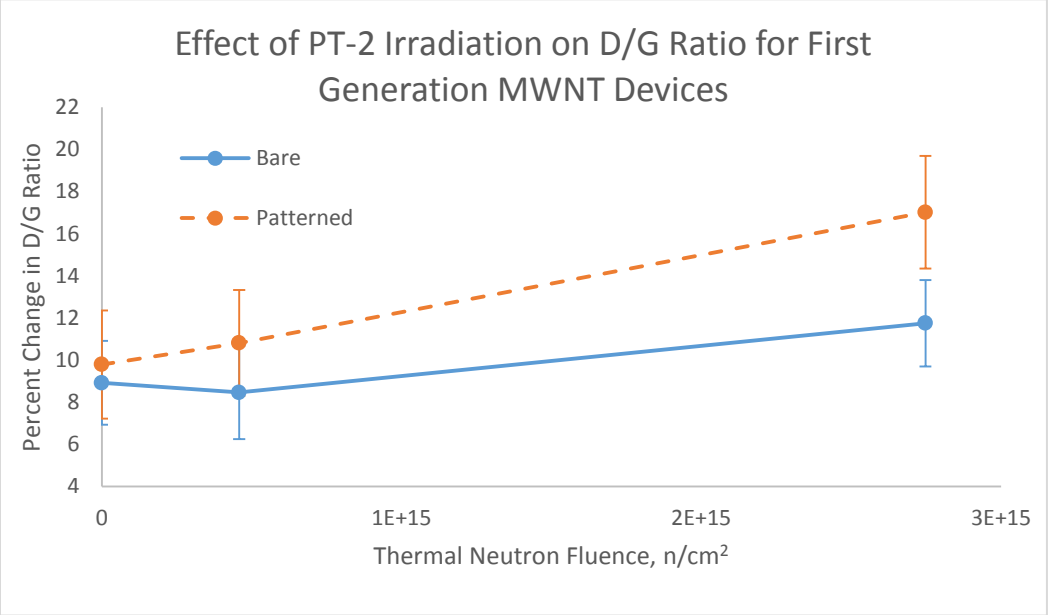

Figure 29: Effect of neutron irradiation on D/G ratio of Raman spectra for MWNT samples. Vertical bars represent standard deviation.

The blue line represents the sample without electrodes while the sample patterned with copper is represented by the orange line. Increasing radiation dose results in an increase in the D/G ratio for both samples. One unexpected feature is that the samples that were not exposed to irradiation showed an 8.9% and 9.8% increase in their D/G ratios, indicating that there was additional damage accumulated

while the devices sat idle. Since the nanotubes in these devices were exposed to air, the influence of humidity, ozone, or some other ambient molecule may have been responsible for this.

The SWNT devices, on the other hand, had very high standard deviations, making any conclusions about their structure difficult to extract from the data. Figure 30 shows the percent change in D/G ratios of the SWNT devices after irradiation.

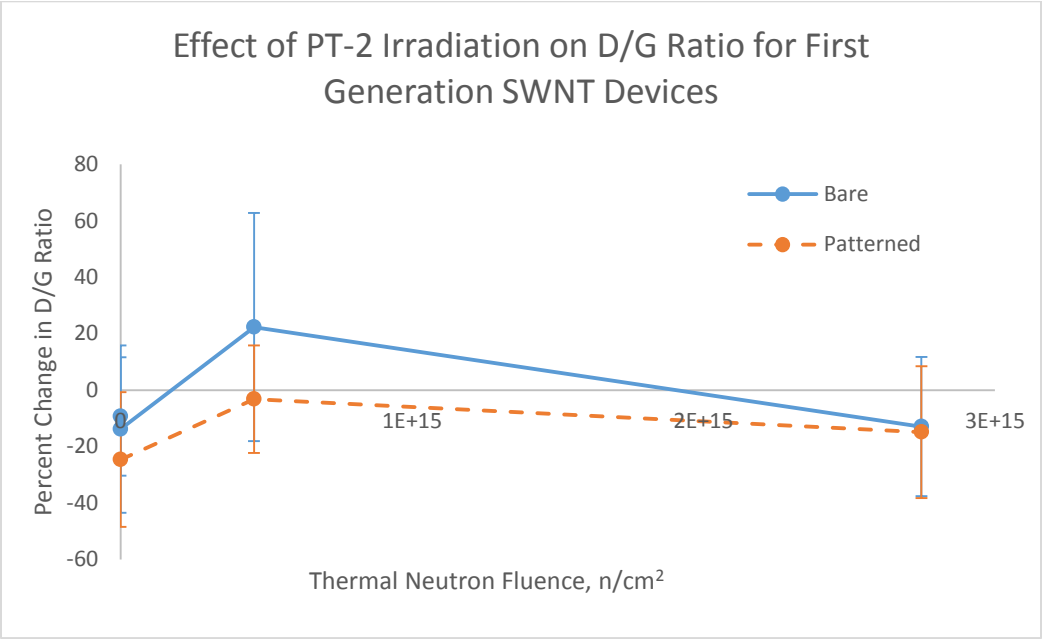

Figure 30: Effect of neutron irradiation on D/G ratio of Raman spectra for SWNT samples. Vertical bars represent standard deviation.

Note that the non-irradiated samples (at 0 s on the x-axis) showed a substantial decrease in the D/G ratio even though they were not exposed to any radiation. These measurements were taken several weeks apart. First the pre-irradiation spectra of all the samples were recorded, then some of the samples were irradiated while the control samples just sat in their container. Once the irradiated samples were released, the spectra of all the samples were collected again. This decrease in D/G ratio suggests a reduction in the defect concentration of the samples after simply sitting in a sealed container

for a few weeks. This could potentially be explained by the fact that the standard deviation of these values was quite high, around 20%-40% of the values themselves, indicating that these variations could just be the result of random variations in the measurement. However, the two samples show very similar trends, suggesting that there is something systematic at work here. Additionally, the general shape of the trend is similar to that of the electrical resistance, with an increase in damage after 10 s matching the increase in electrical resistance at that dose and the subsequent decrease of damage after 60 s potentially explaining the leveling out of the electrical resistance.

The large data scatter of the SWNT devices compared to the low standard deviation of the MWNT samples was due to the differences in amorphous carbon content and network uniformity. The SWNT samples contained large quantities of amorphous carbon, which gives off different Raman signals than CNTs, while the MWNTs had virtually zero amorphous carbon. The other factor that affected the data is that the SWNT network was composed of a wide variety of bundle sizes ranging from individual tubes to large bundles up to 200 nm thick, while the MWNT network was well debundled and uniform.

3.1.5 Conclusions

The most important conclusion drawn from this first generation of devices was that the mechanism of sensing shows promise for dosimetry. This result justified spending additional effort to make more refined devices. The results from the MWNT devices were particularly encouraging, showing a general trend of increasing resistance and defect concentration with increasing radiation dose.

The results also confirmed that all the components of the device were sufficiently pure. Sample purity was a major concern going into this first irradiation and the fact that the devices decayed to undetectable radioactivity levels after just one week proved that the CNT purification process effectively

removed all metallic impurities. Similar irradiations in the past on unpurified CNTs had taken several months to decay.

There were also a number of design decisions motivated by these results. Decreasing electrode dimensions seemed to increase the sensitivity of the devices to neutron and gamma irradiation, so the next generation of devices used even smaller electrodes. The fact that the electrode resistance and D/G ratios changed over time for the non-irradiated control samples suggested that exposure to air could be affecting the results. This motivated an in-depth study of humidity effects. The possibility of interaction with molecules in the air, combined with the ease of accidentally removing nanotubes through inadvertent contact with the surface of the device, motivated the design decision of sealing the CNTs with a layer of silicon dioxide in the next set of devices. SEM micrographs of the SWNT devices revealed that there was a significant amount of amorphous carbon present after purification. This motivated the addition of another step to the purification process for SWNTs to remove as much of this amorphous carbon as possible.

Because the gamma spectrum in PT-2 has not been characterized, it was decided that the next generation of devices would be irradiated in PT-1, another pneumatic tube system in HFIR. PT-1 has higher flux and the gamma spectrum is well defined.

3.2 Second Generation

The second generation devices were similar in concept to the first generation devices in that they relied on a random network of CNTs to detect radiation, but the design and fabrication process were radically different. The first generation devices were designed to be fabricated quickly with immediately available equipment. Now that the concept had been demonstrated to have merit, it was possible to

refine the design by taking advantage of advanced fabrication procedures. It was determined that wafer processing techniques such as those used in the integrated circuit industry could be used to fabricate large numbers of devices with a high degree of precision and uniformity. Additionally, this fabrication method is intrinsically scalable, so that if the devices eventually prove to be effective, they would be easily commercializable.

The goals of the second generation devices were to determine the most effective electrode dimensions and to work through any unexpected issues associated with the new fabrication procedure.

3.2.1 Design and Fabrication

The promising results of the first generation devices justified the time and monetary costs of learning wafer processing techniques. The actual steps in the fabrication of the second generation devices are very similar to those discussed in Chapter 2 for the fabrication of the final fourth generation devices, so only the differences will be discussed in detail in this section.

The second generation devices have a number of significant improvements over the first generation devices. First, a centrifugation step was added to the purification process for the SWNTs in order to remove the amorphous carbon that was observed in the first generation devices. Also, the second generation samples were fabricated on a four inch diameter fused silica wafer, which was cut after batch fabrication, rather than on small rectangular slides that were cut before fabrication. This allowed for the fabrication of a very large number of devices in one process flow, resulting in more uniform characteristics and making this design inherently scalable. This fabrication method also allowed for patterning of smaller and more precise electrodes. Perhaps the most important difference between the

first generation and the second generation is that the CNTs were sealed under a 200 nm thick layer of silicon dioxide in the second generation devices.

Figure 31 shows a schematic and a photo of the second generation devices.

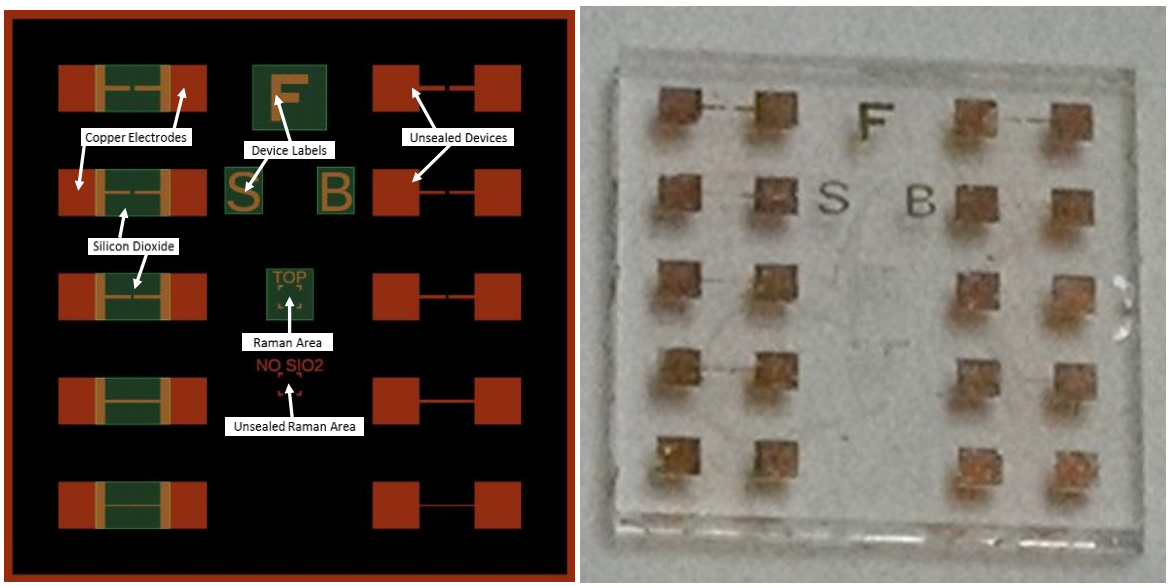

Figure 31: Schematic and photo of second generation device.

This sample has two columns of 5 devices, one column sealed with silicon dioxide and one column unsealed. Each of the 5 devices in each row have different electrode dimensions, as summarized in Table 4.

Table 4: Generation 2 electrode dimensions listed from top to bottom.

Generation 2 Electrode Dimensions		
Device	Width (µm)	Gap Length (µm)
a	50	50
b	30	50
c	30	30
d	30	7
e	7	7

In the center of each device is a designated area for collection of Raman spectra. Raman spectra were collected in a rectangular grid, and four copper marks were patterned into each device to allow this grid to be aligned in order to collect spectra from the same locations before and after irradiation. When designing the layout of these devices, it was unknown whether the silicon dioxide layer would interfere with collection of Raman spectra, so an unsealed Raman area was also patterned into each device. Letters were also patterned in copper onto the devices. The largest letter, an "F", was added to allow for easy visual identification of the front of the sample. Since the substrate is transparent, it was difficult to distinguish between the front and back of the sample, and this large letter that is visible to the naked eye made that task much easier, since it would appear backwards if the sample was upside down. The "S" indicates that this is a SWNT device. MWNT devices were patterned with an "M". The "B" on the right side of the device designated that this side was bare, meaning it had neither CNTs nor silicon dioxide.

Since copper does not adhere well to fused silica, many of the electrodes were damaged during the fabrication process. None of the smallest electrodes survived the lift-off process and only about 25% of the samples had all four of the electrodes intact after fabrication. Fortunately, the wafer processing technique allowed the fabrication of over 100 samples at a time, so 25% was enough to test the design. Obviously, though, this high failure rate would not be acceptable going forward and would need to be addressed in the next design iteration.

3.2.2 Irradiation

Due to the fact that the gamma spectrum was not well characterized for PT-2, it was decided that the second generation devices would be irradiated in PT-1. This would allow exposure of samples to equivalent doses of pure gamma rays in order to distinguish between the effects of gamma and neutron

irradiation. The neutron flux is about an order of magnitude higher than that of PT-2, and the minimum reliable irradiation time possible using the pneumatic tube system is 10 s, so the minimum neutron fluence for the second generation devices was almost as high as the highest neutron fluence for the first generation.

The second generation samples were irradiated for times of 10, 30, 60, 300, and 600 s in PT-1, corresponding to thermal neutron fluences of 4.43×10^{15}, 1.33×10^{16}, 2.66×10^{16}, 1.33×10^{17}, and 2.66×10^{17} n/cm^2, respectively. The radiation environment of PT-1 is discussed in detail in section 2.2.

Like the first generation devices, the second generation devices were irradiated in air, but the significantly higher radiation fluences combined with higher flux caused the copper electrodes to oxidize to the point where they were no longer conductive, as shown in Figure 32.

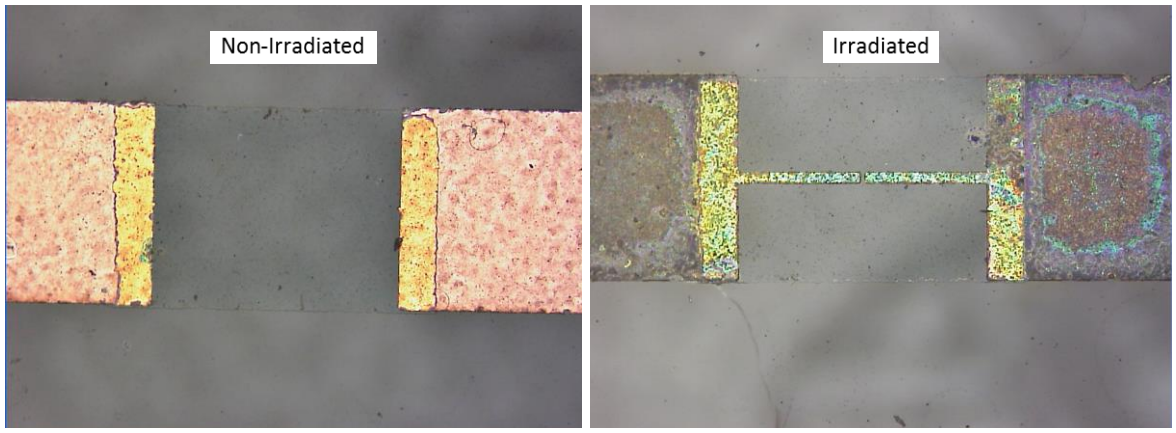

Figure 32: Oxidation of copper electrodes due to irradiation in PT-1.

The discoloration seen in the irradiated sample is characteristic of oxidized copper. The oxidation of the copper was confirmed by electrical measurements, indicating that the electrodes were no longer conductive. Since the silicon dioxide layer extends onto a portion of the electrodes, it was expected that

these portions of the electrode would be protected from oxidation by being sealed from the air, but it is clear from Figure 32 that they were only partially protected and that oxidation did occur even under the silicon dioxide layer. This indicates that the silicon dioxide layer was partially permeable.

3.2.3 Electrical Properties

Since the exposed electrode pads had oxidized and were no longer electrically conductive, it was not possible to measure the post-irradiation electrical properties in the same way that the pre-irradiation properties had been measured. It was hypothesized that only the surface of the electrode pad was oxidized and that, if the thin layer of oxide were removed, there would be conductive copper underneath. To test this theory, an oxidized device was submerged in dilute hydrochloric acid, which etches copper oxide well but does not vigorously attack copper. The acid immediately removed the entire electrode pad, indicating that it had been oxidized all the way through.

Optical microscope images, such as those shown in Figure 32, suggested that the portions of the electrode under the silicon dioxide layer were partially protected from oxidation. Based on this observation, part of the silicon dioxide was scratched off and the exposed portion of less-oxidized electrode were painted with silver paste to form a new electrode pad. This allowed electrical contacts to be established and electrical properties to be measured. These electrical measurements are, of course, not particularly reliable due to the fact that the protected portions of the electrodes were partially oxidized, substantially increasing their electrical resistance. Nonetheless, the electrical properties of these devices were recorded. The change in electrical resistance of the MWNT devices are presented in Figure 33.

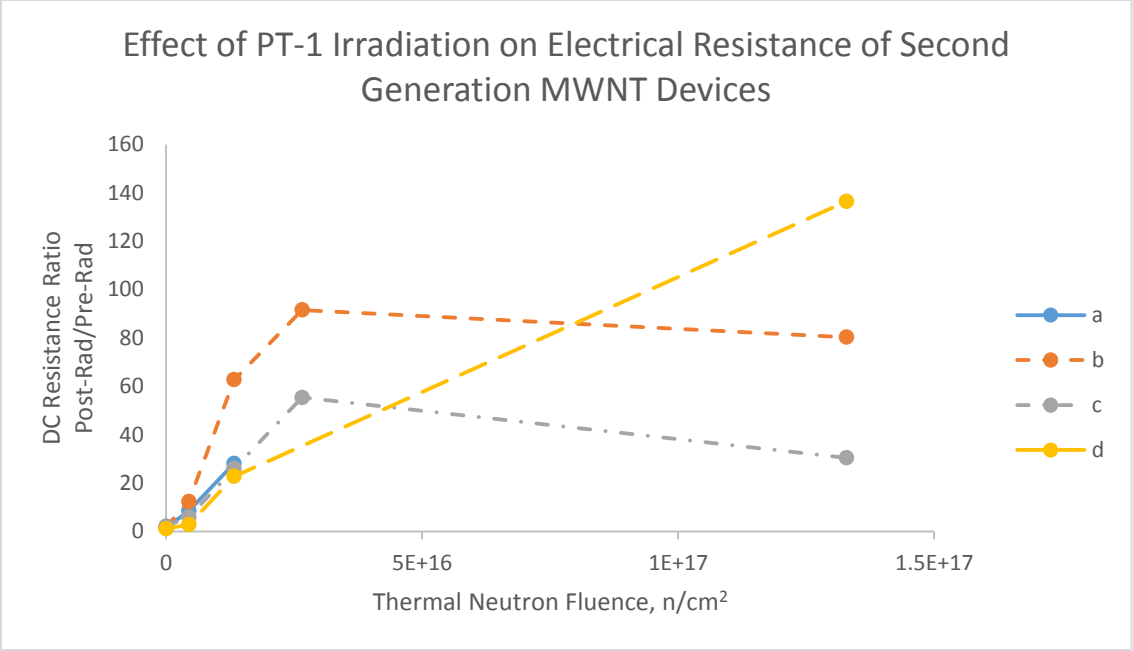

Figure 33: Effect of irradiation in PT-1 on electrical resistance of second generation MWNT devices. Electrode configurations a, b, c, and d correspond to dimensions outlined in Table 4.

The sample exposed to the highest radiation fluence, 2.66×10^{17} n/cm^2, showed no signs of oxidation at all, from which it was concluded that there was something unusual about its irradiation, so this data point was thrown out. The process of rebuilding the electrode pads by hand using silver paste was very delicate and challenging, and three devices were destroyed by accidentally shorting the two electrodes. These devices were configuration a for the 60 s and 300 s samples and configuration d for the 60 s sample. Those devices are not included in Figure 33.

In the first generation devices it was seen that decreasing the width and gap length resulted in an overall increase in sensitivity of the device to radiation. It was hypothesized that this was due to a decrease in alternative conductive paths, which would be caused only by the decrease in width. This hypothesis was further tested in the second generation devices, which support this theory. At the two low doses corresponding with 10 s and 30 s irradiations, the effect of decreasing the electrode width can be seen by comparing configurations a and b, which have the same gap length but different widths. At low

doses, reducing the width from 50 µm to 30 µm increased the sensitivity, as predicted. The effect of reducing the gap length was investigated by comparing configurations b, c, and d, which all have an electrode width of 30 µm but have gap lengths of 50 µm, 30 µm, and 7 µm, respectively. At low doses, reducing the gap length reduces the sensitivity of the device. This result confirms that the increase in sensitivity seen with decreasing electrode dimensions in the first generation devices was due to reductions in the width rather than reductions in the gap length. At high neutron fluences, however, the reduced gap length does not seem to have a consistent effect on the sensitivity. As gap length is decreased, sensitivity first decreases then increases. It is possible that this is because at the highest neutron fluence, the electrodes under the silicon dioxide had oxidized to the point where they were beginning to contribute significantly to the overall resistance.

Figure 34 shows the effect of PT-1 irradiation on the second generation SWNT devices.

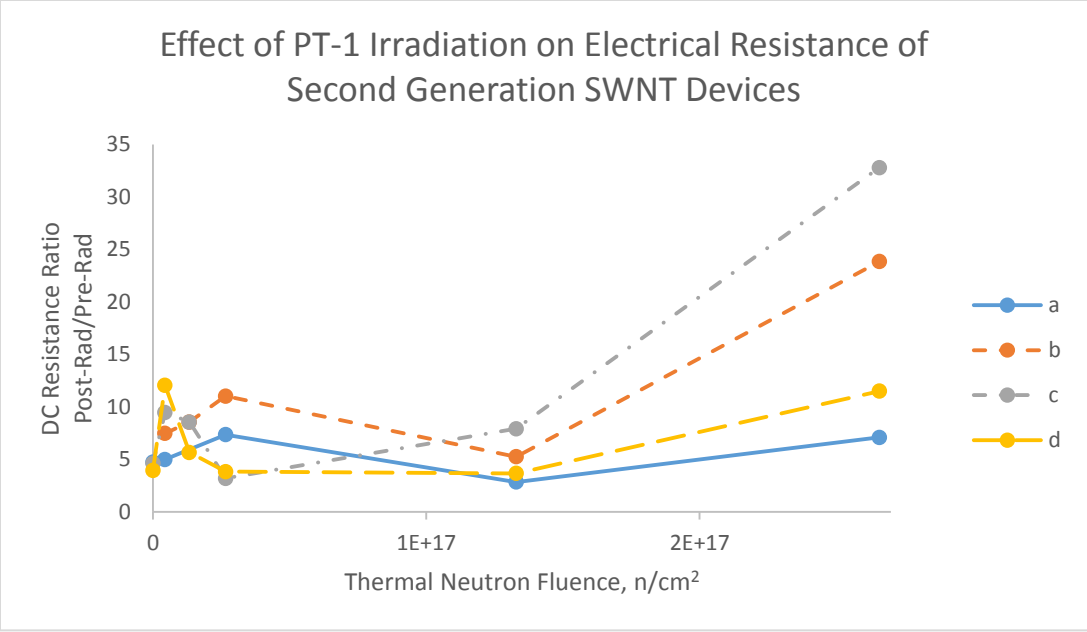

Figure 34: Effect of irradiation in PT-1 on electrical resistance of second generation SWNT devices. Electrode configurations a, b, c, and d correspond to dimensions outlined in Table 4.

The second generation SWNT devices do not show a trend in electrical resistance, with each configuration on different samples giving conflicting results. Increasing radiation dose first increases, then decreases, then increases the electrical resistance, and to quite different extents for each configuration. There is also no trend in the effect of electrode dimensions for the SWNT samples. Each dose results in entirely different sensitivities. Due to the inconsistency of the results, it is not possible to draw any conclusions from the measurements of the electrical properties of the second generation SWNT devices. It is unclear whether this data is the result of a genuine trend in material behavior or if it is caused by variations inherent in the system. To answer this question, multiple devices of each configuration would have to be characterized in order to determine the standard deviation of the dataset.

3.2.4 Raman Spectroscopy

For the second generation devices, Raman spectra were collected at 841 points for each sample with the top and bottom 20% of values thrown out as a crude approach for removing outliers. Figure 35 shows the effect of irradiation on the D/G ratio of the Raman spectra for the second generation MWNT devices. The standard deviation of the Raman data for the second generation devices was much higher than that of the first generation devices. This may be because of the partial permeability of the silicon dioxide layer. Its permeability is the result of pinholes that allow air through in some locations but not others. The effects of irradiation are significantly different in air and in vacuum and the differences in radiation effects at different locations would result in high deviation in the data.

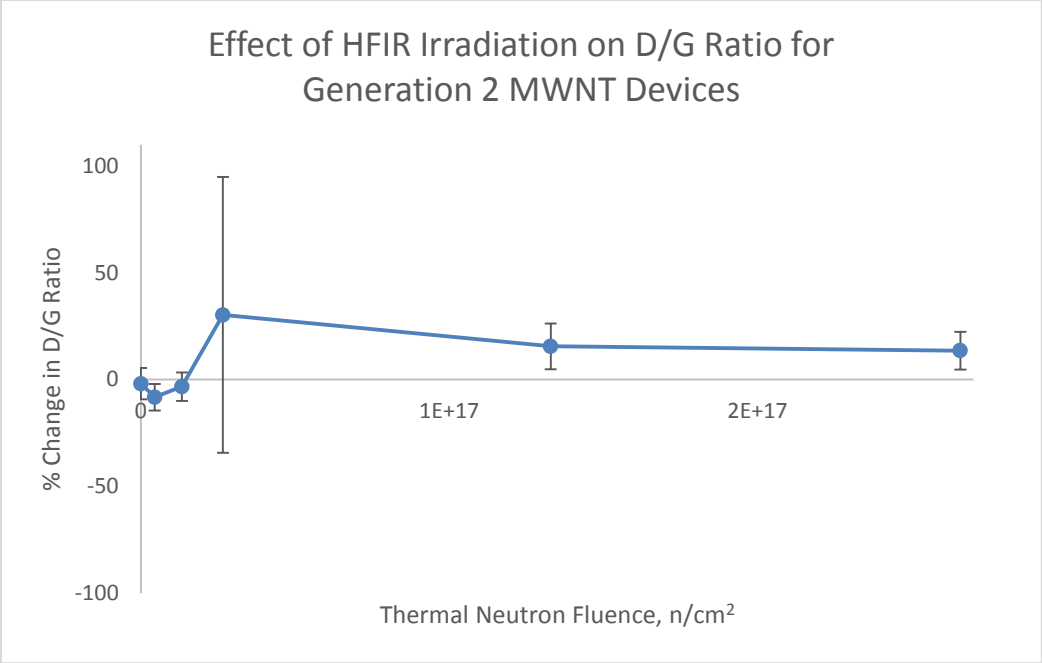

Figure 35: Effect of HFIR irradiation on D/G ratio for second generation MWNT devices. Vertical bars indicate standard deviation.

The data seems to indicate that there is a slight decrease in defect concentration at low radiation dose, but a significant increase in damage at high doses. This initial decrease could be due to annealing of damage already present in the MWNTs from the purification process.

Figure 36 shows the effect of HFIR irradiation on the D/G ratio of the Raman spectra for the second generation SWNT devices. It is clear that the standard deviation of the data is far too high to draw any meaningful conclusions.

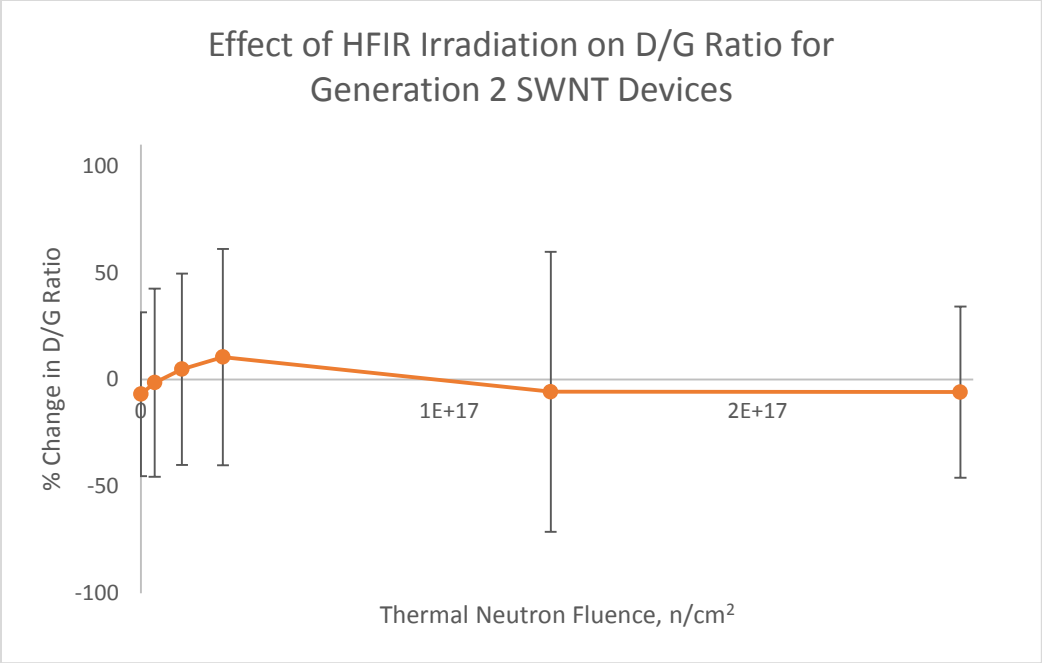

Figure 36: Effect of HFIR irradiation on D/G ratio for second generation SWNT devices. Vertical bars indicate standard deviation.

3.2.5 Conclusions

The second generation experiments prompted a number of critical design changes. The most significant issue that needed to be addressed was the oxidation of the electrodes, which cast doubt on all of the electrical property measurements. Another issue with the electrodes that was uncovered was that the poor adhesion of copper on the fused silica substrate results in the destruction of far too many devices when the electrode dimensions are small. The partial oxidation of the electrodes under the silicon dioxide layer demonstrated that the silicon dioxide layer was somewhat permeable to air. It was concluded that this was due to pinholes that extended through the thickness of the silicon dioxide layer. The inconsistent changes in resistance of the SWNT devices brought up the question of whether a real trend was being observed or whether it was simply data scatter. The inability to answer this question motivated the design decision to include enough devices on each sample to perform statistical analysis. These considerations were addressed in the third generation of devices.

3.3 Third Generation

The third generation devices represented a refinement of the design based on the experience gained from the second generation. The second generation was the first generation that used wafer processing fabrication techniques and it was the first time samples were irradiated in PT-1. The third generation devices were fabricated using the same techniques as the second generation devices, and the lessons learned were applied to the new design.

3.3.1 Design and Fabrication

The most significant changes to the design in the third generation were to the layout and to the electrode materials. The layout of the devices was finalized during this redesign, with 8 devices per sample, each with electrode width and gap length of 50 µm, as shown in Figure 37. This design allowed for statistical analysis of electrical property measurements.

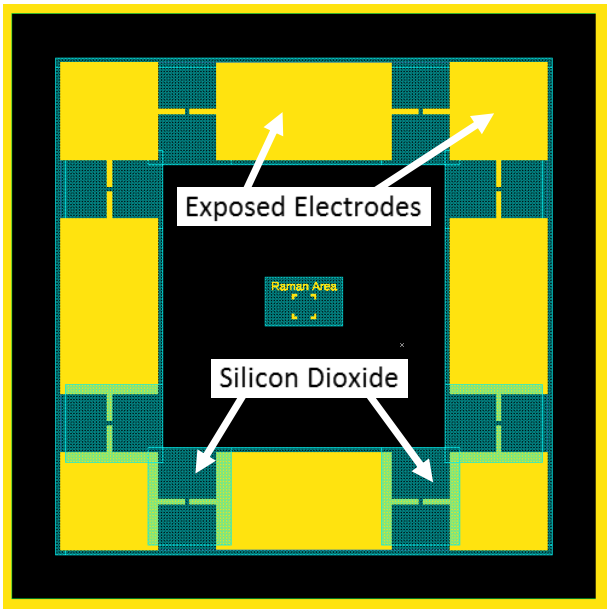

Figure 37: Layout of third generation devices.

To address the oxidation problem, it was decided that the electrodes would be made from nickel instead of copper. Nickel is significantly more resistant to oxidation than copper, but it has the drawback of less desirable radioactivation properties. Nickel interacts with high energy neutrons through an (n,p) interaction to become cobalt-58, which has a half-life of 70.86 days, so if enough of this isotope is produced during irradiation it would take a very long time to decay to releasable levels. With this in mind, a layer of nickel only 5 nm thick was used. Since, like copper, nickel also does not adhere well to the fused silica substrate, an adhesion layer was used. Titanium was chosen as the adhesion layer because it adheres very well to both fused silica and to nickel and because it does not activate strongly when irradiated with neutrons. Titanium, however, oxidizes quite readily, which is why it was necessary to coat the titanium with a layer of nickel.

Because the silicon dioxide layer of the second generation devices was partially permeable to air due to pinholes, a much thicker layer was deposited on the third generation devices. The silicon dioxide layer was 200 nm thick in the second generation and 2000 nm thick in the third generation. This ensured that pinholes could not penetrate through the entire layer.

In order to begin exploring the potential to tune the sensitivity of the devices to neutron radiation, some samples were also made with a thin boron layer.

3.3.2 Irradiation

To further protect the devices from oxidation, they were irradiated in a helium environment. Since there are no flow gasses in PT-1, this was accomplished by packing the rabbits with helium before irradiation. Helium was chosen over argon because argon activates strongly under neutron irradiation

and radioactive gasses are a serious health and safety concern. To pack the rabbits with helium the samples and rabbits were placed inside a glove bag that was connected to a helium tank. The helium was continuously flowed through the glove bag while the samples were placed into the rabbits and the screw tops closed to seal the gas in the rabbit. Samples were then irradiated for 10 s, 30 s, 60 s, 120 s, and 300 s.

Despite the measures taken to prevent oxidation, some of the electrodes still oxidized, as shown in Figure 38.

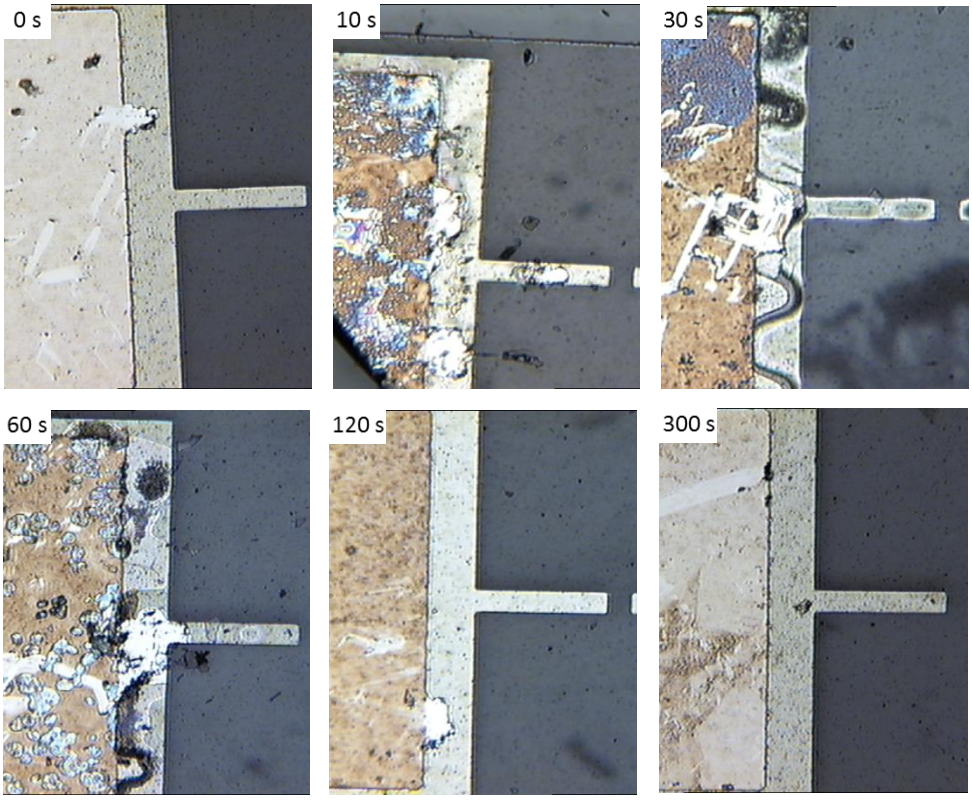

Figure 38: Oxidation of some electrodes after irradiation of third generation MWNT devices. Irradiation time for each device is labelled.

The exposed portions of the electrodes of the 10 s, 30 s, and 60 s samples all oxidized to the point where they were no longer conductive while the electrodes of the devices that were irradiated for the longest

duration did not oxidize and remained conductive. The fact that any of the electrodes oxidized indicates that the nickel layer was not thick enough to prevent oxygen from reaching the titanium adhesion layer. The fact that some of the samples underwent oxidation while others did not leads to the conclusion that the packing with helium was not consistent, and some rabbits either were not sealed tightly enough or were not filled entirely with helium when they were sealed. By chipping away the silicon dioxide layer that was covering the electrodes it was possible to determine that the sealed portions of the electrodes did not undergo significant oxidation, confirming that the thicker silicon dioxide layer was a much better barrier to oxygen. For the SWNT devices, only the samples irradiated for 30 s and 300 s were free from oxidation.

The samples with the boron conversion layer were all destroyed during irradiation by liftoff of the silicon dioxide layer as shown in Figure 39. This is the result of both the poorer adhesive properties of boron and the additional damage and heat generated by conversion of neutrons into alpha particles.

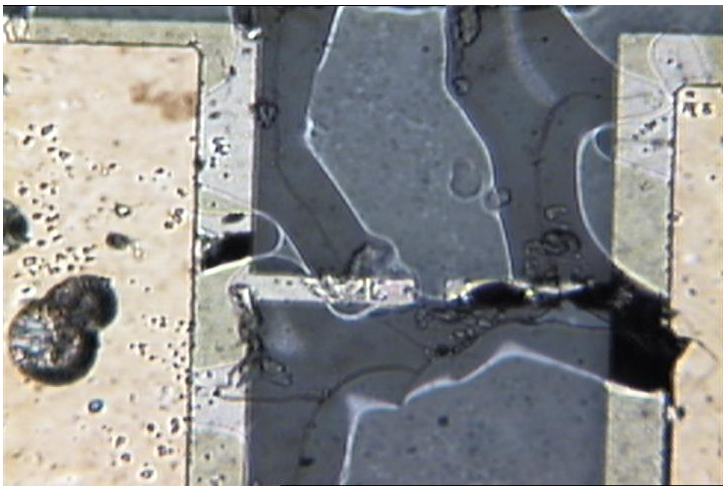

Figure 39: Liftoff of silicon dioxide layer in device with boron conversion layer.

3.3.3 Electrical Properties

Since the electrodes of many of the samples oxidized, the data points for evaluation of the effects of irradiation on the electrical properties of the device are limited. Figure 40 shows the effect of irradiation on the electrical resistance of the MWNT devices that were not oxidized. Each data point represents the mean change in electrical resistance of the 8 devices. Vertical bars represent one standard deviation in the positive direction and one in the negative direction.

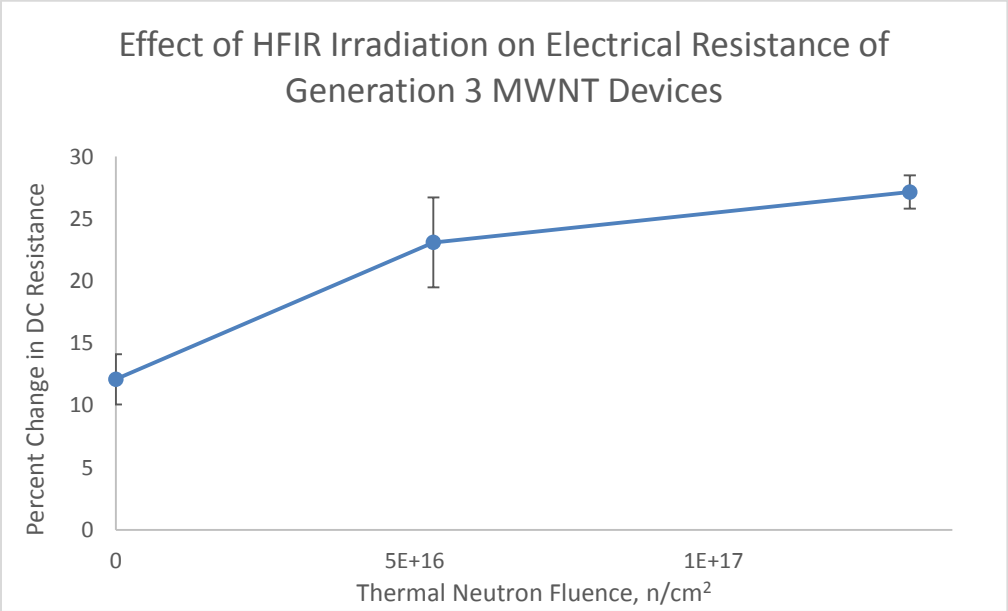

Figure 40: Effect of HFIR irradiation on the DC electrical resistance of third generation MWNT dosimeters. Vertical bars indicate standard deviation.

Consistent with previous results, there was a trend of increasing resistance with increasing radiation dose for the MWNT devices. Both the total change in resistance and the standard deviation of the values were much lower when irradiated in helium than when irradiated in air, indicating that oxidation and radical formation played a significant role in damaging the CNTs in the previous experiments.

Figure 41 shows the effect of irradiation on the electrical resistance of the SWNT devices that were not oxidized.

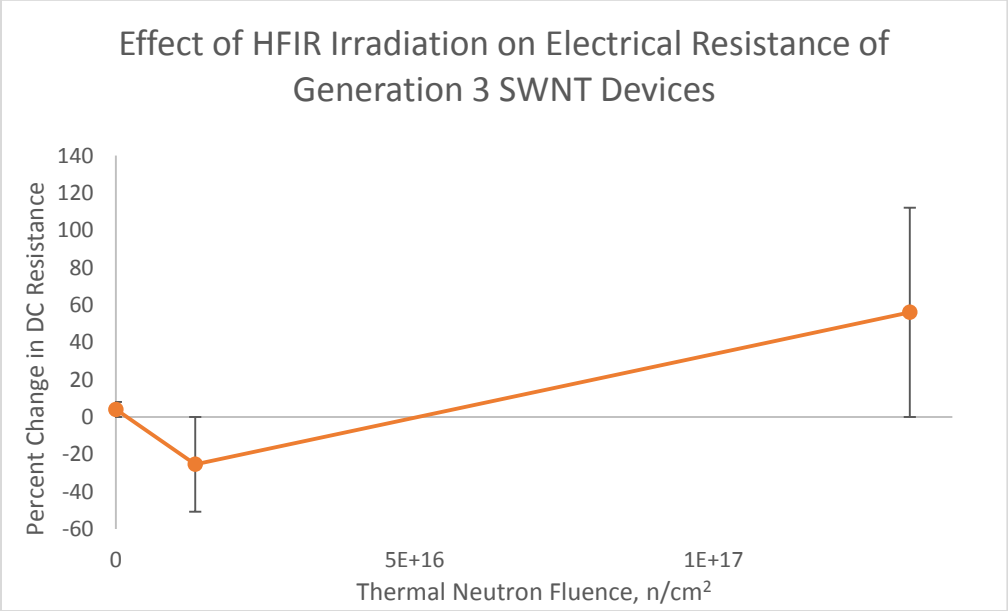

Figure 41: Effect of HFIR irradiation on the DC electrical resistance of third generation SWNT dosimeters. Vertical bars indicate standard deviation.

The resistance first decreased then increased as radiation dose increased. The standard deviation of this dataset is fairly high though and more data points would be necessary to reliably establish a trend.

3.3.4 Conclusions

The fact that the electrodes oxidized demonstrated that the 5 nm nickel layer was not thick enough to prevent oxygen from reaching the titanium adhesion layer. Since the samples decayed to releasable radiation levels within a week, it was concluded that the thickness could be increased substantially without risking serious delays. The titanium adhesion layer worked very well in terms of preventing damage to the electrodes during fabrication and characterization. No electrodes were damaged by being scratched off as they were in the second generation devices.

Since some samples oxidized while others did not, it was clear that there were procedural issues with the helium packing. Either the glove bag was not fully purged of oxygen, the rabbits had some oxygen trapped in them, or the rabbits were not adequately sealed and oxygen leaked in. In the fourth generation, the purge time was increased, the helium was flowed directly into the rabbits for several seconds to make sure all oxygen was removed, and the twist caps of the rabbits were tightened very tight using an Allen wrench.

The final design used the same layout as the third generation devices, with the only design change being that the titanium layer thickness was decreased and the nickel layer thickness was increased.

4. Results and Discussion

4.1 DC Electrical Resistance

At each fluence level, the DC electrical resistance of eight devices was recorded before and after irradiation. The change in resistance due to irradiation was then calculated as a percentage of original resistance for each of the devices and plotted as a function of fluence. Changes due to external factors such as equipment calibration and ambient temperature were accounted for by subtracting out the small changes measured in a non-irradiated control sample. The same process was carried out for both SWNT and MWNT devices, with significantly different results.

4.1.1 SWNT Devices

Figure 42 shows the effect of mixed neutron and gamma irradiation from HFIR on the SWNT devices. Data points represent the mean change in resistance of the eight devices on each sample and the vertical bars represent one standard deviation in both the positive and negative direction.

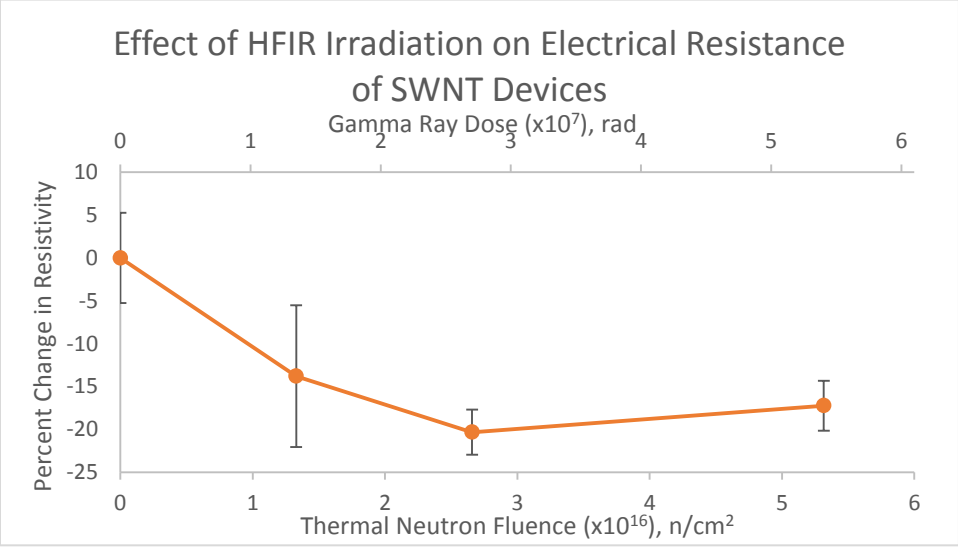

Figure 42: Effect of HFIR irradiation on the DC electrical resistance of SWNT dosimeters. Vertical bars indicate standard deviation.

Notice that the resistance initially decreases with increasing neutron radiation fluence then levels out or even begins to increase after 2.658×10^{16} n/cm^2. The non-linearity of this trend indicates that the cause of the initial decrease in resistance tends to fade as fluence increases. The fact that the slope of the trend inverts suggests that there are competing effects at work in this device.

Trends of this nature have been reported in the literature when irradiating SWNT paper with argon and nitrogen ions [93]. Low fluences of ions, up to 2×10^{12} ions/cm^2, increased the conductivity of the SWNT paper while higher fluences decreased conductivity. This initial increase in conductivity was explained by thermal annealing of defects and impurities present in the pristine SWNT paper. When energy is transferred to a nanotube in the form of heat, that heat is easily conducted through the defect-free portions of the nanotube but builds up rapidly when it encounters a barrier to heat transfer. These local high energy points can anneal defects such as vacancies, by allowing them to migrate, and dopants, by desorbing impurities. Naturally, once defects are annealed and dopants desorbed, thermal annealing can no longer reduce the resistance of the SWNT network, and the effects fall off. As radiation damage accumulates, the resistance begins to increase again. Since this annealing would continue to compete with defect formation caused by irradiation, it is possible that damage accumulation is affected by dose rate. Not all defects can be annealed, so it is expected that defect concentration would increase with increasing dose in the long term until the nanotubes are destroyed.

Another possible mechanism for the decrease in resistance is the formation of cross-links between separate SWNTs in a bundle, reducing the inter-tube resistance. The formation of cross-links between adjacent nanotubes in a SWNT rope under exposure to various types of irradiation including ions, electrons, and gamma rays is well documented in the literature [40, 47, 94-97].

Figure 43 shows the effect of pure gamma irradiation on the SWNT devices. The gamma ray doses were chosen to match the gamma exposure of the HFIR samples.

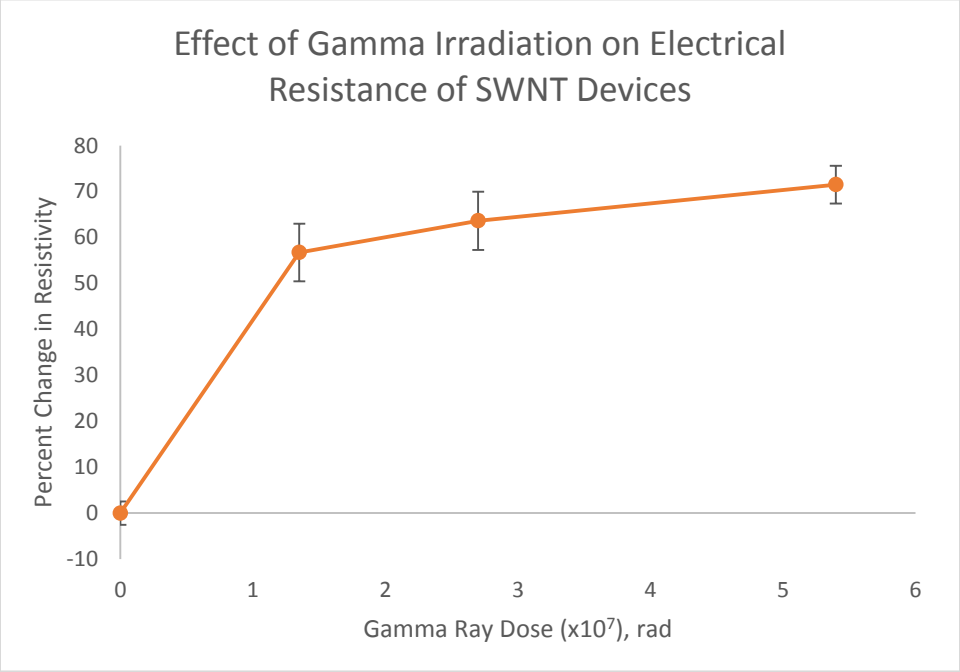

Figure 43: Effect of gamma irradiation on the DC electrical resistance of SWNT dosimeters. Vertical bars indicate standard deviation.

This trend is very different from that of the mixed radiation environment of HFIR, with pure gamma rays causing an increase in resistance of the devices. The stark differences in these two trends indicate that neutron and gamma irradiation result in competing effects on the SWNT devices. It is also clear that at these relative dose rates, the effects of neutron radiation dominate. The logarithmic shape of this trend strongly suggests saturation of defects. These defects can be caused by direct energy transfer to the atoms in the lattice, breaking bonds to cause vacancies, or by the formation of radicals via radiolysis of water molecules adsorbed on the SWNTs.

One possible explanation for the lack of an initial decrease in resistance in the pure gamma ray environment is a lack of annealing. The dose rate and overall energy in the gamma irradiation facility are substantially lower than that of HFIR, which results in lower overall temperatures, which may be too low to desorb dopants or allow annealing of other defects. It is also possible that cross-linking is less prevalent in the pure gamma ray environment. This is because cross-linking relies on the formation of two adjacent vacancies within a short time. At lower dose rates it is less likely that a second vacancy is formed nearby before the first vacancy has been rearranged to saturate its dangling bonds.

The effects of gamma and neutron irradiation on randomly oriented networks of SWNTs is complex, with the two types of radiation interacting with the nanotubes in ways that result in very different modifications to the electrical properties of the devices. This finding is very significant from a scientific perspective but not very useful from an engineering perspective, since this type of complex response to irradiation does not lend itself to accurate dosimetry. An ideal neutron radiation dosimeter for RPV lifetime assessment would show a linear trend in resistance with increasing dose over the relevant range, while showing little or no response to pure gamma rays. This is precisely the response that is observed in the case of the MWNT devices.

4.1.2 MWNT Devices

Figure 44 shows the effect of mixed neutron and gamma irradiation from HFIR on the MWNT devices.

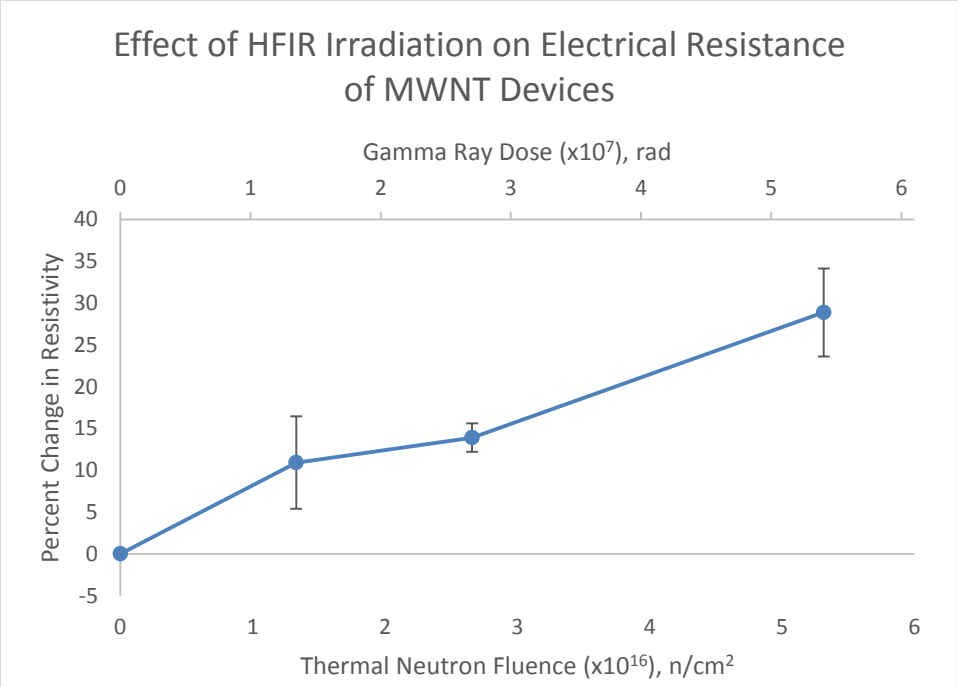

Figure 44: Effect of HFIR irradiation on the DC electrical resistance of MWNT dosimeters. Vertical bars indicate standard deviation.

The resistance increases linearly with increasing radiation fluence with relatively low standard deviation. The response of the MWNT devices is quite different from that of the SWNT devices, showing no reduction in resistance and with a linear trend rather than logarithmic.

Figure 45 shows the effect of pure gamma irradiation on the MWNT devices. The gamma ray doses were chosen to match the gamma exposure of the HFIR samples.

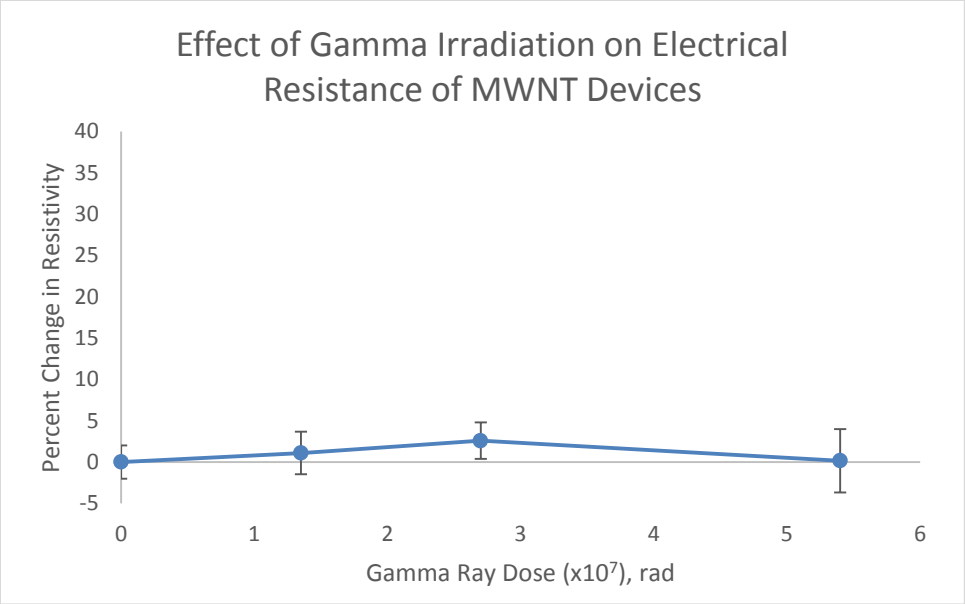

Figure 45: Effect of gamma irradiation on the DC electrical resistance of MWNT dosimeters. Vertical bars indicate standard deviation.

The MWNTs are very robust to gamma irradiation, showing practically no measureable change in resistance even at the highest dose. This is in line with other results that also found MWNTs to be less sensitive to gamma rays than SWNTs [53].

To understand why irradiation affected the MWNT devices in such a different way than the SWNT devices it is helpful to recall some of the differences between them. First, the SWNT devices are made up of a combination of semiconducting and metallic nanotubes while the MWNT devices are made up of entirely metallic nanotubes. This means that doping can substantially decrease the resistance of the SWNT devices but not the MWNT devices. There are also significant morphological differences between the SWNT and MWNT devices, as shown in Figure 46.

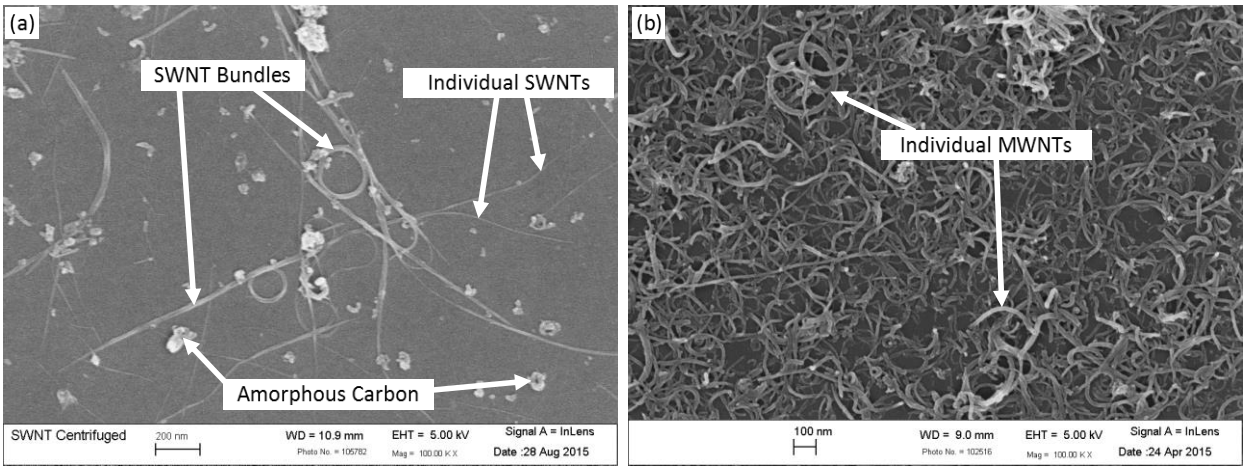

Figure 46: Morphological differences between SWNT and MWNT devices.

The SWNTs are highly agglomerated into bundles while the MWNTs are arranged in a more uniform mat with individual nanotubes intersecting at angles. This means that the MWNTs are only in contact with each other at individual points whereas each SWNT is in contact with several other SWNTs along its entire length. This morphological difference could result in more favorable conditions for formation of crosslinks between SWNTs than MWNTs, which could account for the difference in HFIR radiation effects.

4.3 Raman Spectroscopy

At each dose, Raman spectra were recorded at 49 points before and after irradiation. The changes in a number of spectral features were analyzed in order to gain insights into the effects of irradiation on the microstructure of the nanotubes.

4.3.1 D/G Ratio

The D peak increases with increasing defect concentration while the G peak is not strongly affected by defects. Therefore, the ratio of the intensity of the D peak to the G peak is a good qualitative indicator

of the general defect concentration. Increasing D/G ratio indicates increasing defect concentration. Figure 47 shows the effect of mixed neutron and gamma irradiation in HFIR on the D/G ratio of the MWNT devices. Each data point represents the mean of the change in D/G ratio of the 49 points and the vertical bars represent one standard deviation in the positive direction and one in the negative direction.

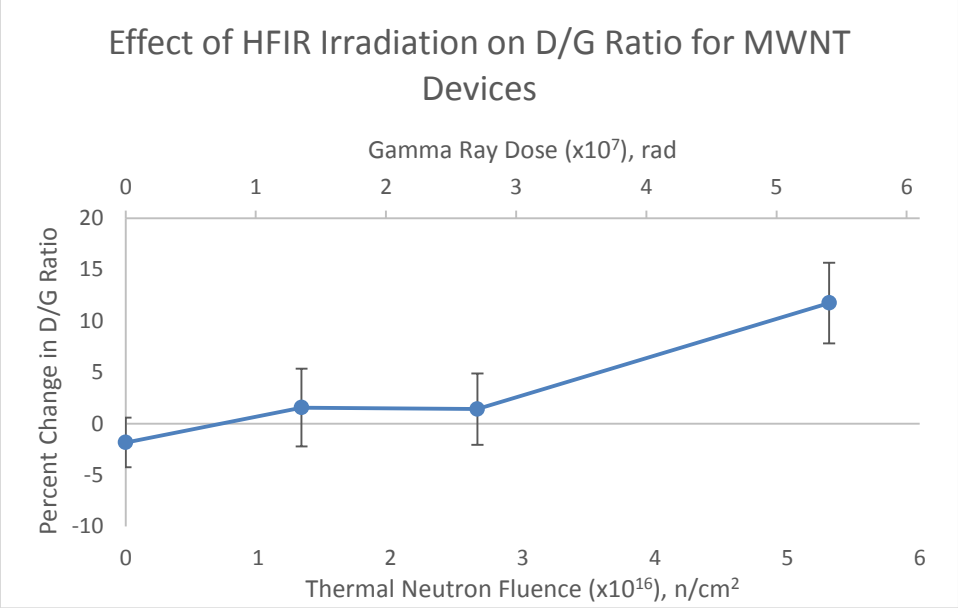

Figure 47: Effect of HFIR irradiation on D/G ratio for MWNT devices. Vertical bars indicate standard deviation.

This trend line is very similar to that of the DC electrical resistance for MWNTs, which confirms the hypothesis that increasing defect concentration is the dominant mechanism driving the increasing resistance. Because these spectra are collected from a network of nanotubes, there are contributions from MWNTs of different sizes, chiralities, number of walls, and orientations, there are naturally some differences even between consecutive measurements. Despite this, the trend of increasing D/G ratio is quite apparent for the case of MWNTs.

The Raman spectra of the MWNT devices before and after irradiation in the pure gamma ray environment of GIF is shown in Figure 48.

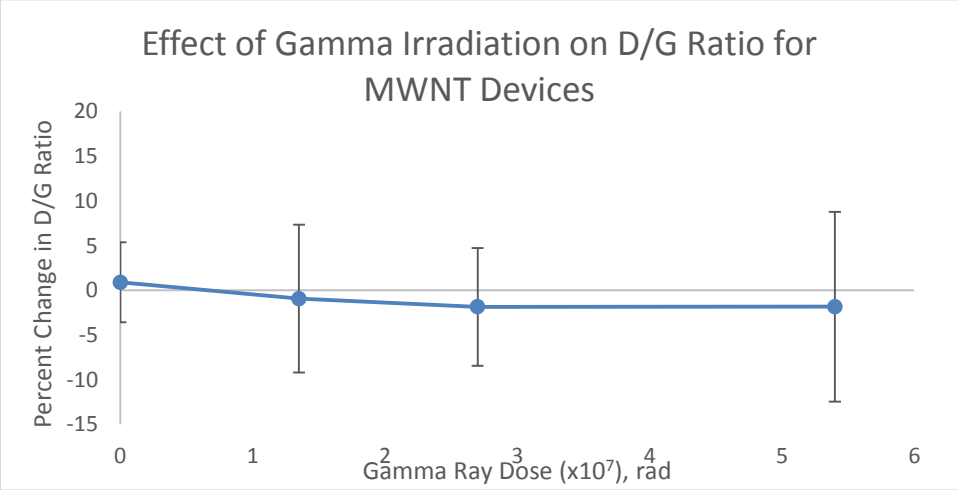

Figure 48: Effect of pure gamma rays on D/G ratio for MWNT devices. Vertical bars indicate standard deviation.

This demonstrates that the MWNTs are very robust to gamma rays, showing no measurable change in defect concentration with increasing dose. Even the highest dose results in a change that is within a fraction of one standard deviation.

The fact that the changes in electrical resistance are driven by an increase in defect concentration, combined with the selective sensitivity to neutrons, makes these devices ideal for neutron dosimetry in nuclear reactor pressure vessels.

Raman spectroscopy of the SWNT devices was not as informative as that of the MWNT devices due to morphological differences. The MWNT network is very homogeneous, with every location made up of a

uniform layer of individual MWNTs. The SWNT network, on the other hand, is highly non-uniform, with some areas containing a bundle of hundreds of SWNTs, some areas with just a few individual nanotubes, and some areas with no nanotubes at all. Since the Raman spectrum of a bundle of nanotubes is different from that of an individual CNT, the data collected from the SWNT devices is very dependent on location. The spectra collected at different locations in the SWNT devices often have very different shapes. For this reason, the standard deviation of the SWNT data is much higher than that of the MWNT devices, which makes it an insensitive characterization technique.

In the MWNT devices, neutron irradiation resulted in a change in D/G ratio on the order of 10%, so it is reasonable to expect a result of around that magnitude for the SWNT devices. However, as shown in Figure 49, these types of changes were not detectable because the standard deviation of the dataset was several times larger than the expected changes resulting from irradiation.

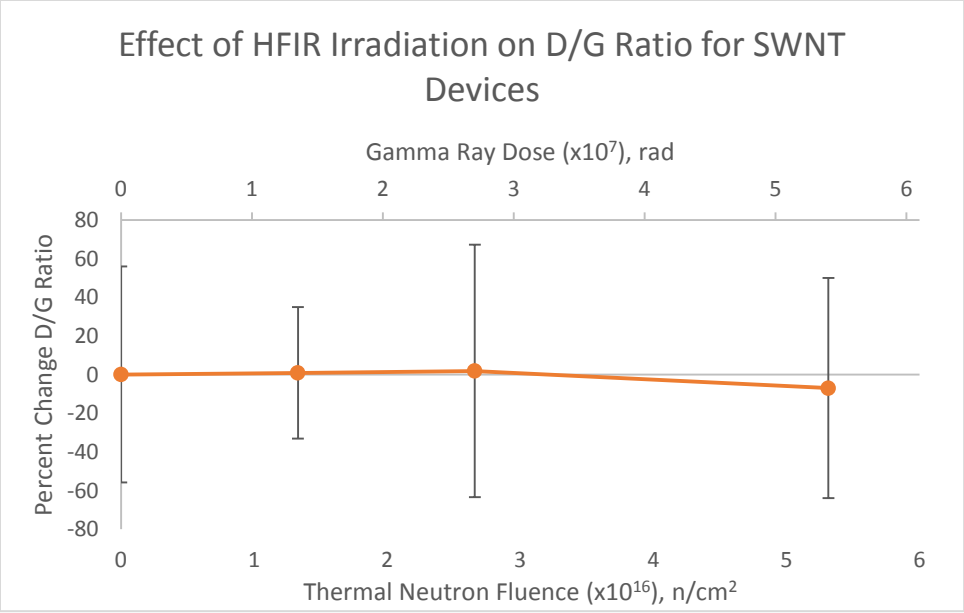

Figure 49: Effect of HFIR irradiation on D/G ratio for SWNT devices. Vertical bars indicate standard deviation.

The high scatter among SWNT devices is present in every feature of the Raman spectrum, making Raman spectroscopy of the SWNT networks less informative than that of the MWNT networks. The scatter of the data also makes it difficult to draw conclusions about the effect of pure gamma irradiation on the defect concentration in the SWNT devices, as shown in Figure 50. One of the 49 data points was removed from the dataset for the sample irradiated at a gamma ray dose of 2.7×10^7 rad due to the fact that it was clearly not the Raman spectrum of a CNT.

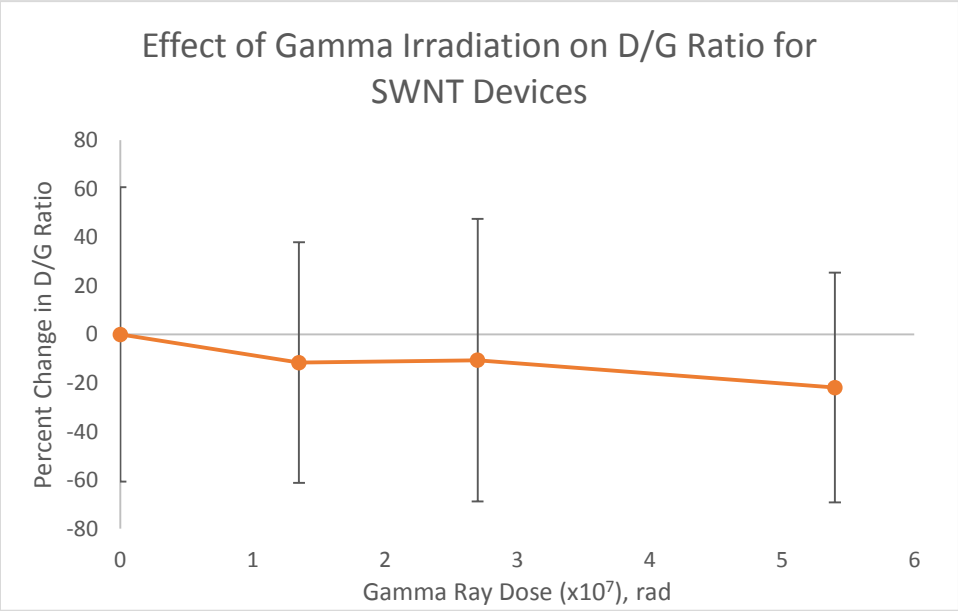

Figure 50: Effect of gamma irradiation on D/G ratio for SWNT devices. Vertical bars indicate standard deviation.

There is a downward trend with increasing radiation dose, which would indicate a decrease in defect concentration, but the largest change is less than half of the standard deviation, so it is not conclusive.

4.3.2 D Peak Position

Shifts in the position of the D peak are useful for differentiating between increases in defect concentration due to sample doping and damage to the microstructure. Damage to the lattice from knock-on impacts does not influence the position of the D peak, and any shifts would indicate sample doping. Doping by p-type dopants causes an upshift in the position of the D peak while doping by n-type dopants causes a downshift in the D peak position. Figure 51 shows the effects of HFIR irradiation on the position of the D peak for the MWNT devices.

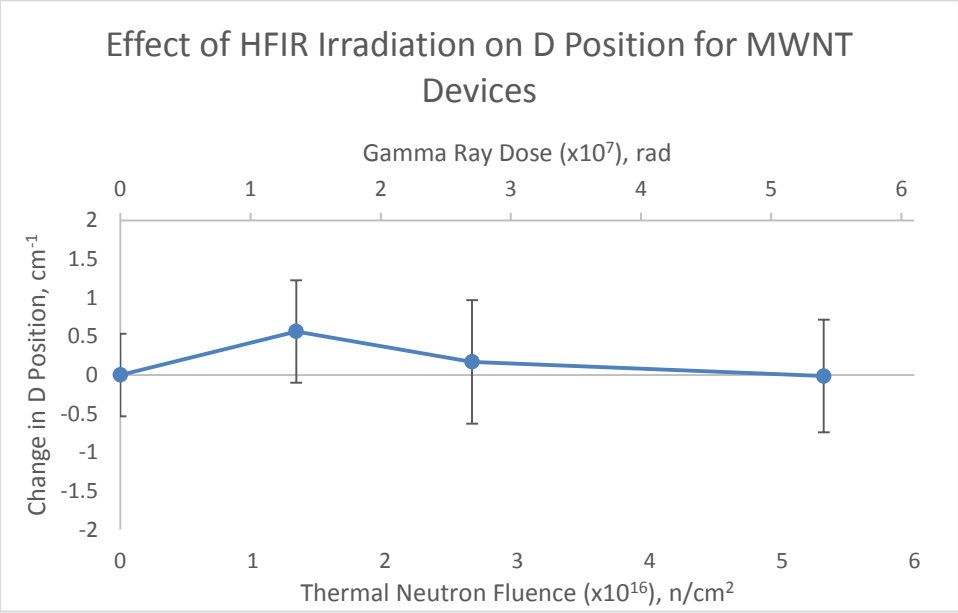

Figure 51: Effect of HFIR irradiation on D peak position for MWNT devices. Vertical bars indicate standard deviation.

This result shows very little, if any shift in the position of the D peak, indicating that there is not significant sample doping. The lowest neutron fluence shows a slight upshift in the position of about 0.5 cm^{-1}, which is within one standard deviation of zero change. Considering that at higher fluences, the change is even less, it is apparent that sample doping does not play a major role here. Figure 52 shows

the effect of gamma irradiation on the D peak position. This data shows a similar trend with indication of slight doping at low radiation doses and zero doping at the highest dose. In the Raman spectra of the gamma irradiated sample, the low dose downshift in D peak position is above a standard deviation, indicating that there probably is some doping occurring at these low doses but that it disappears with increasing radiation dose.

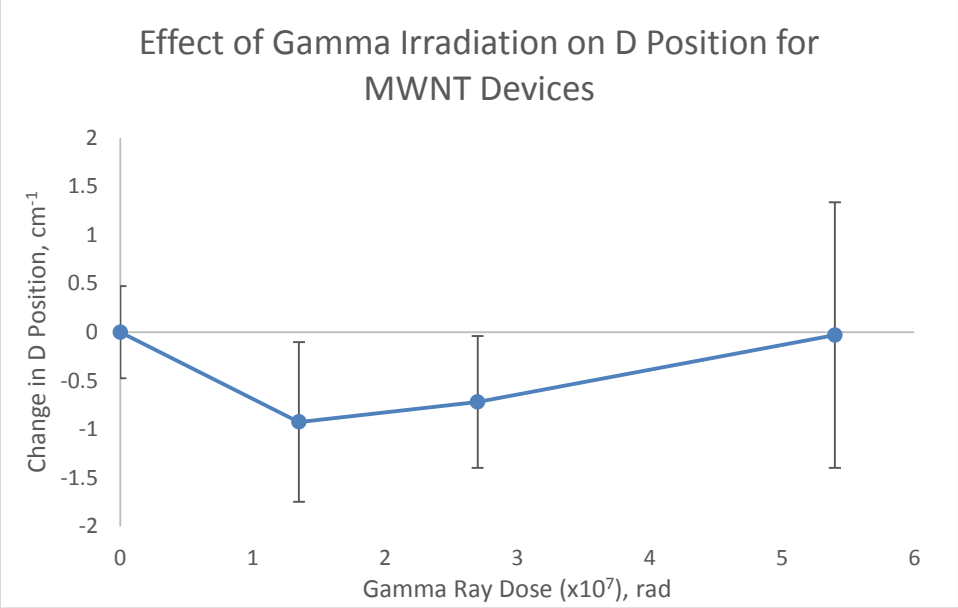

Figure 52: Effect of gamma irradiation on D peak position for MWNT devices. Vertical bars indicate standard deviation.

Raman spectroscopy of the SWNT networks after exposure to mixed gamma and neutron radiation in HFIR also fails to detect evidence of sample doping, as shown in Figure 53.

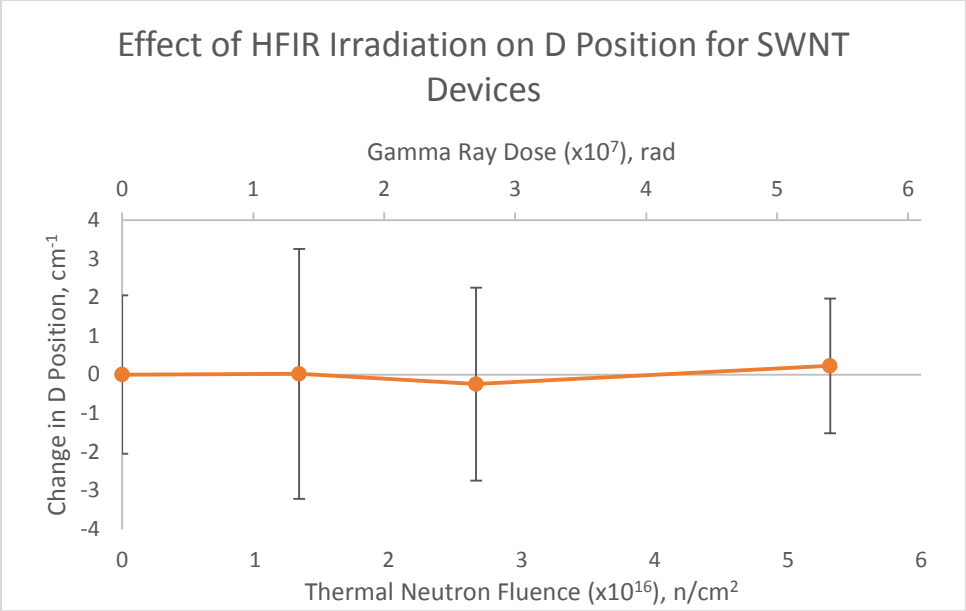

Figure 53: Effect of HFIR irradiation on D peak position for SWNT devices. Vertical bars indicate standard deviation.

Based on these results, it appears that the decrease in electrical resistance of the SWNT devices during HFIR irradiation was not due to doping. Another possibility is that both p- and n-type doping occurred to a similar extent, which would have the result of increasing the standard deviation of the Raman data while still showing no change in D peak position on average. The effects of pure gamma irradiation in GIF on the D peak position for the SWNT devices are shown in Figure 54.

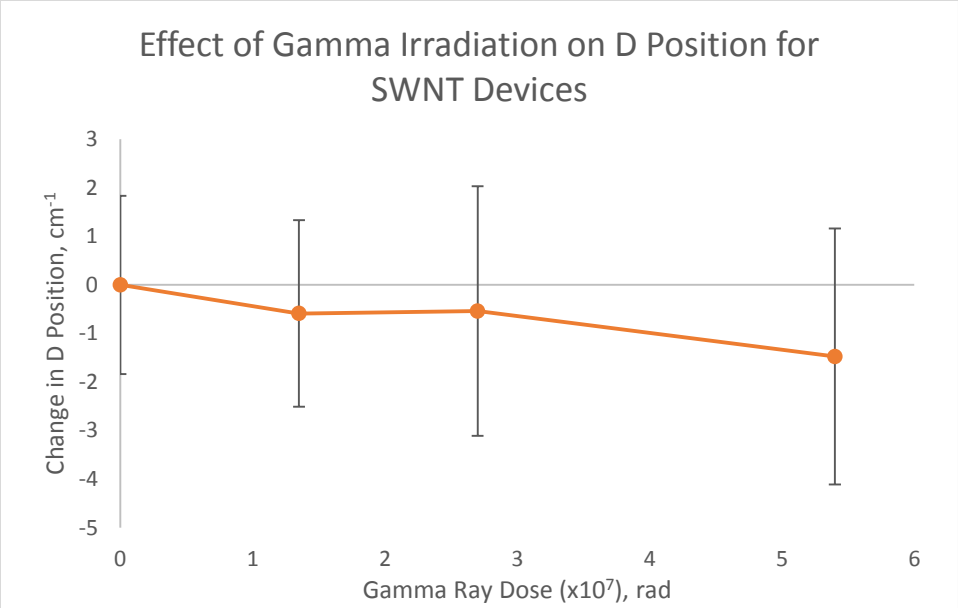

Figure 54: Effect of gamma irradiation on D peak position for SWNT devices. Vertical bars indicate standard deviation.

There appears to be a trend of slightly decreasing D peak position with increasing gamma ray dose in the SWNT devices, which would indicate n-type doping, but again the standard deviation of the data is quite high so it is not possible to be certain. Since SWNTs are often p-type semiconductors, n-type doping would contribute to an increase in resistance as is indeed seen in Figure 43. This possibility can be conclusively evaluated in the future by addition of a gate electrode to the device design in order to make a SWNT-based field effect transistor.

4.4 Humidity Analysis

The adsorption rate of water on randomly dispersed networks of SWNTs and MWNTs were measured at the same time that changes in their electrical properties were recorded. Figure 55 shows the mass of water adsorbed onto the surface of the samples along with the humidity profile. It can be seen that the MWNT samples adsorbed the most water at each humidity level.

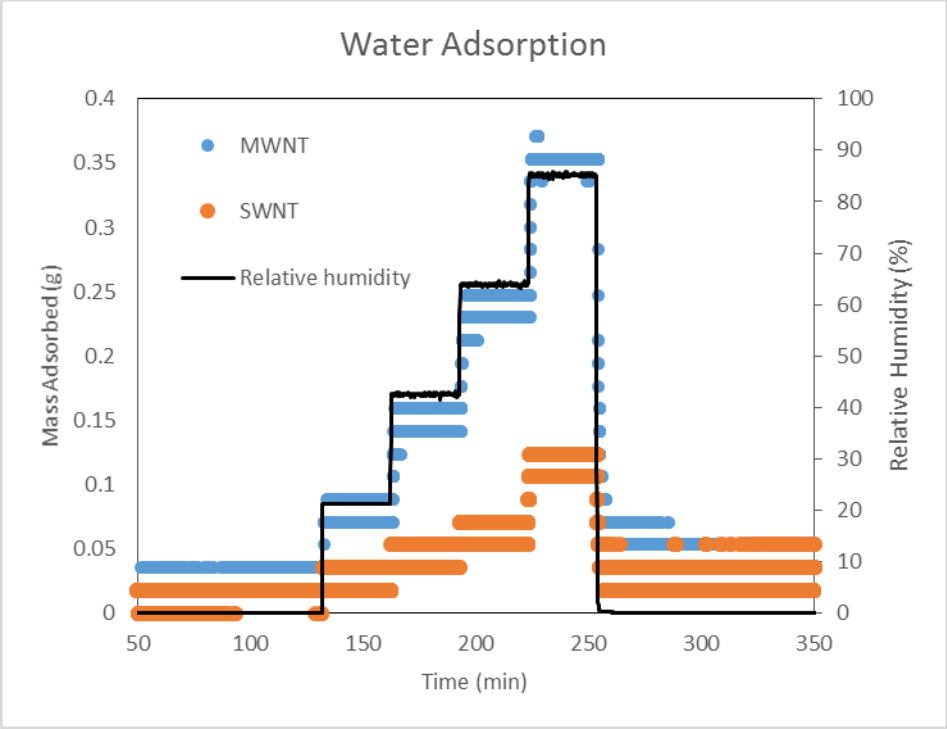

Figure 55: Water adsorption as a function of relative humidity

Figure 56 shows the changes in the DC resistance across electrodes of the three devices. The y-axis shows the ratio given by the resistance divided by the initial resistance. The initial resistance value was measured after degassing in vacuum overnight. The resistance of the MWNT device increases with increasing relative humidity but the SWNT device resistance decreases with increasing humidity.

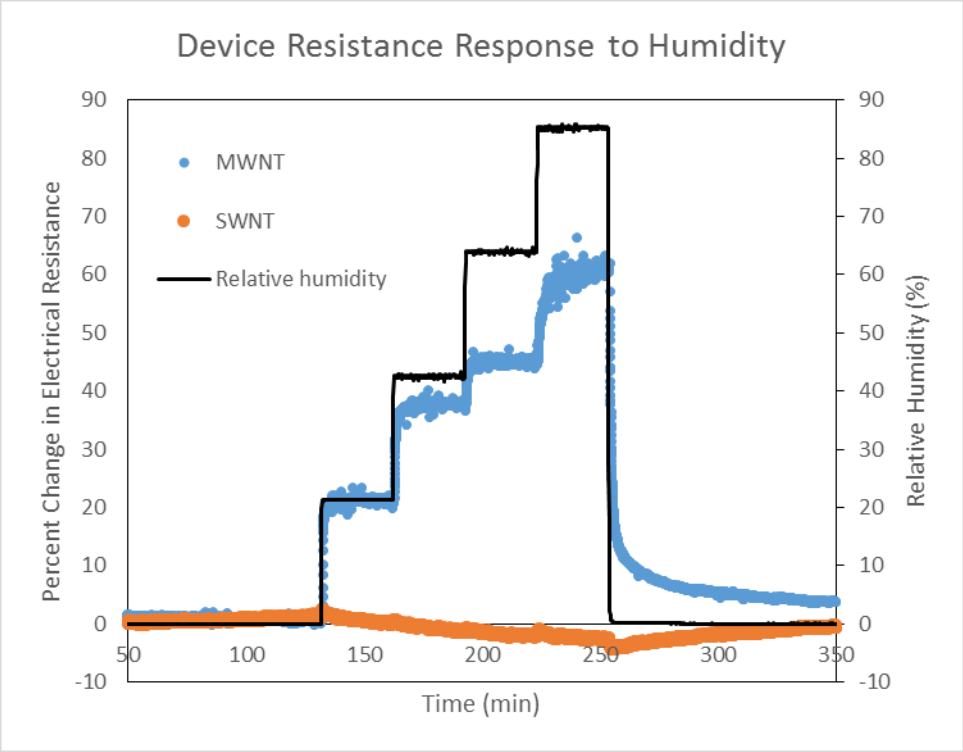

Figure 56: Effect of humidity on DC resistance.

The decreasing in resistance of the SWNTs can be explained by the fact that about 2/3 of the SWNT network is composed of semiconducting nanotubes. Adsorbed water molecules act as electron acceptors, or p-type dopants, leaving behind holes in the semiconducting SWNTs which decreases the resistance of the nanotube network. Because the MWNTs already behave as metallic conductors, doping by water molecules increases their resistivity.

4.5 Thermal Annealing

It is well known that CNTs possess the ability to self-heal structural defects by rearrangement of the local microstructure to saturate energetically unfavorable dangling bonds. Many defects are healed almost instantaneously, but others require the injection of some energy. It was hypothesized that this

type of annealing, where energy from neutron and gamma irradiation facilitated migration of defects, could contribute to a reduction in resistance of the CNT networks.

To test this hypothesis, non-irradiated devices were annealed in nitrogen for one hour at temperatures of 100, 200, 300, 400, and 500 °C. The electrical resistance was measured before and after baking. Figure 57 shows the effect of annealing on SWNT devices.

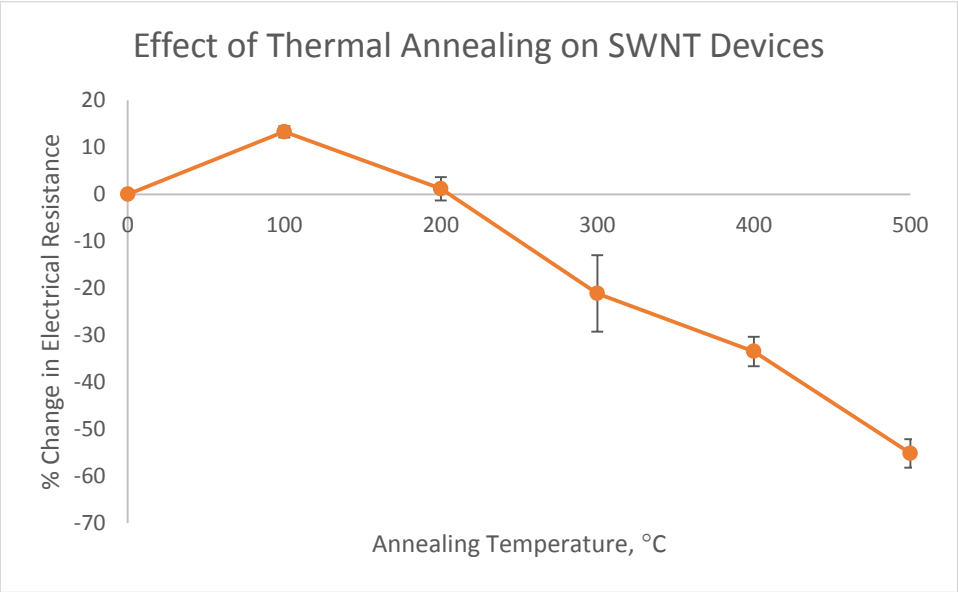

Figure 57: Effect of thermal annealing on SWNT devices. Vertical bars show standard deviation.

The SWNT devices show an initial increase in resistance followed by linear decrease. The initial increase in resistance at 100 °C is the result of desorption of dopants such as water and oxygen. As demonstrated by the humidity analysis, adsorbed dopants can reduce the resistance of these SWNT networks, so naturally desorption would result in an increase in resistance. After this initial increase, thermal annealing takes place, healing defects in the nanotube and decreasing the resistance. The reduction in resistance forms a linear trend from 100 °C to 500 °C, indicating that annealing is taking place at temperatures as low as 200 °C and that even after 400 °C there are still defects that can only be

annealed at higher temperature. Over this linear region, each 100 °C increase in bake temperature resulted in a 17.2% reduction in electrical resistance. Although it appears there may still be some annealing of defects possible with higher temperatures, carbon nanotubes begin to degrade at temperatures above 550 °C, which would overshadow any annealing effects.

Since the MWNT devices do not contain semiconducting CNTs, no increase in resistance is expected. Figure 58 shows the effects of thermal annealing on the MWNT devices.

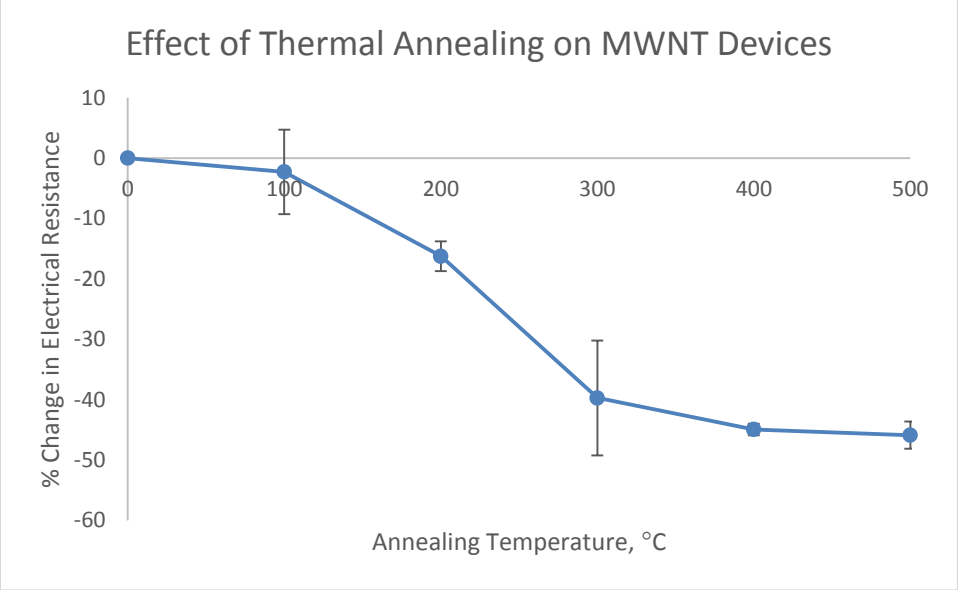

Figure 58: Effect of thermal annealing on MWNT devices. Vertical bars show standard deviation.

There is an initial slight decrease in resistance after baking at 100 °C due to desorption of dopants such as water and oxygen. This is followed by a region from 100 °C to 300 °C of steep reduction in resistance due to thermal annealing of defects. Over this region, the electrical resistance decreases by about 18.7% for every 100 °C increase in bake temperature, which is very close to the 17.2% rate seen in the SWNTs. However, for the MWNTs, this trend begins to level off after 300 °C indicating that increasing temperature no longer results in further annealing. From this, it can be reasonably deduced that the

MWNTs are fully annealed at a lower temperature than the SWNTs. The maximum reduction in resistance for the MWNTs after fully annealing is only 45.9% while the maximum reduction in resistance for the SWNT devices was over 55%, with no reason to suspect that further increases to temperature would not result in even more annealing.

These results indicate that thermal annealing begins at approximately the same temperature for both SWNTs and MWNTs, namely around 100 °C, and that increases in temperature for the next 200 °C increases the amount of defects that can be annealed at about the same rate. So annealing at temperatures below 300 °C is very similar for the two types of nanotubes, and it is only at higher temperatures that there are significant differences in annealing behavior. In the SWNTs, there are defects that can only be annealed by temperatures above 300 °C, still more that can only be annealed by exposure to temperatures above 400 °C, and likely more defects that are only annealed at higher temperatures. In the MWNTs, these types of defects either do not exist or cannot be annealed by exposure to higher temperatures.

This greater potential for thermal annealing of defects in SWNT devices could play a role in explaining the sharp contrast between the electrical behavior of the SWNT devices and the MWNT devices upon exposure to mixed gamma and neutron radiation in HFIR. Due to the extremely high flux in PT-1, nanotube defects can be subject to high local temperatures even during short irradiations.

If MWNTs contain defects that cannot be healed by thermal annealing but SWNTs do not, it would make sense that these defects would accumulate in MWNTs but not in SWNTs during irradiation in HFIR. The ambient temperature in PT-1 is less than 130 °C, but local temperatures often greatly exceed this. When energy is transferred to a nanotube in the form of heat, that heat is easily conducted through the defect

free portions of the nanotube but builds up rapidly when it encounters a barrier to heat transfer. These high energy points could cause annealing of the type demonstrated here, resulting in significant decreases in resistance. If the local heating is high enough, it would affect SWNTs more than MWNTs, since all MWNT annealing can be accomplished at low energy levels.

This thermal annealing can also explain some of the differences between behavior of the SWNTs in the high neutron/gamma flux environment of HFIR and the lower flux of pure gamma rays in GIF. The gamma flux of HFIR is an order of magnitude higher than that of GIF and additionally is accompanied by a massive neutron flux, so even though the gamma fluence in the two facilities was equal, the heating was much higher in HFIR than in GIF. This difference in temperature explains why the resistance did not drop in GIF like it did in HFIR. The temperature was not high enough to allow significant annealing of defects.

5. Conclusions and Future Work

5.1 Conclusions

5.1.1 MWNT Devices

The MWNT devices show great promise as real time neutron dosimeters for RPV lifetime assessment, and represent an improvement over the current state-of-the-art. The electrical resistance of the devices increases linearly with increasing radiation fluence over the relevant range of neutron fluences and the standard deviation from device to device is low. They are insensitive to gamma rays, which is good because the damage to the RPV is caused primarily by neutron bombardment. These changes in electrical properties are caused by damage to the microstructure of the MWNTs, meaning that the dose information is locked in and will not change over time. This is advantageous for nuclear forensics because, in the case of a nuclear accident, investigators may not be able to access the dosimeters until months after the fact.

These devices are intrinsically cheap and scalable, making them ideal for commercialization. The wafer processing fabrication technique allows for thousands of devices to be fabricated on a single wafer. This improves the reliability of the devices from a quality control perspective, guaranteeing high uniformity of device performance. The fact that these dosimeters are incredibly small and cheap opens up the possibility for real time dose mapping, where dosimeters are placed at a number of locations throughout the pressure vessel. This technique provides the increased accuracy needed to ensure safe operation of existing and future plants through their life extensions.

5.1.2 SWNT Devices

The behavior of the SWNT devices is more complex than that of the MWNT devices, with pure gamma irradiation having a very different effect than mixed gamma and neutron irradiation. Gamma irradiation substantially increases the resistance of the devices while combined neutron and gamma irradiation decreases the resistance. This complex behavior is not suitable for dosimetry, but it is of great interest to the nanoscience community.

It is clear that annealing plays a significant role in the decrease in electrical resistance of the SWNT devices during HFIR irradiation. It is also possible that the formation of crosslinks contributes to the decrease in resistance. Raman data does not support the hypothesis that the reduction in electrical resistance in HFIR is caused by doping of the SWNTs. The mechanism of this decrease in resistance is quite powerful, as it dominates the strong increase in resistance caused by pure gamma irradiation. Pure gamma irradiation increases the resistance of the SWNT devices by over 70% and yet when exposed to combined neutron and gamma radiation in HFIR, the overall result is a drop in resistance of around 20%. Such a reaction can be understood if the damage caused by gamma irradiation is being continuously annealed, but that raises the question of the effect of dose rate. Raman data suggests the possibility that the pure gamma irradiation does cause n-type doping of the SWNTs, which could contribute to the increase in electrical resistance.

5.2 Future Work

The results discussed here demonstrate that the MWNT dosimeters are effective at measuring neutron radiation fluence, but there are still some issues to be addressed and possible improvements that can be made. Additionally while this work provides substantial contributions to the understanding of the

effects of neutron and gamma irradiation on carbon nanotubes, it also raises a number of questions. There are a several very interesting routes that future research can build upon the results of this project.

Prior to commercialization, in order to demonstrate that the MWNT devices can truly function as real time dosimeters, it is necessary to perform instrumented irradiation of the devices. In this work only the changes in electrical resistance that persist after irradiation were measured. It is essential to demonstrate that there are no unexpected effects that are present during irradiation that could interfere with accurate dosimetry. It is also important to repeat these experiments at a number of different flux levels, to ensure that the results are independent of the dose rate.

The design could also potentially be improved by addition of a gate electrode to make it a field effect transistor (FET). Changes in threshold gate voltage can provide useful information on doping and potentially increase the sensitivity and reliability of the dosimeters. This modification to the device can be used to distinguish between changes to the resistance due to doping and those due to damage to the microstructure.

These SWNT devices were fabricated from a mix of semiconducting and metallic SWNTs and it is likely that these two types of nanotubes are affected differently by irradiation. The results presented here of the changes to the electrical resistance of a mixed network can be better understood if the effects of each type of nanotube are investigated separately. It is possible to segregate semiconducting and metallic SWNTs by the method of density-gradient ultracentrifugation [98], by using competing mixtures of structure-discriminating surfactants [99], and by selective functionalization [100]. By fabricating devices from only semiconducting SWNTs and from only metallic SWNTs, a greater understanding of the

effects of irradiation can be gained. It would also be very interesting to investigate the effects of nanotube network density.

The method used in this project to attempt to tune the sensitivity of the devices to neutron radiation via a boron conversion layer resulted in destruction of the samples, but the idea has merit and an alternative method could be pursued. The issues encountered during this project had to do with poor adhesion of the boron layer, which can easily be overcome by alternative approaches to incorporate boron into the device. Additionally, since the objective of the boron conversion layer is to increase the sensitivity of the devices, a lower flux neutron source should be used. Since the boron conversion layer works by emitting alpha particles upon exposure to neutron irradiation, an analysis of the effects of pure alpha irradiation on CNTs should also be explored.

It would also be very interesting to examine the effects of other nanomaterials, such as graphene. Graphene has a similar structure to carbon nanotubes but its electrical properties are quite different due to the fact that it is flat rather than cylindrical. It is, however, similarly sensitive to defects and it would be worthwhile to investigate the effects of neutron irradiation on its microstructure and electrical properties.

References

1. Ilieva, K., et al., *Reactor dosimetry for VVERs RPV lifetime assessment.* Progress in Nuclear Energy, 2009. **51**(1): p. 1-13.
2. Serén, T. and T. Kekki, *Retrospective dosimetry based on niobium extraction and counting-VTT's contribution to the RETROSPEC project.* VTT TIEDOTTEITA, 2003.
3. Ballesteros, A., et al., *Open issues in reactor dosimetry.* Progress in Nuclear Energy, 2010. **52**(7): p. 615-619.
4. Belousov, S., K. Ilieva, and M. Mitev, *Reactor dosimetry and RPV life management.* American Society for Testing and Materials-ASTM International, 2011.
5. Hopkins, D.N., E.T. Hayes, and A.H. Fero, *Ex-vessel neutron dosimetry results in the vicinity of RPV supports*. Proceedings of the ASME Pressure Vessels and Piping Conference, ed. A.C. Smith. Vol. 7. 2007, New York: Amer Society Mechanical Engineers. 125-134.
6. Knoll, G.F., *Radiation detection and measurement*. 2010: John Wiley & Sons.
7. Rinard, P., *Neutron interactions with matter.* Passive Nondestructive Assay of Nuclear Materials, 1991: p. 357-377.
8. Iijima, S., *Helical microtubules of graphitic carbon.* Nature, 1991. **354**: p. 56-58.
9. Wang, X., et al., *Fabrication of ultralong and electrically uniform single-walled carbon nanotubes on clean substrates.* Nano Letters, 2009. **9**(9): p. 3137-3141.
10. Thostenson, E.T., Z. Ren, and T.-W. Chou, *Advances in the science and technology of carbon nanotubes and their composites: a review.* Composites Science and Technology, 2001. **61**(13): p. 1899-1912.
11. Treacy, M.M.J., T.W. Ebbesen, and J.M. Gibson, *Exceptionally high Young's modulus observed for individual carbon nanotubes.* Nature, 1996. **381**(6584): p. 678-680.

12. Poncharal, P., et al., *Electrostatic deflections and electromechanical resonances of carbon nanotubes.* Science, 1999. **283**(5407): p. 1513-1516.

13. Krishnan, A., et al., *Young's modulus of single-walled nanotubes.* Physical Review B, 1998. **58**(20): p. 14013-14019.

14. Wong, E.W., P.E. Sheehan, and C.M. Lieber, *Nanobeam mechanics: elasticity, strength, and toughness of nanorods and nanotubes.* Science, 1997. **277**(5334): p. 1971-1975.

15. Salvetat, J.-P., et al., *Elastic and shear moduli of single-walled carbon nanotube ropes.* Physical Review Letters, 1999. **82**(5): p. 944-947.

16. Yu, M.-F., et al., *Strength and breaking mechanism of multiwalled carbon nanotubes under tensile load.* Science, 2000. **287**(5453): p. 637-640.

17. Dresselhaus, M.S., et al., *Carbon Nanotubes*, in *The Physics of Fullerene-Based and Fullerene-Related Materials*, W. Andreoni, Editor. 2000, Springer Netherlands: Dordrecht, The Netherlands. p. 331-379.

18. Falvo, M., et al., *Bending and buckling of carbon nanotubes under large strain.* Nature, 1997. **389**(6651): p. 582-584.

19. Wagner, H., et al., *Stress-induced fragmentation of multiwall carbon nanotubes in a polymer matrix.* Applied Physics Letters, 1998. **72**(2): p. 188-190.

20. Walters, D., et al., *Elastic strain of freely suspended single-wall carbon nanotube ropes.* Applied Physics Letters, 1999. **74**(25): p. 3803-3805.

21. Demczyk, B., et al., *Direct mechanical measurement of the tensile strength and elastic modulus of multiwalled carbon nanotubes.* Materials Science and Engineering: A, 2002. **334**(1): p. 173-178.

22. Muster, J., et al., *Scanning force microscopy characterization of individual carbon nanotubes on electrode arrays.* Journal of Vacuum Science & Technology B: Microelectronics and Nanometer Structures, 1998. **16**(5): p. 2796-2801.

23. Baughman, R.H., A.A. Zakhidov, and W.A. de Heer, *Carbon nanotubes--the route toward applications.* Science, 2002. **297**(5582): p. 787-792.

24. Soh, H.T., et al., *Integrated nanotube circuits: controlled growth and ohmic contacting of single-walled carbon nanotubes.* Applied Physics Letters, 1999. **75**(5): p. 627-629.

25. Collins, P.G. and P. Avouris, *Nanotubes for electronics.* Scientific American, 2000. **283**(6): p. 62-69.

26. Postma, H.W.C., et al., *Electrical transport through carbon nanotube junctions created by mechanical manipulation.* Physical review B, 2000. **62**(16).

27. Rochefort, A., et al., *Electrical and mechanical properties of distorted carbon nanotubes.* Physical Review B, 1999. **60**(19).

28. Minot, E., et al., *Tuning carbon nanotube band gaps with strain.* Physical review letters, 2003. **90**(15).

29. Delaney, P., et al., *Broken symmetry and pseudogaps in ropes of carbon nanotubes.* Nature, 1998. **391**(6666): p. 466-468.

30. Zeng, H., et al., *Atomic vacancy defects in the electronic properties of semi-metallic carbon nanotubes.* Journal of Applied Physics, 2011. **109**(8).

31. Choi, H.J., et al., *Defects, quasibound states, and quantum conductance in metallic carbon nanotubes.* Physical Review Letters, 2000. **84**(13).

32. McEuen, P.L., et al., *Disorder, pseudospins, and backscattering in carbon nanotubes.* Physical Review Letters, 1999. **83**(24): p. 5098-5101.

33. Hansson, A. and S. Stafström, *Intershell conductance in multiwall carbon nanotubes.* Physical Review B, 2003. **67**(7).

34. Li, H.J., et al., *Multichannel ballistic transport in multiwall carbon nanotubes.* Physical review letters, 2005. **95**(8).

35. Terrones, M., et al., *Molecular junctions by joining single-walled carbon nanotubes.* Physical review letters, 2002. **89**(7): p. 075505.

36. Terrones, M., et al., *Coalescence of single-walled carbon nanotubes.* Science, 2000. **288**(5469): p. 1226-1229.

37. Susi, T., et al., *Atomistic description of electron beam damage in nitrogen-doped graphene and single-walled carbon nanotubes.* ACS nano, 2012. **6**(10): p. 8837-8846.

38. Krasheninnikov, A. and K. Nordlund, *Irradiation effects in carbon nanotubes.* Nuclear Instruments and Methods in Physics Research Section B: Beam Interactions with Materials and Atoms, 2004. **216**: p. 355-366.

39. Beuneu, F., et al., *Modification of multiwall carbon nanotubes by electron irradiation: an ESR study.* Physical Review B, 1999. **59**(8): p. 5945-5949.

40. Kis, A., et al., *Reinforcement of single-walled carbon nanotube bundles by intertube bridging.* Nature Materials, 2004. **3**(3): p. 153-157.

41. Ishaq, A., L. Yan, and D. Zhu, *The electrical conductivity of carbon nanotube sheets by ion beam irradiation.* Nuclear Instruments and Methods in Physics Research Section B: Beam Interactions with Materials and Atoms, 2009. **267**(10): p. 1779-1782.

42. Yan, L., et al., *Improving the electrical conductivity of multi-walled carbon nanotube networks by H ion beam irradiation.* Carbon, 2011. **49**(6): p. 2141-2144.

43. Krasheninnikov, A., K. Nordlund, and J. Keinonen, *Production of defects in supported carbon nanotubes under ion irradiation.* Physical Review B, 2002. **65**(165423): p. 1-8.

44. Krasheninnikov, A. and K. Nordlund, *Ion and electron irradiation-induced effects in nanostructured materials.* Journal of applied physics, 2010. **107**(7).

45. Krasheninnikov, A., et al., *Stability of carbon nanotubes under electron irradiation: role of tube diameter and chirality.* Physical review B, 2005. **72**(12).

46. Banhart, F., J. Li, and A. Krasheninnikov, *Carbon nanotubes under electron irradiation: stability of the tubes and their action as pipes for atom transport.* Physical Review B, 2005. **71**(24).

47. Krasheninnikov, A.V. and F. Banhart, *Engineering of nanostructured carbon materials with electron or ion beams.* Nature Materials, 2007. **6**(10): p. 723-733.

48. Stone, A. and D. Wales, *Theoretical studies of icosahedral C 60 and some related species.* Chemical Physics Letters, 1986. **128**(5): p. 501-503.

49. Xu, Z., et al., *Nano-structure and property transformations of carbon systems under γ-ray irradiation: a review.* Rsc Advances, 2013. **3**(27): p. 10579-10597.

50. Hulman, M., et al., *Raman spectroscopy of single-wall carbon nanotubes and graphite irradiated by γ rays.* Journal of applied physics, 2005. **98**(2): p. 024311.

51. Guo, J., et al., *The effects of γ-irradiation dose on chemical modification of multi-walled carbon nanotubes.* Nanotechnology, 2005. **16**(10): p. 2385.

52. Xu, Z., et al., *Modification of surface functionality and interlayer spacing of multi-walled carbon nanotubes using gamma-rays.* Journal of Applied Physics, 2011. **109**(5).

53. Gupta, S., R.J. Patel, and N.D. Smith. *Advanced carbon-based material as space radiation shields*. in *MRS Proceedings*. 2004. Cambridge Univ Press.

54. Skákalová, V., U. Dettlaff-Weglikowska, and S. Roth, *Gamma-irradiated and functionalized single wall nanotubes.* Diamond and Related Materials, 2004. **13**(2): p. 296-298.

55. Miao, M.H., et al., *Effect of gamma-irradiation on the mechanical properties of carbon nanotube yarns.* Carbon, 2011. **49**(14): p. 4940-4947.

56. Dahl, E.M., *Single-walled carbon nanotube response to neutron and gamma irradiation*. 2013, Thesis, Virginia Tech: Blacksburg, VA.

57. Cao, W.B., et al., *Neutron-irradiation catalyzed synthesis of novel carbon nanomaterials.* Journal of Radioanalytical and Nuclear Chemistry, 2007. **272**(3): p. 611-614.

58. Taylor, R., B.T. Kelly, and K.E. Gilchrist, *The thermal conductivity of fast neutron irradiated graphite.* Journal of Physics and Chemistry of Solids, 1969. **30**(9): p. 2251-2267.

59. Wu, C.H., et al., *Neutron irradiation effects on the properties of carbon materials.* Journal of Nuclear Materials, 1994. **212**: p. 416-420.

60. Budd, M.I., *Estimated influence of neutron damage on the divertor protection material during the physics phase of net.* Journal of Nuclear Materials, 1990. **170**(2): p. 129-133.

61. Burchell, T.D. and J.P. Strizak, *The effect of neutron irradiation on the fracture toughness of graphite.* Nuclear Engineering and Design, 2014. **271**: p. 262-269.

62. Oku, T., et al., *Effect of neutron irradiation on the microstructures and tensile properties of different carbon fibers.* Science Reports of the Research Institutes Tohoku University Series a-Physics Chemistry and Metallurgy, 1997. **45**(1): p. 63-65.

63. Tans, S.J., A.R. Verschueren, and C. Dekker, *Room-temperature transistor based on a single carbon nanotube.* Nature, 1998. **393**(6680): p. 49-52.

64. Cattanach, K., et al., *Flexible carbon nanotube sensors for nerve agent simulants.* Nanotechnology, 2006. **17**(16): p. 4123.

65. Parikh, K., et al., *Flexible vapour sensors using single walled carbon nanotubes.* Sensors and Actuators B: Chemical, 2006. **113**(1): p. 55-63.

66. Slobodian, P., et al., *Multi-wall carbon nanotube networks as potential resistive gas sensors for organic vapor detection.* Carbon, 2011. **49**(7): p. 2499-2507.

67. Occhiuzzi, C., et al., *RFID passive gas sensor integrating carbon nanotubes.* Microwave Theory and Techniques, IEEE Transactions on, 2011. **59**(10): p. 2674-2684.

68. Suehiro, J., et al., *Controlled fabrication of carbon nanotube NO2 gas sensor using dielectrophoretic impedance measurement.* Sensors and Actuators B-Chemical, 2005. **108**(1-2): p. 398-403.

69. Jacobs, C.B., M.J. Peairs, and B.J. Venton, *Review: Carbon nanotube based electrochemical sensors for biomolecules.* Analytica Chimica Acta, 2010. **662**(2): p. 105-127.

70. Martínez, M.T., et al., *Label-free DNA biosensors based on functionalized carbon nanotube field effect transistors.* Nano letters, 2009. **9**(2): p. 530-536.

71. Hecht, D.S., et al., *Bioinspired detection of light using a porphyrin-sensitized single-wall nanotube field effect transistor.* Nano Letters, 2006. **6**(9): p. 2031-2036.

72. Tang, X.W., et al., *Measurement of ionizing radiation using carbon nanotube field effect transistor.* Physics in Medicine and Biology, 2005. **50**(3): p. N23-N31.

73. Malekie, S. and F. Ziaie, *Study on a novel dosimeter based on polyethylene-carbon nanotube composite.* Nuclear Instruments & Methods in Physics Research Section a-Accelerators Spectrometers Detectors and Associated Equipment, 2015. **791**: p. 1-5.

74. Kang, Q.S., J.T.W. Yeow, and R. Barnett, *The use of semiconducting single-walled carbon nanotube films to measure X-ray dose.* Carbon, 2012. **50**(6): p. 2197-2201.

75. Lobez, J.M. and T.M. Swager, *Radiation detection: resistivity responses in functional poly (olefin sulfone)/carbon nanotube composites.* Angewandte Chemie, 2010. **122**(1): p. 99-102.

76. Boul, P.J., et al., *Single wall carbon nanotube response to proton radiation.* Journal of Physical Chemistry C, 2009. **113**(32): p. 14467-14473.

77. Robinson, J.A., et al., *Investigation of graphene-based nanoscale radiation sensitive materials.* Micro- and Nanotechnology Sensors, Systems, and Applications Iv, 2012. **8373**.

78. Foxe, M., et al. *Graphene-based neutron detectors*. in *Nuclear Science Symposium and Medical Imaging Conference (NSS/MIC), 2011 IEEE*. 2011. IEEE.

79. Foxe, M., et al., *Detection of ionizing radiation using graphene field effect transistors.* IEEE Transactions on Nanotechnology, 2012.

80. Patil, A., et al. *Graphene field effect transistor as radiation sensor*. in *Nuclear Science Symposium and Medical Imaging Conference (NSS/MIC)*. 2011. IEEE.

81. Harutyunyan, A.R., et al., *Purification of single-wall carbon nanotubes by selective microwave heating of catalyst particles.* Journal of Physical Chemistry B, 2002. **106**(34): p. 8671-8675.

82. Chiang, I., et al., *Purification and characterization of single-wall carbon nanotubes.* The Journal of Physical Chemistry B, 2001. **105**(6): p. 1157-1161.

83. *In-Vessel Irradiation Experiment Facilities at HFIR*. [cited 2016; Available from: https://neutrons.ornl.gov/hfir/in-vessel-irradiation].

84. Smith, E. and G. Dent, *Modern Raman spectroscopy: a practical approach*. 2013: John Wiley & Sons.

85. Dresselhaus, M.S., et al., *Raman spectroscopy of carbon nanotubes.* Physics Reports, 2005. **409**(2): p. 47-99.

86. Jorio, A., et al., *Raman Spectroscopy in Graphene Related Systems*. 2011, Weinheim, Germany: Wiley-VCH.

87. Cao, C.L., et al., *Humidity sensor based on multi-walled carbon nanotube thin films.* Journal of Nanomaterials, 2011: p. 5.

88. Benchirouf, A., et al., *Humidity sensitivity of thin films based dispersed multi-walled carbon nanotubes*. 10th International Multi-Conference on Systems, Signals & Devices. 2013, New York: IEEE.

89. Kong, J., et al., *Nanotube molecular wires as chemical sensors.* Science, 2000. **287**(5453): p. 622-625.

90. Duan, Y., et al., *A comparative analysis of thin-film transistors using aligned and random-network carbon nanotubes.* Journal of Nanoparticle Research, 2013. **15**(3): p. 7.

91. Martel, R., et al., *Single-and multi-wall carbon nanotube field-effect transistors.* Applied Physics Letters, 1998. **73**(17): p. 2447-2449.

92. Zahab, A., et al., *Water-vapor effect on the electrical conductivity of a single-walled carbon nanotube mat.* Physical Review B, 2000. **62**(15): p. 10000-10003.

93. Skákalová, V., et al., *Ion irradiation effects on conduction in single-wall carbon nanotube networks.* Applied Physics A, 2008. **90**(4): p. 597-602.

94. Salonen, E., A. Krasheninnikov, and K. Nordlund, *Ion-irradiation-induced defects in bundles of carbon nanotubes.* Nuclear Instruments and Methods in Physics Research Section B: Beam Interactions with Materials and Atoms, 2002. **193**(1): p. 603-608.

95. O'Brien, N., M. McCarthy, and W. Curtin, *Improved inter-tube coupling in CNT bundles through carbon ion irradiation.* Carbon, 2013. **51**: p. 173-184.

96. Federizzi, R.L., C.S. Moura, and L. Amaral, *Polymerization of carbon nanotubes through self-irradiation.* The Journal of Physical Chemistry B, 2006. **110**(46): p. 23215-23220.

97. Skákalová, V., et al., *Effect of gamma-irradiation on single-wall carbon nanotube paper*, in *Molecular Nanostructures*, H. Kuzmany, et al., Editors. 2003. p. 143-147.

98. Ghosh, S., S.M. Bachilo, and R.B. Weisman, *Advanced sorting of single-walled carbon nanotubes by nonlinear density-gradient ultracentrifugation.* Nature nanotechnology, 2010. **5**(6): p. 443-450.

99. Arnold, M.S., et al., *Sorting carbon nanotubes by electronic structure using density differentiation.* Nature nanotechnology, 2006. **1**(1): p. 60-65.

100. Kim, W.-J., M.L. Usrey, and M.S. Strano, *Selective functionalization and free solution electrophoresis of single-walled carbon nanotubes: Separate enrichment of metallic and semiconducting SWNT.* Chemistry of Materials, 2007. **19**(7): p. 1571-1576.